ASTROCHEMICAL MODELING OF STAR-FORMING REGIONS

Brielle M. Shope
Greenwood, Indiana

B.A. Chemistry, Taylor University, 2018
M.S. Physics, Ball State University, 2020

A Dissertation Presented to the
Graduate Faculty of the
University of Virginia
in Candidacy for the Degree of
Doctor of Philosophy

Department of Chemistry

University of Virginia
May 2025

Committee Members:
Robin T. Garrod
L. Ilsedore Cleeves
Remy Indebetouw
Zhi-Yun Li

ABSTRACT

Astrochemistry influences various stages of a star's life cycle, including the star-forming phase, where molecular clouds collapse to form protostars and protostellar disks. This thesis explores the formation and evolution of complex organic molecules (COMs) in both high-mass and low-mass star-forming cores through astrochemical modeling. I investigate extreme methyl formate (MF) to glycolaldehyde (GA) ratios in NGC 6334I, identifying high gas densities and prolonged desorption timescales as the physical cause. To trace ice chemistry evolution from pre-stellar collapse to protostellar disk formation, I present a coupled radiation hydrodynamical and chemical model of a hot corino, comparing column density predictions with JWST and Spitzer observations across different YSO stages. Furthermore, I analyze COM variability in four Class 0 protostars from the CORINOS project, utilizing ALMA observations and radiative transfer modeling. I find that the low-inclination source, Ser-emb 7, exhibits lower observed CH_3OH column densities, while ice column densities remain unaffected during Class 0. By integrating astrochemical modeling with observational comparisons, this work addresses key scientific inquiries: the physical conditions and chemical pathways that drive high MF:GA ratios, the impact of viewing angle on observed column densities, and the implications of our models on the inheritance of COMs in solar-type star formation. These findings advance understanding of COM evolution, providing insights into protostellar chemistry and molecular origins.

Acknowledgements

Like a comet pulled from orbit as it passes a sun, like a stream that meets a boulder halfway through the wood. Who can say if I've been changed for the better? But because I knew you, I have been changed for good."

Wicked, *For Good*

During my studies at the University of Virginia, I lived in a small town west of Charlottesville called Crozet. On my short commute to school, I'd often fill my car with music that became my anthems. Day in and day out I listened to these songs. On my way to a normal day in the office. My exams. The nauseating days of my early pregnancy. In the following pages at the start of each chapter, you will find some selected lyrics of the music that was an integral part of my road to obtaining a PhD.

The town of Crozet, nestled at the base of the Blue Ridge Mountains, will forever and always hold a piece of my heart. It is where I started my life as a newly wed, became a momma, and met the most precious, heartwarming community that I love dearly. To my Crozet community, thank you for the memories, the home-cooked meals, and friendship.

Another influential part of my life there was my church - First Baptist Park Street in Charlottesville. Pastor Rob, the Fields, the Fitzgeralds, the church choir, and my

Sunday School class - from the warm reception on my first Easter Sunday, to the weekly choir rehearsals, and welcoming smiles each week, you all have made my time here one to cherish and it's harder than ever to leave. And the most special thanks to Dana Fitzgerald, who helped watch Isaiah for a while once my maternity leave ended.

My family. Austan, thank you for taking the leap, the act of love, to leave everything familiar and start our adventure as a married couple in the hills of Virginia. This has been a beautiful chapter of our life. Breathtaking views from the tops of mountains. Hot summer trips to Sugar Hollow. The many, many trips to King Family Vineyards. Our walks to the park as a family. The adventures around the wooded loop in our neighborhood that practically became our backyard. I loved seeing you fall in love with the mountains and finding reward and purpose in your training with Blue and Grey K-9 Search and Rescue.

My son Isaiah, I love you so very much. I love being your momma and it will give me so much joy and pride to have you on my hip when I graduate. Being pregnant and a new mother in graduate school was not without its challenges - of course physically (the nausea, the back pain, the lack of sleep postpartum - this list could go on...) but also emotionally. I faced questions from others about my situation: why I was pregnant in graduate school, whether I was truly dedicated to my studies, and how I was going to spend my time during maternity leave, because apparently I had to do "something" with my time. But I set a boundary for our precious time, choosing to be present with you and embrace the countless hours of rocking, coddling, and nurturing you. I was nearly denied a scholarship nomination simply because I was pregnant, as the committee questioned my commitment to finishing my PhD. But who cares if I wasn't "forthright" enough for some? We did it.

Mom and dad - thank you both for your investment in me and your support towards my studies over the MANY years. We are finally here. Mom, thank you for all your sacrifices. You have taught me to keep my faith strong and taught me invaluable lessons on how to present myself to each day and challenge. Dad, it is evident that your spirit and drive in life has shaped who I am today. Thank you for instilling the love of learning and desire for growth in me. You have been here as my career paradigm shifts and you are here to propel me into whatever next endeavor is on my mind.

To my advisor, Rob, thank you for the countless hours you've spent teaching me the field of astrochemistry and advising me in my research. Having an advisor with whom I can freely share my ideas — scientific and even political — has truly been a gift. An American patriot in spirit, but still unmistakably English. My time as your research student has inadvertently enriched my vocabulary, and I now find it to be a rather more 'proper' way of things, with 'quite' having firmly made its way into my everyday speech. 'Cheers' to that!

To the rest of my thesis committee, thank you for your guidance along the various milestones of my PhD and throughout my academic career.

My peers in astrochemistry - Rachel Gross, Abygail Waggoner, Mélisse Bonfand, Sydney Willis, Grace Dinges, Drew Christianson, Kamil Stelmach, and so many more - it has been a pleasure working alongside you. I am thankful for the friendships I have made along the way and look forward to keeping in touch and seeing the directions each one of us take.

And ultimately, I acknowledge my Lord and Savior. "The grass withers, the flower fades, but the word of our God stands forever" (Isaiah 40:8). I find it a great honor to study how you have set this world into motion and with each discovery, I get to know you more.

To lifelong learning.

TABLE OF CONTENTS

List of Figures

List of Tables

CHAPTER 1

INTRODUCTION

"Why do you write like you're running out of time? Write day and night like you're running out of time. Every day you fight like you're running out of time. Keep on fighting, in the meantime. Non-stop!"

Hamilton, *Non-Stop*

1.1 IN THE VASTNESS OF SPACE

When looking up at the night sky, onlookers could easily assume that there is a vast, empty, nothingness between the stars. However, the space between the stars brims with activity. This vast space between the stars is called the Interstellar Medium (ISM) and within are stellar nurseries, the birthing places of young stars and planets.

These stellar nurseries host rich and dynamic chemistry, occurring both in the gas phase and on the surfaces of small sub-micrometer-sized dust grains. These grains are paramount to the eventual formation of more complex molecules that are later transformed into species of biological importance, such as amino acids and sugars. These complex species are suspected to eventually make their way into comets, asteroids, and the fabric of planets like our own. The field that studies the chemical behavior of atoms and molecules in astrophysical environments is called astrochemistry. It is interdisciplinary in nature, combining knowledge from chemistry, astronomy, and physics. By studying the chemistry that occurs in the vastness of space, we can get a better picture of how stars and their surrounding material evolve into established systems like our own.

1.2 ASTROPHYSICAL ENVIRONMENTS

In introductory astronomy, star formation is often taught with a focus on stellar nucleosynthesis - the fusion of hydrogen and helium into heavier elements. What is less commonly explored and taught is the intricate chemistry that occurs in the surrounding environment and how that chemistry changes over time. Astrochemistry occurs in various astronomical environments, all of which contain their own unique chemistry influenced by their respective environment. I will start with a description of the interstellar medium.

The interstellar medium refers to the vast space between stars in galaxies. Gas is the primary component of the interstellar medium, with hydrogen being the most abundant element. Other elements, such as helium, carbon, oxygen, and nitrogen, are also present, but in smaller quantities. Dust grains, composed of tiny solid particles, are another significant component of the ISM. These particles are mainly made up of carbon, silicates, and ice and provides sites for the condensation of heavy elements.

The interstellar medium is not uniform but exhibits a range of densities and temperatures. From least dense to most dense, this includes the hot ionized medium, diffuse interstellar clouds, dark molecular clouds, and giant molecular clouds. The material between clouds is the hot ionized medium, which contains sparse ionized gas and can achieve temperatures over 10,000 K. Diffuse gas refers to the tenuous gas found throughout the ISM. Diffuse clouds are the most sparse of the clouds, with hydrogen densities of $n_{\mathrm{gas}} = 10 - 1000$ cm^{-3} and temperatures of $T_{\mathrm{gas}} = 50 - 100$ K. The visual extinction, a measure of the drop in brightness due to an intervening medium (dust), is usually low, with values of $A_{\mathrm{v}} \simeq 1$. Molecules in diffuse clouds are typically detected through absorption of background starlight. Dark clouds have densities of $n_{\mathrm{gas}} = 10^3 - 10^5 cm^{-3}$ and temperatures of $T_{\mathrm{gas}} \simeq 10$ K. These clouds are opaque, with a visual extinction of $A_{\mathrm{v}} > 10$ mag.

Molecular clouds are dense regions with densities that can reach 10^6 cm^{-3} or more. Within molecular clouds can form two types of star-forming objects, either high-mass or low-mass molecular cores. High-mass cores are commonly called “hot cores”, and often form in clusters. They are chemically rich, have high rotational temperatures ($>$ 100 K), and reach high densities ($>$ 10^7 cm^{-3}). Low-mass cores can form in isolation and include solar-type stars. Low-mass cores also often form in a cluster around a high-mass core (Williams et al., 2023). Low-mass star-formation is associated with a Young Stellar Object (YSO) classification scheme that includes

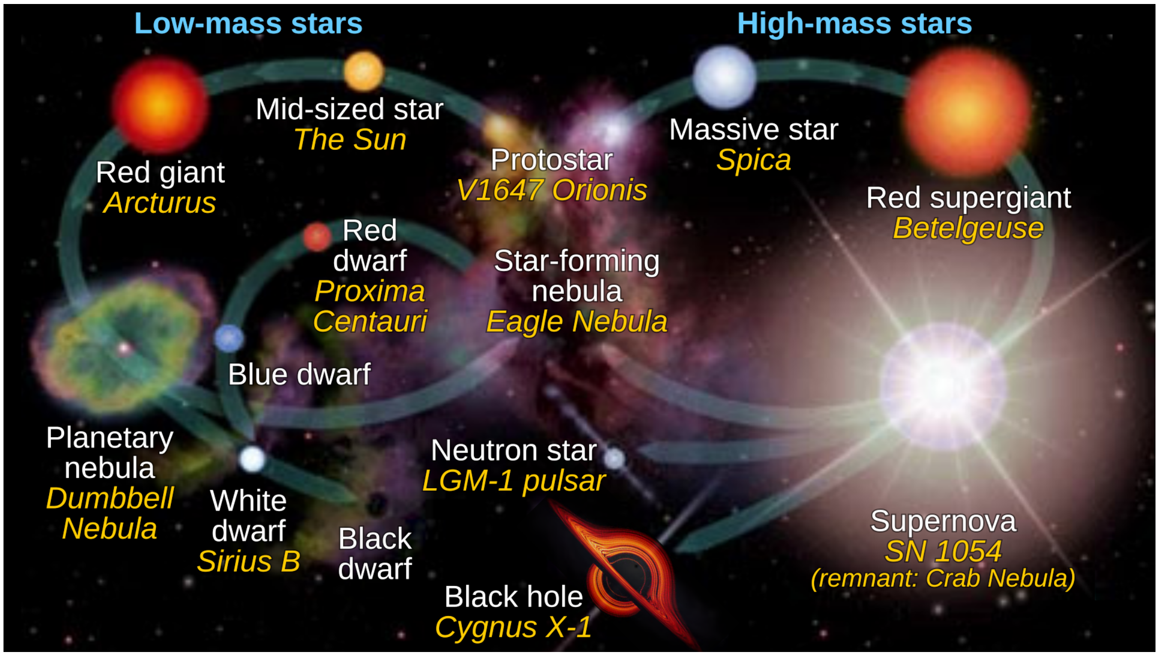

Figure 1.1 Star life cycle for both low- and high-mass stars. Credit: “Star life cycles red dwarf en" by cmglee, NASA Goddard Space Flight Center

the formation of a pre-stellar core, protostar, protoplanetary disk, and eventually a planetary system. Hot cores have dynamical processes that are not agreed upon, so they do not fall into the YSO classifications.

For both low-mass and high-mass stars, the star reaches the end of its lifetime once the star runs out of hydrogen. During a star’s lifetime, the heat produced by the conversion of hydrogen to helium through nuclear fusion provides the outward pressure to counteract gravity. Once the hydrogen is gone, collapse of the star follows as the force of gravity finally takes over. During collapse of the star, the star will first expand due to the increase of temperature and pressure as the outer material first started to fall inward. For a low-mass star, the star will enter a red-giant phase and the high-mass star a red supergiant phase. For low-mass stars, as the outer material expands, the inner core will contract inward into what is called a white dwarf and leave behind a planetary nebula. This material from the planetary nebula expands over time and space and eventually results in a molecular cloud and the star-formation cycle repeats. For high-mass stars ($\geq 8M_{\odot}$), the end result is different. Due to the amount of mass, the collapse leads to supernova explosion, with material spewing into the ISM, aiding in the development of distant star-forming regions. The remaining core results in a neutron star or black hole. Figure 1.1 illustrates the star life cycle for low-mass and high-mass stars.

1.2.1 Young Stellar Objects

Low-mass star-formation has five classes according to the Young Stellar Object classification scheme. Although the classification is based on the infrared spectral energy distribution and each class is defined by a spectral index, the following description gives an overview of the features of each class.

Class -I is a pre-stellar core, and forms through contraction of self-gravitating dust and gas. These regions show strong molecular depletion, as gas-phase molecules freeze out onto dust grains, but no signs of star-formation. They typically survive for around 1 million years before collapsing. Class 0 starts when material starts to accrete from the envelope onto the protostar. This class lasts as long as the mass of the envelope is larger than the mass of the protostar. Once the mass of the protostar overtakes the mass of the envelope, the protostar enters the Class I stage, in which it becomes a deeply embedded source and a protostellar disk starts to form. At this stage, there is fluctuation in ice composition within the disk. Particles that have close approaches to the hot protostar will experience more grain species desorption than particles that accrete onto the cold outer disk or evade the high temperatures near the protostar. These YSO stages are illustrated in Figure 1.2.

After protostellar disk formation, the Class II stage entails hydrostatic equilibrium of the core, the start of hydrogen fusion of the star, and the surrounding material

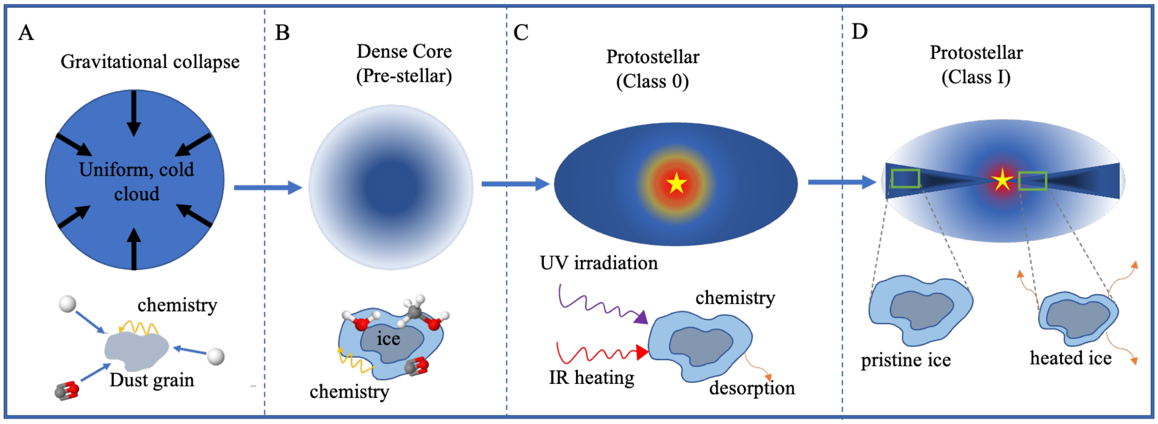

Figure 1.2 Young Stellar Object (YSO) stages and corresponding grain-ice chemistry. From the left, a uniform cloud collapses into a dense pre-stellar core. During this stage, hydrogen and other atoms and simple molecules accrete onto the dust-grain surface and form an icy mantle. As the protostar accretes material from the surrounding envelope (Class 0), UV-induced chemistry occurs on grain surfaces and molecules start to desorb due to thermal heating. In Class I, much of the envelope mass has been accreted onto the protostar and the disk has grown. Ices near the protostar completely desorb and grains in the outer envelope stay intact.

evolves into a protoplanetary disk. A protoplanetary disk is a rotating disk of gas and dust around a young star. Within the disk, gas and dust can collide and stick together, gradually growing into larger objects known as planetesimals. These planetesimals can further collide and accumulate to form planets. Lastly, in Class III, planets have formed along with debris such as comets and asteroids.

1.3 GAS-PHASE CHEMISTRY

Gas-phase chemistry in the interstellar medium mostly consists of two-body collisions, single atom or molecule ionization, and photodissociation. Ion-neutral and neutral-neutral reactions are the main reaction routes, with ion-neutral reactions being the most prominent. Three body collision reactions do occur in circumstellar environments but are due to the low densities of the ISM. Three-body reactions do not occur in diffuse, dark, or molecular clouds or hot cores/corinos. For a generalized two-body reaction (A + B → C + D) in the ISM, the rate of reaction is defined as

$$R_{\text{reaction}} = k(T)n(A)n(B)\ \text{cm}^{-3}\text{s}^{-1} \tag{1.1}$$

where $k(T)$ is the rate coefficient, $n(A)$ is the absolute number density of species A, and $n(B)$ is the absolute number density of species B. The rate constant is represented by a modified Arrhenius equation

$$k(T) = \alpha(T/300\ K)^{\beta}\exp(-\gamma/T) \tag{1.2}$$

where γ is the activation barrier and parameters $\alpha, \beta,$ and γ are derived empirically.

Many neutral-neutral two body collisions often have activation barriers that are over 100 K or are endothermic reactions. In the cold temperatures of the ISM, these neutral-neutral reactions become inefficient, making ion-molecule reactions more dominant. Ion-molecule reactions have a small temperature dependence and have many exothermic branches making them more efficient in the ISM at low temperatures. However, it should be noted, that there are still many neutral-neutral reactions that are efficient and important at 10 K.

In this work, two sources of ionization are considered, UV and cosmic-rays. UV ionization is generally described by the Interstellar Radiation Field (ISRF), which is an average value of radiation due to various photon fields such as *OB* stars, cool stars, emission from dust, and the cosmic microwave background (CMB). UV-ionization affects the outer edges of clouds and drives photo-ionization/dissociation reactions. Cosmic-rays are high-energy charged particles that come from external sources such as supernovae, following the galactic magnetic field. These particles are mostly relativistic protons that can travel far into the inner parts of the cloud, mainly ionizing atomic and molecular hydrogen as well as helium. Liberated electrons from cosmic-ray ionization process produces what is called the secondary UV field, where the electrons collide again with more molecular hydrogen releasing UV photons that can ionize and dissociate chemical species.

X-rays are also a source of ionization and similarly produce a secondary UV field. X-rays strongly affect regions such as supernova remnants, Herbig-Haro objects, protoplanetary disks, and regions close to the Galactic Center. However, in some models, x-ray ionization is considered through the cosmic-ray ionization rate.

Once gas-phase species have been ionized by cosmic-rays or UV photons, the ionized species can undergo various types of ion-neutral reactions. Some common types of ion-neutral reactions include proton transfer, H-atom abstraction, radiative association, and charge transfer. These reaction types are as follows:

$$\begin{aligned}
&\text{Proton Transfer} \qquad && \mathrm{AH^+ + B \rightarrow A + BH^+} && (1.3)\\
&\text{H-atom abstraction} \qquad && \mathrm{A^+ + H_2 \rightarrow AH^+ + H} && (1.4)\\
&\text{Radiative Association} \qquad && \mathrm{A^+ + B \rightarrow AB^+} + h\nu && (1.5)\\
&\text{Charge Transfer} \qquad && \mathrm{A^+ + B \rightarrow A + B^+} && (1.6)
\end{aligned}$$

These processes drive ion-chemistry. Two important processes that terminate ion-driven chemistry are radiative recombination of atoms and dissociative recombination:

$$\begin{aligned}
\text{Radiative Recombination} \qquad & \mathrm{A^+ + e^- \rightarrow A} + h\nu && (1.7)\\
\text{Dissociative Recombination} \qquad & \mathrm{ABC^+ + e^- \rightarrow A + B + C} && (1.8)\\
& \mathrm{\rightarrow AB + C,\ etc.} && (1.9)
\end{aligned}$$

All of these reaction types serve to shape the gas-phase chemistry in the ISM, contributing to molecular formation and destruction. However, gas-phase reactions alone cannot fully account for the observed abundances of certain species, particularly complex organics. For example, methanol (CH_3OH) was once thought to form efficiently in the gas phase through the reaction $CH_3{}^+ + H_2O \rightarrow CH_3OH_2{}^+ + h\nu$, followed by dissociative recombination of $CH_3OH_2{}^+$. However, experimental studies have shown that this pathway is inefficient, with only 3% efficiency rather than the original estimate of $\sim$ 50% efficiency (Geppert et al., 2006). This suggests that methanol primarily forms on dust grains followed by non-thermal desorption into the gas phase. Such limitations highlight the need to consider grain-surface chemistry as a complementary mechanism.

1.4 GRAIN CHEMISTRY

Dust grains serve as the sites for COM production and enable chemical reactions that are inefficient in the gas-phase to proceed. These grains, typically submicron-sized ($\sim$ 0.1 μm), are composed of a core, mantle, and surface, as shown in Figure 1.3. The core is composed of silicates and carbonaceous material and is surrounded by an icy mantle that grows over time. The ice mantle is initially formed with simple species such as H_2O, CO, CO_2, NH_3, and CH_4. As the ice mantle grows in layers, called monolayers, it undergoes mantle chemistry that produces more complex species. The outermost layer of the grain is called the grain-surface. On the grain-surface, molecules and/or atoms undergo surface-chemistry and species undergo thermal or non-thermal desorption to put species into the gas-phase. A diagram of grain-chemistry reactions and how the reactions vary through the layers of a dust grain is shown in Figure 1.4. Note that this figure represents chemistry unique to comet chemistry, which includes the effect of galactic cosmic rays and includes monolayers. In the ISM model used in

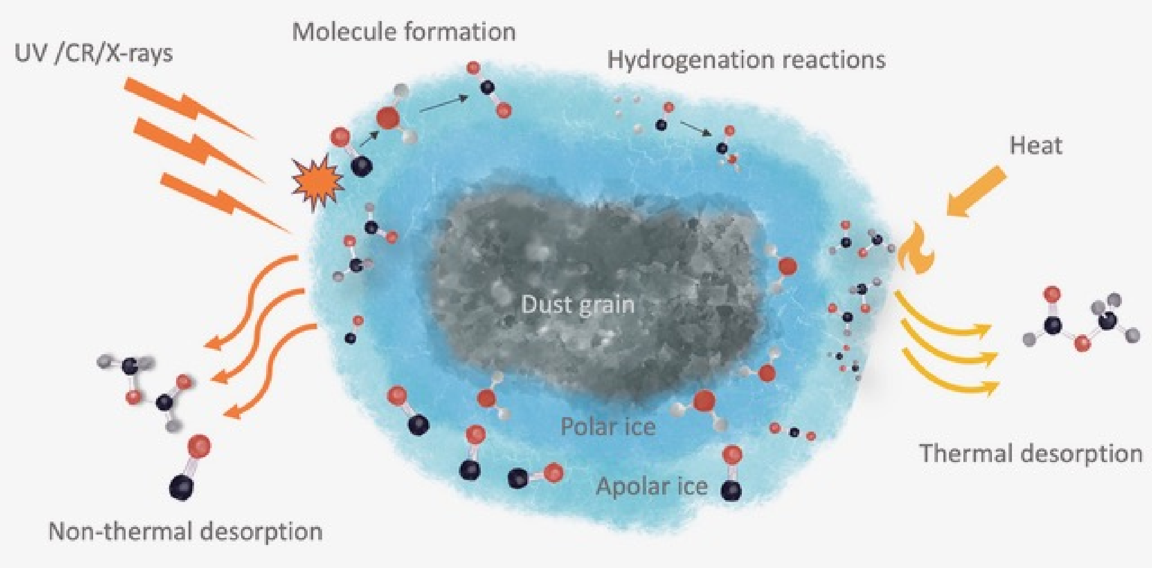

Figure 1.3 Illustration of a dust grain with the core, mantle, and surface. Credit: Rachel Gross

thesis, cosmic-ray driven radiolysis is not included, there is only one monolayer, and no reservoir. However, these processes are shown for completeness in explaining dust grain chemistry. In this section, the overview of grain chemistry is based on Rob Garrod's *Introduction to Astrochemistry* course.

Gas-phase species accrete onto a grain surface, a process characterized by a sticking coefficient, which is the probability that an impinging molecule will remain on the surface rather than bounce back into the gas. Once accreted, whether a species stays on the surface is determined by its binding energy, or also called its desorption energy (E_{des}). The ability of a species to stay on the surface is influenced by the grain temperature, with higher temperatures promoting desorption. The processes of accretion, diffusion, reaction, and desorption are depicted in Figure 1.5.

Accreted species can migrate across a grain through thermal hopping. Diffusion across the grain is limited by a species diffusion barrier, E_{dif}. The hopping rate, k_{hop}, is the site-to-site diffusion rate and is defined as

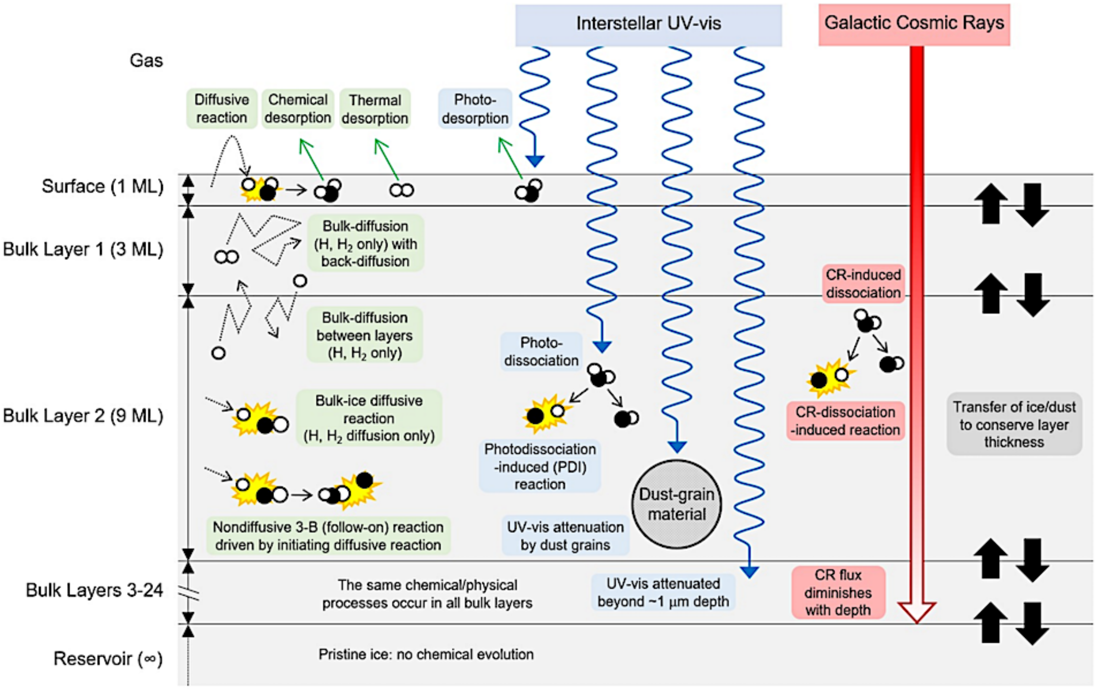

Figure 1.4 Diagram of chemical processes that occur on a dust grain. Cosmic-ray induced radiolysis, monolayer and reservoir dependence are unique to comet chemistry. Credit: Drew Christianson

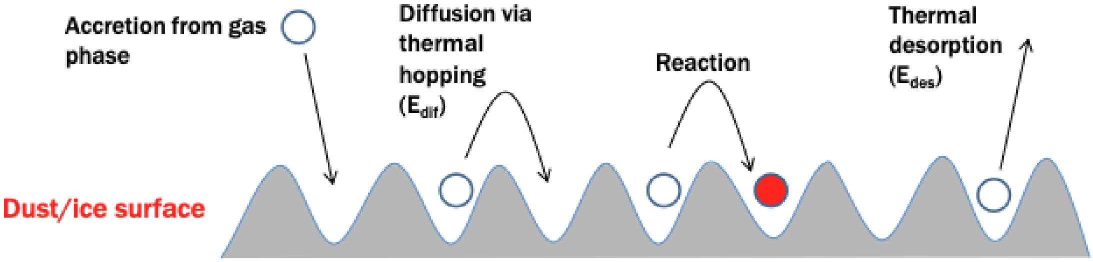

Figure 1.5 Illustration of accretion, diffusion, reaction, and desorption on a grain surface. Credit: Rob Garrod's *Introduction to Astrochemistry* class notes

$$k_{\mathrm{hop}} = \nu(i, E_{\mathrm{des}}) \exp(-E_{\mathrm{dif}}/\mathrm{T}_{\mathrm{gr}}) \tag{1.10}$$

where T_{gr} is the grain temperature. When species encounter each other, their reaction rate, R_{reac}, is given by

$$R_{\mathrm{reac}} = k_{\mathrm{reac}}(A + B)N(A)N(B) \tag{1.11}$$

where $N(A)$ and $N(B)$ are the surface populations of species A and B.

Species on a grain can meet and react in various ways. Langmuir-Hinshelwood mechanism involves the diffusion of two species across a surface where they meet and react, as described above. In addition to diffusion, grain species can meet through other mechanisms such as the Eley-Rideal mechanism and non-diffusive mechanisms such as 3-body reactions, and photodissociation-induced reactions. Eley-Rideal entails a gas-phase species directly reacting with an species on the surface as it adsorbs. In a non-diffusive 3-body reaction, species being formed or adsorbed near each other react instantly. A similar process, an excited 3-body reaction, is where reaction energy released from two species reacting allows enough energy for the third nearby species to instantly react. In photodissociation-induced reactions, a UV or cosmic-ray photons break apart molecules, allowing new species to form from nearby fragments.

Grain-surface chemistry is often more efficient than gas-phase chemistry due to the ability of surface reactions to overcome activation barriers through multiple interaction attempts, energy dissipation, and quantum tunneling. On dust-grains, species stay in close proximity and have multiple opportunities to react, increasing the reaction probability. Grains also act as a thermal reservoir, allowing excess reaction energy to stabilize products that normally would not form in the gas-phase. Additionally, small atoms, particularly hydrogen, can overcome activation barriers through quantum tunneling, allowing more reactions to proceed even at low temperatures.

Through quantum tunneling and non-diffusive mechanisms, grain chemistry can proceed at low temperatures allowing for the build up of simple species and formation of COMs. These mechanisms help explain the presence of COMs in the gas-phase in pre-stellar cores, as has been detected in observations. Grain-chemistry thus provides an alternative pathway for molecular synthesis in the ISM.

1.5 ASTROCHEMICAL MODELING

Astrochemical modeling incorporates mathematics, chemical reaction rates, and in some cases, large-scale physical dynamics, to simulate the chemical processes occurring in astrophysical environments. Such models typically output chemical abundances, reaction pathways, and spectra. Depending on the model, some are able to vary physical conditions of the system such as time, density of the region studied, and other radiation-linked parameters. There is a variety of complexity in chemical models used in the field today, but the majority of models incorporate grain surface chemistry. Such models simulate chemistry in different evolutionary stages of star-formation and offer comparisons to observational data.

In this thesis, I utilize the three-phase astrochemical model MAGICKAL (*Model for Astrophysical Gas and Ice Chemical Kinetics And Layering*; Garrod, 2013). This model treats gas-phase, surface, and mantle chemistry, allowing material from the mantle to push up to the surface. It is fully-active, meaning it accounts for the movement of reactants within the ice layers.

The inputs for MAGICKAL include physical conditions, the chemical network, and initial chemical conditions. Parameters such as hydrogen number density, visual extinction, cosmic-ray ionization rate, and timescale define the physical conditions. The chemical network includes the chemical reaction types described in Sections 1.3

and 1.4. Initial chemical conditions include parameters such as the elemental budgets and chemical ratios, which serve as a starting point for the model. These inputs feed into the main code, where chemical rates are computed and ordinary differential equations (ODEs) governing gas-grain chemistry are solved using an ODE solver. Once the model calculates chemical rates and evolves abundances over time, the results - including abundances, reaction rates, and changes in physical conditions - are stored in output and "order" files. These outputs form the basis for subsequent analysis.

MAGICKAL's combination of an extensive chemical network and a three-phase approach makes it one of the most comprehensive and up-to-date astrochemical models in the field today.

1.6 ASTRONOMICAL OBSERVATIONS

Observations of hot cores and hot corinos allow for direct comparisons to chemical modeling results. Benchmarking chemical models against observational data, such as column densities, helps assess their accuracy and refine reaction networks. Alternatively, chemical modeling aids in interpreting observational results by identifying the model's chemical pathways that reproduce the values obtained from observations.

In this thesis, MAGICKAL results are compared to two types of observations: radio and infrared. Radio observations detect the rotational transitions of gas-phase molecules, making them a useful tool for studying molecular emission in star-forming regions. Notable radio telescopes include the Atacama Large Millimeter/submillimeter Array (ALMA) and the Very Large Array (VLA). Infrared telescopes detect the vibration of molecules, making them particularly valuable for studying ices on grain surfaces. Ground-based IR telescopes, such as the Keck Observatory, and space-based observatories, including the now-retired Spitzer Space Telescope, have provided data on the composition of interstellar ices and dust grain mantles. However, limitations in spectral resolution and sensitivity have restricted their ability to probe deeply embedded regions and detect faint spectral features.

The launch of the James Webb Space Telescope (JWST) offers much higher sensitivity and spectral resolution than ever before. With its Near Infrared Spectrograph (NIRSpec) and Mid-Infrared Instrument (MIRI), JWST allows for the detailed characterization of molecular vibrational modes enabling the detection of complex organic molecules and volatiles on icy grain surfaces. By comparing our model to JWST results, we can now benchmark our models with solid-phase data rather than solely gas-phase.

1.7 OVERVIEW OF THESIS

Astrochemistry occurs throughout the entire life cycle of a star, from a dark molecular cloud to a fully formed planetary system. This thesis focuses on the star-forming part of the process, the collapse of a molecular cloud and formation of a protostar and protostellar disk. I present studies on the two types of star-forming cores, high-mass and low-mass. High-mass cores ($\geq 8M_{\odot}$), hot cores, often form in clusters and are typically chemically rich regions. Low-mass cores, hot corinos, are solar-type forming stars, can form isolated in space or as a product of high-mass star formation, and are much more common. Both of these star-forming cores undergo dramatic physical changes and can harbor complex organic molecules. This thesis traces the formation and evolution of these COMs through astrochemical modeling of their molecular abundances.

Chapter 2 investigates the physical conditions and chemical processes that lead to the observed chemical abundances of $C_2H_4O_2$ isomers methyl formate (MF), glycolaldehyde (GA), and acetic acid (AA) in the NGC 6335I MM1 and MM2 cores, as published in Shope et al. (2024). I examine the effects of visual extinction, hydrogen number density, cosmic-ray ionization rate, and warm-up timescale on the observed MF:GA ratio. Chapter 3 presents a coupled radiation hydrodynamic (RHD) and chemical model of a hot corino, tracing ice chemistry evolution from pre-stellar collapse through protostellar disk formation. The model's column densities are compared to JWST and Spitzer data across the different YSO stages. Chapter 4 extends this analysis by comparing gas-phase and solid-phase column densities from the coupled RHD/chemical model to observational data from four hot corino sources - B335, L483, IRAS 1398, and Ser-emb 7 - using ALMA observations for the gas-phase comparisons, and ice data from recent JWST programs. To account for dust opacity effects on the column densities and to properly compare with observations, I employ the radiative transfer software, RADMC3D, along with a private script made by Dr. Mélisse Bonfand. In Chapter 5, I give my final conclusions for each chapter and draw conclusions across my entire thesis.

Below are the overarching scientific inquiries in this thesis that will be revisited in Chapter 5:

1. What hot core physical conditions yield a high MF:GA abundance ratio? And what chemical pathways yield this high ratio?

2. How does the viewing angle effect the column densities during protostellar disk formation?

3. What implications do the RHD/chemical model results have on the inheritance of COMs throughout the solar-type star formation process?

CHAPTER 2

CHEMICAL MODELING OF $C_2H_4O_2$ ISOMERS IN NGC 6334I

"I'm in the race but I've already won and getting there can be half the fun. So don't stop me 'til I'm good and done. Don't you try to rain on my perfect day."

Legally Blonde, *Perfect Day*

2.1 Abstract

The work presented here has been published in The Astrophysical Journal, 2024, volume 972, page 146, with co-authors Samer J. El-Abd, Crystal L. Brogan, Todd R. Hunter, Eric R. Willis, and Robin T. Garrod (Shope et al., 2024).

Abstract: Gas-phase abundance ratios between $C_2H_4O_2$ isomers methyl formate (MF), glycolaldehyde (GA), and acetic acid (AA) are typically on the order of 100:10:1 in star-forming regions. However, an unexplained divergence from this neat relationship was recently observed towards a collection of sources in the massive protocluster NGC 6334I; some sources exhibited extreme MF:GA ratios, producing a bimodal behavior between different sources, while the MF:AA ratio remained stable. Here, we use a three-phase gas-grain hot-core chemical model to study the effects of a large parameter space on the simulated $C_2H_4O_2$ abundances. A combination of high gas densities and long timescales during ice-mantle desorption ($\sim$125–160 K) appears to be the physical cause of the high MF:GA ratios. The main chemical mechanism for GA destruction occurring under these conditions is the rapid adsorption and reaction of atomic H with GA on the ice surfaces before it has time to desorb. The different binding energies of MF and GA on water ice are crucial to the selectivity of the surface destruction mechanism; individual MF molecules rapidly escape the surface when exposed by water loss, while GA lingers and is destroyed by H. Moderately elevated cosmic-ray ionization rates can increase absolute levels of COM production in the ices and increase the MF:GA ratio, but extreme values are destructive for gas-phase COMs. We speculate that the high densities required for extreme MF:GA ratios could be evidence of COM emission dominated by COMs desorbing within a circumstellar disk.

2.2 Introduction

Methyl formate (MF, $HCOOCH_3$), glycolaldehyde (GA, $CH_2(OH)CHO$), and acetic acid (AA, CH_3COOH) – all structural isomers of formula $C_2H_4O_2$ – are commonly detected in the gas phase toward hot molecular cores and their low-mass analogs, hot corinos, through their cm, mm, and sub-mm wavelength rotational emission (Brown et al., 1975; Cazaux et al., 2003; Hollis et al., 2000; Jørgensen et al., 2012; Mehringer et al., 1997; Jørgensen et al., 2016). In an interstellar context, these three species are known as "complex organic molecules" (COMs), which are defined as carbon-bearing molecules composed of 6 or more atoms (Herbst & van Dishoeck, 2009). As with many other COMs, they are of some prebiotic interest; glycolaldehyde is a sugar-like diose and may be a key RNA precursor (Benner et al., 2019). Methyl formate leads to the synthesis of bio-polymers (Occhiogrosso et al., 2011), while acetic acid is a metabolic intermediate, occurring naturally in body fluids.

Although some COMs may have efficient gas-phase routes to their formation in hot cores (e.g. dimethyl ether, CH_3OCH_3; Garrod & Herbst, 2006), COMs in general are thought to be formed initially on dust-grain surfaces at relatively low temperatures (Garrod et al., 2008; Fedoseev et al., 2015; Ioppolo et al., 2021), and then released into the gas phase as the dust grains are heated by the protostar. Shock-related heating and/or sputtering could also be important in some instances (Jørgensen et al., 2020). Recent observations toward the quiescent Galactic Center cloud G+0.693−0.027 have also revealed a rich COM chemistry related to shock-induced release of dust-grain ice mantles (Zeng et al., 2018, 2020; Rivilla et al., 2022).

The precise mechanisms leading to the production of each individual COM molecule remain under debate, but much of the chemical modeling work on hot cores and corinos over the past decade or so has concentrated on the recombination of functional-group radicals on the dust grains or within their ice mantles (Garrod & Herbst, 2006; Garrod et al., 2008; Garrod, 2013). As some of these radicals, such as CH_3O and CH_2OH, may derive from the same source molecules, i.e. CO, H_2CO (formaldehyde) and/or CH_3OH (methanol), the observational study of structural isomers (e.g. MF and GA) that contain these functional groups may provide constraints on astrochemical models of star-formation chemistry and the underlying chemical mechanisms that they simulate.

Glycolaldehyde was first detected in the ISM toward the high-mass star-forming region Sgr B2(N) by Hollis et al. (2000), who derived ratios for MF:GA:AA of 26:4:1 based on observations with the NRAO 12 m telescope. Follow-up mapping work by Hollis et al. (2001), using the BIMA interferometer, revealed GA to be highly spatially extended in that source (contrary to the compact emission of MF and AA). Those authors determined MF:GA:AA ratios of 52:1:2 specifically toward the Sgr B2(N) core. Detection of GA toward this source was again confirmed by Halfen et al. (2006). The more recent EMoCA survey of Sgr B2(N) by Belloche et al. (2016), using ALMA, yielded ratios 60:7:1 (based on their upper limit for AA) for hot core Sgr B2(N2).

The first detection of glycolaldehyde toward a solar-type protostar (IRAS 16293-2422B; Jørgensen et al., 2012), obtained with ALMA, indicated a ratio of MF to GA of ~10-15. The later ALMA PILS line survey of the same source yielded MF:GA:AA ratios of 93:12:1 (Jørgensen et al., 2016). The EMoCA ALMA line survey of Sgr B2(N2) yielded a MF:GA:AA ratio of 60:7:1 (Belloche et al., 2016) and the ALMA observations of NGC 6334I MM1 sources yielded ratios of 130-380:10:1 (El-Abd et al., 2019).

Based on these and other observations of $C_2H_4O_2$ isomers toward both high- and low-mass star-forming cores, approximate MF:GA:AA ratios of 100:10:1 have been considered broadly representative of these species' relative abundances. However, a divergence from this neat relationship – particularly between MF and GA – was revealed by the study of El-Abd et al. (2019), who examined the abundance ratios of the $C_2H_4O_2$ isomers toward a collection of sources within the massive protocluster NGC6334I, along with values for a variety of other sources taken from the literature. The column densities of MF maintained stable ratios against AA amongst all the sources (see their Figure 2A). However, when comparing the column densities of MF with those of GA, a bimodal distribution was observed among a number of sources, including locations within NGC6334I MM2 (their Figure 2B). Along with some more typical MF:GA ratios of ∼10:1, some of these high-mass cores had MF:GA ratios that were at least an order of magnitude higher. El-Abd et al. (2019) speculated that this bimodal behavior may indicate some unknown competing pathways and/or unknown physical processes in the protostellar environment that must be taken into account in the models in order to explain the observations.

Simulating the observed MF:GA:AA ratios using astrochemical models has been a challenge in the past, due to the models predicting excessive amounts of glycolaldehyde (Garrod et al., 2008; Garrod, 2013). In these past treatments, production of each of the three isomers depended mainly upon diffusive reactions between radicals on grain surfaces, occurring at somewhat elevated temperatures (∼20–40 K; Garrod et al., 2008) during the warm-up of the protostellar envelope. More recently, Jin & Garrod (2020) and Garrod et al. (2022, G22 hereafter) made substantial changes to their astrochemical models, to include nondiffusive grain-surface and bulk-ice chemistry, whereby reactants may be brought together not as the result of diffusion but through some other process, such as a preceding reaction. The earlier Garrod & Pauly (2011) model included a formulation for nondiffusive CO_2 production through the facile process of atomic H diffusion to meet atomic O and instantly react with nearby surface CO.

This type of nondiffusive reaction mechanism, labeled more specifically as a "three-body" (3-B) reaction by Jin & Garrod (2020), was applied to a selection of reactions leading to COM production. Also included was the "photodissociation-induced" (PDI) reaction process, based on a similar treatment used for comet ice chemistry by Garrod (2019), in which a nondiffusive meeting would occur as the result of the spontaneous production of one reactant in the presence of the other via the photodissociation of some precursor molecule near to one of the reactants. Jin & Garrod (2020) also included the Eley-Rideal (E-R) mechanism as a related nondiffusive process, along with a special case of the 3-B process in which the formation energy of the reaction product of the initiating reaction could allow it to overcome the activation energy of the subsequent reaction (known as "three-body excited formation", 3-BEF). The G22 model included the same set of nondiffusive mechanisms, applying them comprehensively to the entire network of surface and bulk-ice reactions.

The inclusion of the 3-B and PDI mechanisms in particular allowed various COMs to be formed effectively in the dust-grain ice mantles or on the grain surfaces, without the need for a direct diffusion mechanism to mediate the reactions. The PDI process correctly allows for photochemistry to occur in the ices even at very low temperatures (see, e.g., Öberg et al., 2009). Furthermore, the 3-B process allows for COMs to be formed as the result of the surface chemistry that builds up the ice mantles under cold and dark cloud conditions, driven mainly by the diffusion of atomic H.

Perhaps most importantly for the $C_2H_4O_2$ isomers, the formation of MF through the 3-B process, as a side-effect of grain-surface methanol production, avoids the problematic CH_3O:CH_2OH photodissociation branching ratio of 1:5 (Öberg et al., 2009). Both of these radicals are instead formed either through hydrogenation of formaldehyde (H_2CO) or by H-abstraction from methanol by H atoms. The latter process, which favors CH_2OH production, is relatively slow, whereas the former process is an essential step in methanol production that strongly favors the production of CH_3O. The models of G22 included further reaction pathways for the formation of glycolaldehyde from glyoxal (HCOCHO), as well as interconversion between glyoxal, glycolaldehyde, and ethylene glycol ($(CH_2OH)_2$), through barrier-mediated H-addition and abstraction reactions with atomic H, using activation barriers partially based on rates provided by Simons et al. (2020), who based their rate parameters on calculations by Álvarez Barcia et al. (2018). These additional pathways were found to contribute significantly to the total production of glycolaldehyde.

As with past hot-core chemistry models by those authors, G22 used a physical treatment deemed to be representative of the evolution of a generic, star-forming source. The treatment divides the evolution into two stages; the first stage involves a cold, free-fall collapse to the final density of the hot core, during which the ice mantles form. In the second, warm-up stage, the gas and dust temperatures rise over time, allowing the ice mantles ultimately to be desorbed into the gas phase, typically at temperatures greater than around 100 K.

The timescale of warm-up has typically been the only free parameter considered in these models. However, Barger & Garrod (2020) conducted a more substantial survey of the parameter space of the physical treatment, using a model that did not include nondiffusive grain-surface/ice chemistry. They found that the combination of the chosen warm-up timescale and cosmic-ray ionization rate (CRIR) could produce broad, and somewhat degenerate variation in gas-phase and grain-surface abundances for COMs.

CRIR values are rather poorly constrained in the ISM in general, with recently determined values diverging from the canonical value of $\zeta \simeq 10^{-17}$ s^{-1}, reaching as many as three orders of magnitude higher, dependent on source (e.g. Caselli et al., 1998; van der Tak et al., 2006; Favre et al., 2018). Theoretical work indicates that the CRIR from Galactic cosmic rays should be dependent on H_2 column density (e.g. Padovani et al., 2009; Rimmer et al., 2012; Padovani et al., 2018; Fitz Axen et al., 2021). More recent theoretical and observational work provides evidence that high-energy, ionizing particles may be produced locally within protostellar sources (e.g. Padovani et al., 2018; Cabedo et al., 2023; Sabatini et al., 2023). Thus, the operative CRIR used in models of particular sources may require a far more localized tuning than the simple adoption of a generic CRIR value.

Other physical conditions, such as the gas density and visual extinction behavior, may also influence the gas and grain chemistry in a meaningful way: the former determining the rate of growth of ice mantles and the rates of gas-phase chemistry; the latter determining the dust-grain temperature and the degree of photo-processing of the ice mantles to form or destroy COMs.

Here, we present hot-core chemical model results from a broad physical parameter space using the MAGICKAL chemical model as presented by G22, with a particular emphasis on the search for parameter values that lead to large MF:GA abundance ratios and the possible emergence of bimodal behavior between different models in the grid. The general effects of each physical parameter on the model are also considered. The main parameters explored within the context of the usual physical treatment are the peak (final) hydrogen number density (n_{H}), cosmic ray ionization rate (ζ), and the warm-up timescale (t_{wu}) of the hot core. The influence of changing the initial visual extinction ($A_{\mathrm{v,initial}}$) of the collapsing cloud is also tested.

By varying these parameters, we investigate which parameter combinations best reproduce the observed isomer abundance ratios in the twelve sources of the star forming regions MM1 and MM2 in the massive protocluster NGC6334I (El-Abd et al., 2019). The results are also compared with molecular abundance ratios obtained by the

PILS and EMoCA line surveys of IRAS 16293 and Sgr B2(N), respectively, presented in Appendix A.1.

A summary of the general effects of each parameter on the model is given in Section 2.4.4.

2.3 Methods

The gas-grain chemical kinetics model MAGICKAL is used to simulate the time-dependent chemistry in hot cores. MAGICKAL (*Model for Astrophysical Gas and Ice Chemical Kinetics And Layering*; Garrod, 2013) is a three-phase model used to calculate and solve the coupled rate equations that govern the chemistry occurring in the gas, grain-surface, and bulk-ice phases. Except for the chemical network employed, the chemical model used here is identical to the "`final`" model setup presented by G22. Notable features of that model include both diffusive and nondiffusive grain-surface and bulk-ice chemical reaction mechanisms. While all chemical species on the grains are in principle allowed to diffuse on the surface, diffusion within the bulk ice is limited to H and H_2, which are assumed to exist in interstitial positions within the ice matrix. Bulk-ice diffusion rates for H and H_2 are based on barriers twice the strength of the surface barriers. Tunneling rates are used (based on a barrier width of 3.2Å, corresponding to a majority water ice) in cases where those rates exceed the thermal diffusion rates. As per G22, the surface binding energy of atomic H is taken as 661 K and the diffusion barrier as 243 K, corresponding to the average values calculated by Senevirathne et al. (2017) for H on ASW. As in G22, the sticking coefficient for all species is unity. The reader should refer to G22 for detailed descriptions of all of the main features of the model.

The chemical network used here is that presented by Garrod & Herbst (2023) for their M4 setup; it is identical to that of G22, except that it includes some additional gas-phase proton-transfer reactions between the protonated forms of various COMs and certain other species that have proton affinities larger than that of ammonia. For the $C_2H_4O_2$ isomers and related species, the network may be considered essentially identical to that of G22; the most important proton-transfer reactions for these species involve ammonia (NH_3) and methanol (CH_3OH), and these were already present in the G22 network.

The chemical network includes a total of 749 gas-phase species, and 318 (neutral) grain-surface species, with the same number of species also traced in the bulk ice. There is a total of 22,401 reactions and processes, including transfer of atoms/molecules between the surface and bulk ice. This number also includes surface/bulk reactions that are replicated between the diffusive and various nondiffusive meeting mechanisms; the number of unique reactions on the grains (regardless of meeting mechanism or surface/ice phase) is 1,279. From this uniform chemical treatment, a grid of chemical model runs is constructed, based on the variation of a selection of key physical parameters related to the dynamical and thermal evolution of a hot core.

2.3.1 Physical model

The physical model has two consecutive stages of evolution: the first stage represents the isothermal, free-fall collapse of a dense core from an initially diffuse/translucent state, with the gas temperature held constant at 10 K. The initial density for each stage-1 run is set to the same value for all model runs ($n_{\rm H,initial} = 3000$ cm^{-3}; Garrod et al., 2022), while the final gas density achieved during the collapse is varied in the grid. As the density increases during the collapse, the visual extinction rises according to $A_{\rm V} = A_{\rm V,initial}(n_{\rm H}/n_{\rm H,initial})^{2/3}$, where $A_{\rm V,initial}$ assumes a value of either 2 or 3 mag (Garrod et al., 2022). These initial extinction and density values are consistent with typical values cited for translucent and/or clump material in interstellar clouds (Snow

& McCall, 2006; Bergin & Tafalla, 2007), within which a core would grow. The visual extinction is capped at a value of 500 mag., which is sufficiently large to exclude effectively all external UV-vis photons. The dust temperature in stage 1 varies as a function of visual extinction (Garrod & Pauly, 2011), falling from ∼16 – 8 K or from ∼14.7 – 8 K, for initial visual extinctions of 2 or 3 mag., respectively. The dust grains are assumed to have a uniform radius of 0.1 μm, following past models. Chemical evolution during the collapse stage continues until the final density is reached, which occurs after ∼0.95 Myr. Most of the initial dust-grain ice build-up occurs during the collapse stage.

Stage 2 of the physical model involves the gradual warm-up of the gas and dust, while all other physical quantities are held steady (using their final values from stage 1). The dust temperature initially rises from 8 K until it reaches the 10 K initial temperature of the gas; T_{gas} and T_{dust} then rise together, until they reach a final temperature of 400 K. The characteristic warm-up timescale, t_{wu}, which is varied within the model grid, corresponds to the time taken to reach 200 K, following past models. Parameter values used in the grid of models are shown in Table 2.1 and described below.

2.3.2 Model Grid Parameters

Based on the general modeling treatment described above, we build a grid of chemical models adopting a range of physical parameter values (Table 2.1), in order to gauge the response of the chemistry beyond the analysis of G22. The standard parameter values used by those authors are shown in bold in the table. Aside from visual extinction, parameter values used in the model grid are distributed logarithmically around the standard values.

In the stage-1 setups, we adopt final hydrogen number densities, n_{H}, from 2×10^6

to 2×10^{10} cm^{-3}, in order to capture a range of possible gas-density values; typical hot-core gas densities are greater than 10^7 cm^{-3} (Choudhury et al., 2015), while the typical, representative values adopted in our past models have ranged from 2×10^7 – 2×10^8 cm^{-3}. To provide some additional parameter coverage within the latter range, a logarithmically intermediate value of 6.32×10^7 cm^{-3} was included in the grid. The chosen final density, which is achieved at the end of stage 1, carries over to the corresponding stage-2 model runs.

The initial visual extinction in stage 1 is set at either 2 or 3 mag. G22, who tested these two values within a large grid of chemical parameter variations, found that the choice of $A_{\mathrm{V,initial}}$ made only a modest difference to simple ice abundances. In order to restrict the potentially large parameter space of the model grid, we choose to test only those same two values. By the end of the collapse stage, each model reaches at least 150 mag. of extinction, meaning that the post-collapse A_{V} value has minuscule influence over the chemical rates. The choice of initial visual extinction therefore has no practical effect on the behavior of the stage-2 models other than through the chemical abundances that they inherit from the stage-1 runs.

We also vary the cosmic ray ionization rates (CRIR), as most COM production on the grains is influenced in some degree by cosmic-ray induced UV photodissociation, while much of the post-desorption gas-phase destruction of COMs involves ion-molecule chemistry. The past chemical models of Barger & Garrod (2020) suggested that CRIR values greater than the canonical value (of order 10^{-17} s^{-1}) were most appropriate when compared with observed COM abundances, although the models used to draw this conclusion did not include any non-diffusive grain chemistry. In the present model grid, the CRIR ranges from an order of magnitude below our basic value of 1.30×10^{-17} s^{-1}, to two orders of magnitude greater, with values distributed logarithmically. Each chosen CRIR value is applied throughout both stage 1 and 2,

Table 2.1 Key physical parameters varied in the chemical model grid: initial visual extinction ($A_{\rm v,init}$), hydrogen number density ($n_{\rm H}$), cosmic ray ionization rate (ζ), and warm-up timescale ($t_{\rm wu}$). The table also indicates whether the parameter directly influences the physical behavior of the Stage-1 model, the Stage-2 model, or both. "Standard" values used in the Garrod et al. (2022) models are shown in bold. The standard warm-up timescale indicated corresponds to the *medium* value used in past models.

$A_{\rm v,init}$ (mag)	$n_{\rm H,final}$ (cm^{-3})	ζ (s^{-1})	$t_{\rm wu}$ (yr)
Stage 1	Stages 1 & 2	Stages 1 & 2	Stage 2
2	2.00×10^{6}	1.30×10^{-18}	2.00×10^{4}
3	2.00×10^{7}	4.11×10^{-18}	3.56×10^{4}
	6.32×10^{7}	**1.30×10^{-17}**	6.32×10^{4}
	2.00×10^{8}	4.11×10^{-17}	1.12×10^{5}
	2.00×10^{9}	1.30×10^{-16}	**2.00×10^{5}**
	2.00×10^{10}	4.11×10^{-16}	3.56×10^{5}
		1.30×10^{-15}	6.32×10^{5}
			1.12×10^{6}
			2.00×10^{6}

and does not vary with time or column density in these models.

For the warm-up timescales used in stage 2, seven values are adopted, ranging from 2×10^4 to 2×10^6 yr, based around the *medium* warm-up timescale used by G22 and others. Here we choose not to use the *fast* (5×10^4 yr) and *slow* (1×10^6 yr) values adopted in past models, as they fall between the logarithmically distributed values that we have adopted to ensure comparability within the grid. They are, however, within the extremes of the range of values tested here.

The full grid of physical parameters is varied to test every combination; this results in a total of 84 stage-1 models. For each stage-1 run, nine different stage-2 runs are calculated (varying warm-up timescale), such that the initial chemical and physical state of each of those nine is inherited from the same stage-1 run. The total number of stage-2 model runs is thus 756.

2.3.3 Observational Comparisons

Quantitative comparisons of the model results with observational values can be used to determine which model best matches a particular source, thus indicating which physical conditions are most applicable in the context of our chemical model grid. The calculation of a matching parameter between a particular set of observational data and each chemical model may thus help to guide the explanation for the distinct chemical behavior observed between different sources.

Of particular interest is to identify any physical/chemical origins for the bimodal behavior seen in the MF and GA column densities observed by El-Abd et al. (2019) in data from two Band 7 ALMA tunings toward the protocluster NGC 6334I. In their work, the column densities of MF, GA, and AA were obtained for lines of sight within the two sources in NGC 6334I, MM1 and MM2. Spectra were extracted from nine positions in MM1 and from three positions in MM2, for a total of twelve locations observed in this star forming region.

These observations were done with a full-width half-power beam size of 20 arcsec, spectral resolution of 1.1 km s^{-1}, and rms per channel of 2.0 mJy $beam^{-1}$. More details can be found in El-Abd et al. (2019), Hunter et al. (2017), McGuire et al. (2017) and Brogan et al. (2018).

Matching parameter

For each comparison of a model with a set of observational data, a matching parameter, m, is calculated with the generalized form:

$$m = \sqrt{m_1^2 + m_2^2 + ...} \tag{2.1}$$

where the number of terms depends on the number of molecular species used in the comparison. Each m_i represents the quality of match for an individual quantity (molecule or molecular ratio) of index i, given by:

$$m_i = \log\left(\frac{R_{\rm mod,i}}{R_{\rm obs,i}}\right). \qquad (2.2)$$

The value $R_{\rm mod,i}$ indicates a model-produced quantity and $R_{\rm obs,i}$ is the corresponding observed value. Since observational molecular abundance information is obtained as a set of column densities, while the chemical models instead produce local fractional abundances, $R_{\rm obs,i}$ and $R_{\rm mod,i}$ are taken as molecular ratios with respect to some standard molecule. The value m_i thus indicates the number of orders of magnitude by which the modeled molecular ratio deviates from the observed ratio, while m is the root-mean-square of all such individual values, with $m = 0$ being a perfect match. Other forms of matching parameter are of course possible; however, the chosen method ensures that, in the case of a non-perfect match, a model producing a single, large divergence is disfavored versus a model that produces many small divergences from the observed values.

Following G22 and related studies in which output data from the MAGICKAL model has been compared with gas-phase observational abundance values for hot cores/corinos, we use the *peak* gas-phase abundance produced by the stage-2 models for comparison with observations. Thus, for example, the modeled MF:GA ratio is calculated as the ratio of the peak gas-phase MF abundance to the peak gas-phase GA abundance. Although there is a degree of variation, most COMs reach their peak gas-phase abundances within a similar range of times/temperatures in the models. We therefore assume that this region/time of peak molecular abundance is representative of the observed emission from these molecules (see e.g. Belloche et al., 2019). Furthermore, the destruction of gas-phase COMs is dominated by ion-molecule reactions, and the rates of destruction for most COMs of interest in the models (including the $C_2H_4O_2$ isomers) are similar; this means that the post-peak molecular ratios remain fairly stable over time. In the absence of a spatial model of the distribution of the COMs, we therefore assume that the ratio of peak abundances between different molecules should be directly comparable with observed column density ratios.

The matching parameter described by Eqs. (2.1) and (2.2) is used in several different ways to determine the quality of match of various models with particular observational datasets, as described below.

Comparisons with NGC 6334I

As the main focus of this work, comparisons of the chemical models with lines of sight toward NGC 6334I focus specifically on the MF:GA and MF:AA ratios. Thus, Eq. (2.1) requires only m_1 and m_2, which take values:

$$m_1 = \log\left(\frac{R_{\mathrm{mod,MFGA}}}{R_{\mathrm{obs,MFGA}}}\right)$$
$$m_2 = \log\left(\frac{R_{\mathrm{mod,MFAA}}}{R_{\mathrm{obs,MFAA}}}\right),$$

where $R_{\mathrm{mod,MFGA}}$ is the MF:GA ratio from the model, and $R_{\mathrm{obs,MFGA}}$ is the observed ratio, etc. In cases where the observational value of MF:GA is based on an upper limit for the column density of GA, models that achieve a ratio that matches *or exceeds* the observed value are assigned a perfect match parameter, i.e. $m_1 = 0$.

Table 2.2 lists the twelve sight-lines observed in NGC 6334I and their respective column density ratios of MF to GA and MF to AA. For each of the sight-lines, a best-match model is sought. Three different procedures are used to determine these

Table 2.2 MF:GA and MF:AA ratios for the 12 sources in NGC 6334I observed by El-Abd et al. (2019). Listed alongside each source is an identification number used exclusively in this paper to more easily indicate the best-match model for each source as shown in Figs. 2.5–2.6. Beside the observed molecular ratios are shown the best-match modeled ratios based on matching procedures #1, #2 and #3, and the relevant model parameters. Note that procedure #3 has the same best-match results as fitting procedure #2 for the MM1 sources.

ID #	Source name	Observed		Best-Match Model			Model Conditions			
		MF:GA	MF:AA	MF:GA	MF:AA	m-value	$A_{v,init}$ (mag.)	n_H (cm^{-3})	ζ (s^{-1})	t_{wu} (yr)
	Matching Procedure #1 - No Constraints									
1	NGC 6334I MM1-i	15.0	21.8	15.0	21.8	0.002368	2	2×10^{10}	1.30×10^{-15}	2.00×10^{4}
2	NGC 6334I MM1-ii	15.6	33.7	16.0	35.9	0.02372	3	2×10^{10}	1.30×10^{-17}	3.56×10^{5}
3	NGC 6334I MM1-iii	16.5	9.80	15.2	7.1	0.1459	3	2×10^{10}	4.11×10^{-18}	6.32×10^{5}
4	NGC 6334I MM1-iv	37.8	87.5	39.2	89.0	0.01701	3	2×10^{10}	4.11×10^{-17}	3.56×10^{5}
5	NGC 6334I MM1-v	45.4	6.17	63.9	7.0	0.1573	3	2×10^{10}	4.11×10^{-18}	2.00×10^{6}
6	NGC 6334I MM1-vi	13.3	12.7	11.2	14.8	0.1005	2	2×10^{8}	1.30×10^{-15}	1.12×10^{5}
7	NGC 6334I MM1-vii	25.2	18.4	25.0	17.6	0.02000	3	2×10^{10}	1.30×10^{-15}	3.56×10^{4}
8	NGC 6334I MM1-viii	30.1	34.3	33.1	34.3	0.04116	3	2×10^{10}	1.30×10^{-17}	6.43×10^{5}
9	NGC 6334I MM1-ix	35.3	54.1	37.4	51.8	0.03132	2	2×10^{6}	1.30×10^{-16}	1.12×10^{6}
10	NGC 6334I MM2-i	>158	21.7	140	18.2	0.09528	2	2×10^{10}	1.30×10^{-15}	1.12×10^{5}
11	NGC 6334I MM2-ii	>146	15.8	235	16.5	0.01753	2	2×10^{10}	4.11×10^{-18}	2.00×10^{6}
12	NGC 6334I MM2-iii	>374	28.3	577	43.1	0.1822	2	2×10^{9}	4.11×10^{-16}	3.56×10^{5}
	Matching Procedure #2 - Fixed combination of ζ and $A_{V,initial}$									
1	NGC 6334I MM1-i	15.0	21.8	15.0	21.8	0.002368	2	2×10^{10}	1.30×10^{-15}	2.00×10^{4}
2	NGC 6334I MM1-ii	15.6	33.7	15.0	21.8	0.2378	2	2×10^{10}	1.30×10^{-15}	2.00×10^{4}
3	NGC 6334I MM1-iii	16.5	9.80	11.2	14.8	0.2461	2	2×10^{8}	1.30×10^{-15}	1.12×10^{5}
4	NGC 6334I MM1-iv	37.8	87.5	32.2	21.9	0.6064	2	2×10^{10}	1.30×10^{-15}	3.56×10^{4}
5	NGC 6334I MM1-v	45.4	6.17	38.1	15.4	0.4041	2	2×10^{9}	1.30×10^{-15}	1.12×10^{5}
6	NGC 6334I MM1-vi	13.3	12.7	11.2	14.8	0.1005	2	2×10^{8}	1.30×10^{-15}	1.12×10^{5}
7	NGC 6334I MM1-vii	25.2	18.4	19.0	19.5	0.1263	2	2×10^{9}	1.30×10^{-15}	6.32×10^{4}
8	NGC 6334I MM1-viii	30.1	34.3	32.2	21.9	0.1974	2	2×10^{10}	1.30×10^{-15}	3.56×10^{4}
9	NGC 6334I MM1-ix	35.3	54.1	32.2	21.9	0.3951	2	2×10^{10}	1.30×10^{-15}	3.56×10^{4}
10	NGC 6334I MM2-i	>158	21.7	140	18.2	0.09528	2	2×10^{10}	1.30×10^{-15}	1.12×10^{5}
11	NGC 6334I MM2-ii	>146	15.8	140	18.2	0.06224	2	2×10^{10}	1.30×10^{-15}	1.12×10^{5}
12	NGC 6334I MM2-iii	>374	28.3	140	18.2	0.4690	2	2×10^{10}	1.30×10^{-15}	1.12×10^{5}
	Matching Procedure #3 - Separate combination of ζ and $A_{V,initial}$ combinations for MM1 and MM2									
	MM1 sources: same as matching procedure #2									
10	NGC 6334I MM2-i	>158	21.7	235	16.5	0.1203	2	2×10^{10}	4.11×10^{-18}	2.00×10^{6}
11	NGC 6334I MM2-ii	>146	15.8	235	16.5	0.01753	2	2×10^{10}	4.11×10^{-18}	2.00×10^{6}
12	NGC 6334I MM2-iii	>374	28.3	235	16.5	0.3102	2	2×10^{10}	4.11×10^{-18}	2.00×10^{6}

best matches, based on several further constraints, as summarized below:

1. No constraints: Matching procedure runs through all models and independently selects the best matching (lowest m) model for each sight-line.
2. Uniform cosmic-ray ionization rate and initial extinction: Assumes that all sight-lines in NGC 6334I must have a shared ζ-value. A shared $A_{\mathrm{V,initial}}$ value is also selected, to indicate a common background/ambient visual extinction for the cloud in its initial state.
3. Separate MM1 and MM2: Same constraints as procedure 2, but allows different CRIR values for MM1 versus MM2 sight-lines.

For matching procedure #1, all 756 stage-2 models are considered in one run through. Each model is analyzed for its peak abundance ratios of MF, GA, and AA and for each of the twelve sources; whichever model out of the 756 has the best MF:GA and MF:AA match compared to observations is deemed the best-match model. Although this method technically finds the best matches between models and observations, it ignores that the local CRIR in NGC 6334I may be the same or very similar between each sight-line.

For matching procedure #2, the determination of the best-match model for each sight line is done separately for each ζ-value tested in the models, in combination with one or other $A_{\mathrm{V,initial}}$ value, on the assumption that the same ζ applies throughout NGC 6334I, and all material originated from a cloud of the same or similar degree of exposure to external ionizing photons. For each of the 14 [ζ,$A_{\mathrm{V,initial}}$] combinations, a model dataset of six density values and nine warm-up timescales (a total of 54 models) is compared with each of the twelve NGC 6334I sight-lines. The best match for each source is found within that set. An overall m-value is then determined for this

[ζ,$A_{\mathrm{V,initial}}$] combination, whereby the m-values of the best matching models for each of the sources are combined according to Eq. 2.1. The [ζ,$A_{\mathrm{V,initial}}$] combination with the lowest overall m-value is considered the best overall match to the observations. The best-match model for a particular source is then considered to be the one drawn from this overall best-match combination.

For matching procedure #3, the same constraints as matching procedure #2 are used, but sources MM1 and MM2 are considered separately, allowing them to settle on independent best-match [ζ,$A_{\mathrm{V,initial}}$] combinations.

The above-described matching procedures are based on comparisons of molecular ratios, but by themselves they do not take account of the absolute abundance values of individual species. In principle, this could lead to models being chosen as a good/best match while not otherwise being suitable as a description of hot-core chemistry. To avoid the consideration of models with unrealistically low molecular abundances, thresholds were set for the two key molecules methyl formate and methanol. Models for which the gas-phase methyl formate abundance falls below $10^{-9}\mathrm{n_H}$, are removed from consideration as best-match models. Methyl formate abundances in hot cores are typically on the order of $10^{-8}\mathrm{n_H}$ or higher (Bisschop et al., 2007). As a further constraint, we also remove models with peak methanol abundances less than $10^{-6}\mathrm{n_H}$, although models that fail one condition typically fail both.

2.4 RESULTS

In order to gain insight into the chemistry influencing MF ($HCOOCH_3$), GA ($CH_2(OH)CHO$), and AA (CH_3COOH) in the models, we first consider the time-dependent abundances of these isomers, as well as the chemically related COMs ethanol (C_2H_5OH) and dimethyl ether (CH_3OCH_3). We focus here on three particular models from the grid, corresponding to (i) the "standard" conditions used by G22 (and shown in Ta-

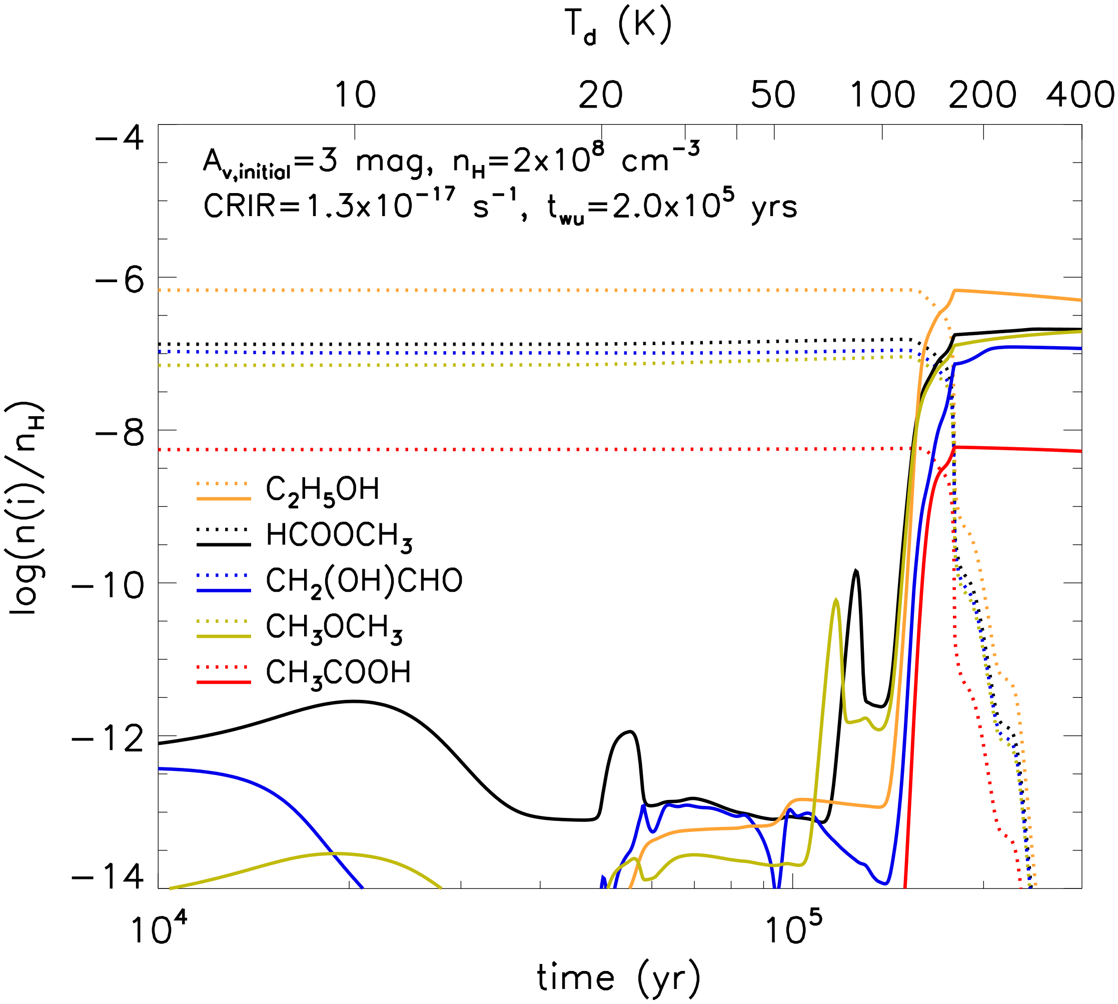

Figure 2.1 Selected fractional abundances produced by the model with standard physical conditions as considered by Garrod et al. (2022)
(shown in Table 2.1 where $A_{v,init} = 3$ mag, $n_{H,final} = 2 \times 10^8$ cm^{-3}, CRIR $= 1.3 \times 10^{-17}$ s^{-1}, and $t_{wu} = 2 \times 10^5$ yr). Gas (solid lines) and grain (dotted lines) abundances of MF (black), GA (blue), AA (red), ethanol (orange), and dimethyl ether (green) with respect to total hydrogen are shown.

ble 2.1); (ii) a model with different conditions including more extreme density and CRIR values; and (iii) a model with somewhat lower CRIR, high gas density, and a long warm-up timescale. The first of the three models (Fig. 2.1) is essentially the same as that presented by G22, for which a broader range of chemical abundance plots may be found in their Figures 8 and 9 (stage 1) and their Figure 11 (stage 2). The question of which model best matches each observed source is explored below in Sec. 2.4.5; however, we note that model (ii) considered here (Fig. 2.2) corresponds to the best match for the NGC 6334I MM2 sources using matching procedure #2. Model (iii) (Fig. 2.3) is the best match for MM2 sources using matching procedure #3 (see Sec. 2.4.5 for further discussion). Here we describe the broad features and differences in the abundance behavior shown in the three figures, digging deeper into the underlying chemistry in Secs. 2.4.1–2.4.3.

Fig. 2.1 shows COM abundances during the stage-2 (warm-up) evolution of the "standard" model (i) setup. For consistency between models, results are plotted beginning at time 10^4 yr, when the dust and gas temperatures are $\sim$8 K and 10 K, respectively. The plot continues until the end-time of the model, which occurs at $\sim 2.85 \times 10^5$ yr, when gas and dust temperatures of 400 K are reached.

The COMs shown in the plot are largely formed on the dust grains during stage 1 (a depiction of the net production rates through stages 1 and 2 may be seen in Figure 13 of G22). The early production of each of the grain-surface ice species (dotted lines) derives a substantial contribution from radical-association reactions on the surfaces as the ices build up under low-temperature and high gas-density conditions. In the case of AA and ethanol, photochemistry in the young, thin, grain-surface ices is also important. Solid-phase GA abundances are intertwined with the abundances of the related glyoxal (HCOCHO) and ethylene glycol ($HOCH_2CH_2OH$) molecules, via H-atom addition and abstraction. The solid-phase abundances of these COMs are stable

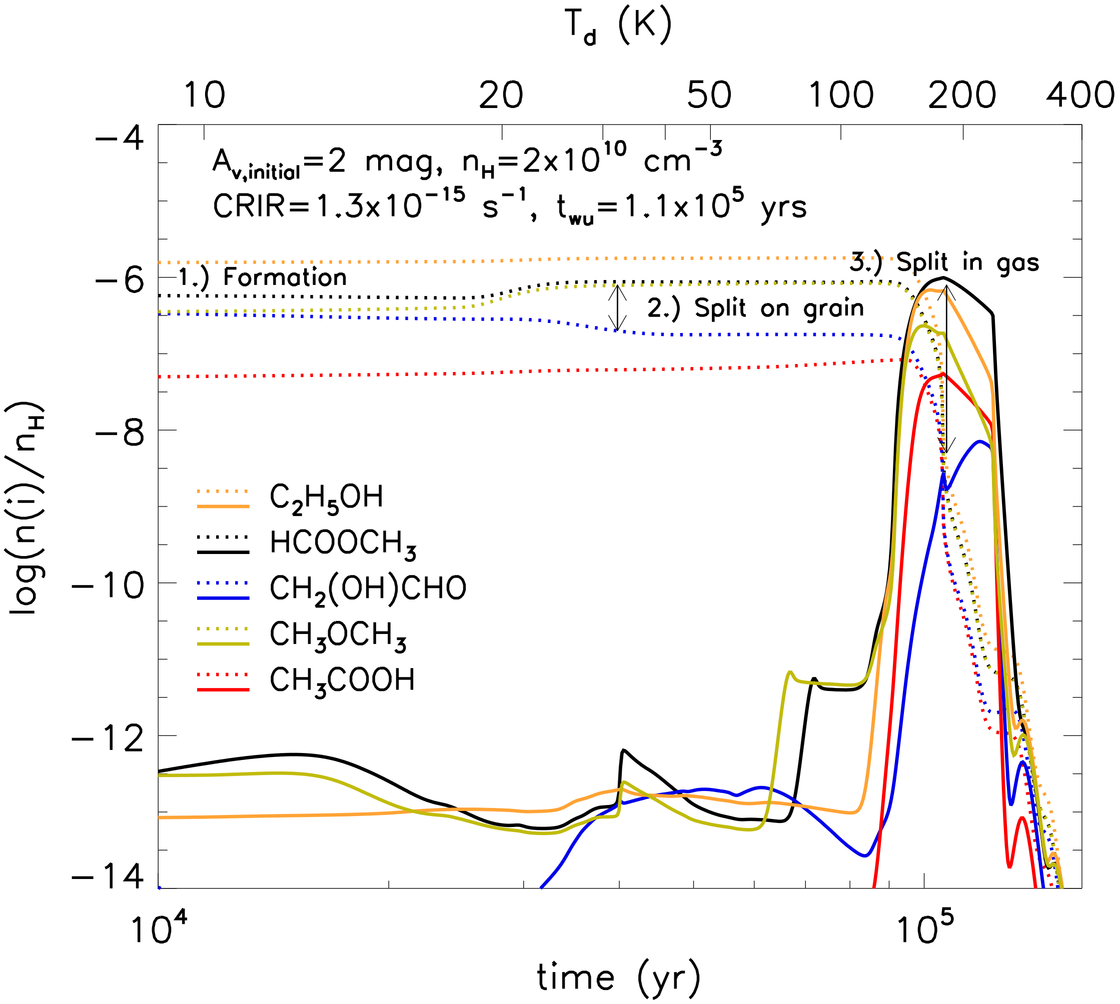

Figure 2.2 As Fig. 2.1, with results from an alternative model with higher gas density (2×10^{10} cm^{-3}), CRIR (1.3×10^{-15} s^{-1}), lower initial visual extinction (2 mag), and shorter warm-up timescale (1.1×10^5 yrs), producing a more substantial divergence in grain-surface and gas-phase MF and GA abundances. The model shown is the best-match model for NGC 6334I MM2 sources, using matching procedure #2. Color scheme as per Fig. 2.1. Note the different conditions from Fig. 2.1 as stated at the top of the figure.

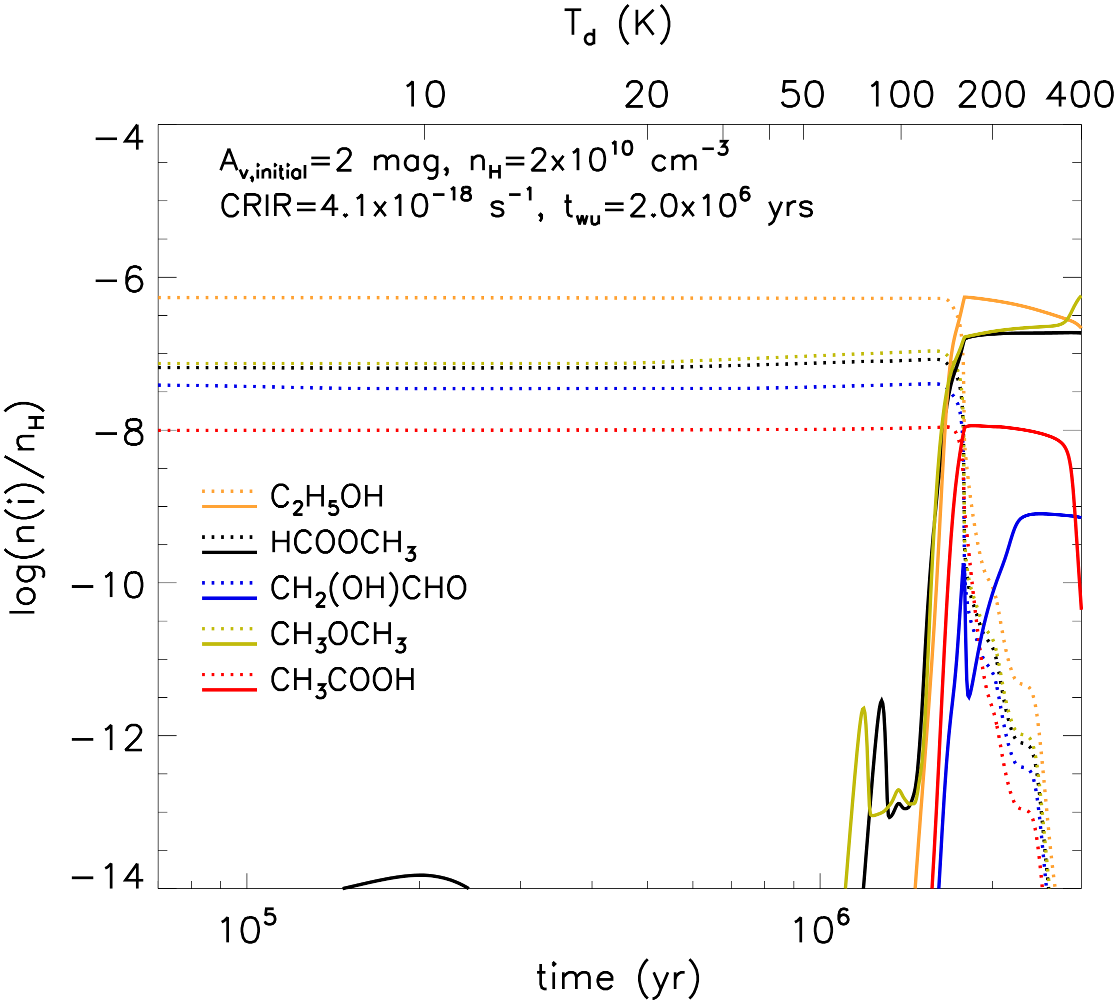

Figure 2.3 As Fig. 2.1, with results from an alternative model that is the best match for NGC 6334I MM2 sources with matching procedure #3. Same color scheme as per Fig. 2.1 and Fig. 2.2. Note the different conditions from Fig. 2.2 as stated at the top of the figure, with a lower CRIR (4.1×10^{-18} s^{-1}) and longer warm-up timescale (2.0×10^6 yrs). The gas density remains high at 2×10^{10} cm^{-3} and the initial visual extinction at 2 mag.

until the ices begin to sublimate.

The gas-phase abundances of the COMs (solid lines of the same colors) reach their peaks at temperatures above ∼120 K, when the ices begin to sublimate. Some of the gas-phase abundances do not reach their full peak values until the large water-ice component has fully desorbed, which occurs at a temperature around 160 K. Release of some species at yet higher temperatures can also occur, either due to their own high binding energies, or because of trapping beneath species that have not yet desorbed. Gradual declines in gas-phase abundances toward the end of the model are caused by protonation of the COMs by abundant molecular ions such as H_3O^+; protonated COMs are destroyed by dissociative recombination with electrons. The peak gas-phase abundances of the $C_2H_4O_2$ isomers in Fig. 2.1 are in the correct order with respect to observational values, i.e. MF is most abundant and AA is the least abundant. The MF:GA ratio is ∼1.7.

Fig. 2.2, showing results from model (ii) – which has 100 times higher stage-2 gas density and 100 times higher cosmic ray ionization rate – reveals some interesting differences. Firstly, all of the solid-phase COM abundances have been enhanced during their earlier formation in stage 1; the stronger secondary UV field, produced by CR excitation of gas-phase H_2, leads to a greater abundance of radicals on the grain surfaces and in the ices, which then recombine to form more COMs. Meanwhile, toward the end of stage 2, following the desorption of the COMs into the gas phase, the higher CRIR drives a more rapid ion-molecule chemistry. Protonation and dissociative recombination destroy these species completely before the end of the model is reached, in spite of the timescale of this model being slightly shorter than the "standard" value of model (i).

Two other important features are also notable; whereas in model (i) the solid-phase abundances of MF and GA seem to track in parallel with each other, more or less

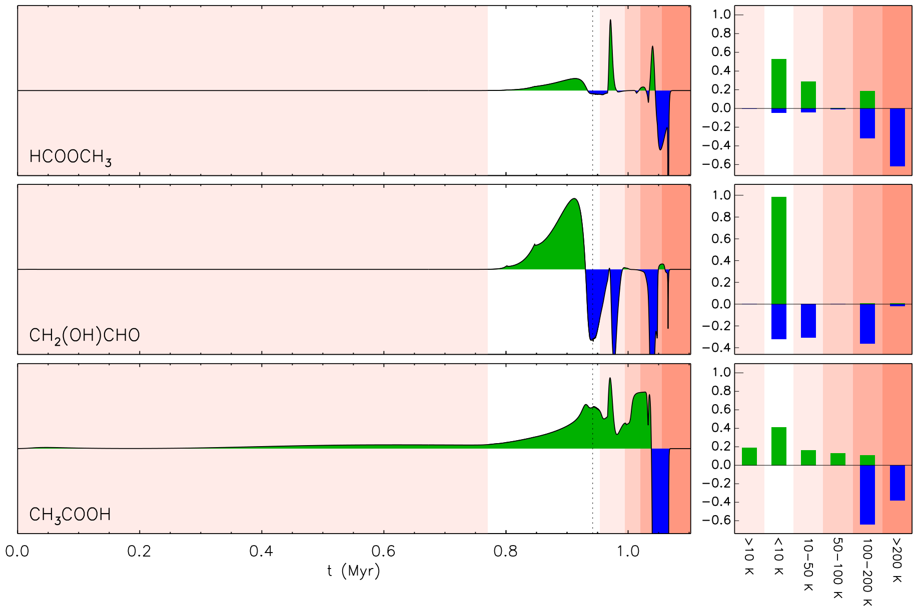

Figure 2.4 **Left panels:** Net rate of change of the three $C_2H_4O_2$ isomers, as a function of time, for the best-matching model to the NGC 6334I MM2 abundances using match parameter #2. Rate of change for each molecule is summed over all phases, and is shown in arbitrary units. Net formation is highlighted in green and net destruction in blue. The dotted vertical line indicates the transition from stage 1 to stage 2. **Right panels:** The same data is shown as a fraction of the total net formation (i.e. the sum of all green areas), for each of six temperature regimes occurring through stages 1 and 2. Different background shading indicates each temperature regime. Destruction bars (blue) are also normalized to the total net formation.

preserving their abundances from stage 1, in model (ii) these two species diverge at a temperature around 20–30 K, with MF increasing in abundance while GA decreases. Dimethyl ether behaves similarly to MF at this point in the model.

An even greater divergence is then seen when the ices desorb into the gas phase; while MF abundance is essentially preserved between its peak solid-phase abundance prior to desorption and its subsequent gas-phase peak value, GA drops drastically during the desorption period, so that it never reaches the same abundance in the gas phase as it had in the ice just prior to desorption. The gas-phase MF:GA ratio in this model is 140:1.

In Fig. 2.3, in which the results of the high-density, long warm-up timescale model (iii) are shown, the solid-phase abundances are again more stable until sublimation occurs, although the abundances are generally lower (excluding dimethyl ether) than in the "standard" model (i), due to the slightly lower CRIR that results in weaker stage-1 production of radicals. The large split in peak gas-phase abundances of MF and GA is retained in this high-density model, with a MF:GA ratio of 235:1. Methyl formate abundance actually grows during the period of strong desorption, rising above the prior solid-phase abundance. Although the CRIR is a little lower than standard, the long timescale of this model means that ion-molecule chemistry diminishes some of the molecules more substantially by the end of the model run than in the "standard" case.

2.4.1 Early Formation Mechanisms

Here we provide a more detailed description of the formation mechanisms of the $C_2H_4O_2$ isomers occurring mainly during stage 1 (collapse), which are in general responsible for much of the formation of these molecules under typical conditions.

Figure 2.4 (left panels) shows the net rate of formation (green) and destruction (blue) for MF, GA, and AA at times throughout model (ii), from the beginning of stage 1 through the end of stage 2. These rates correspond to the sum of formation and destruction of the same molecule over all phases (i.e. gas, grain-surface and bulk-ice). The dotted line in the plot separates stage 1 from stage 2. The right panels of the same figure indicate the integrated formation and destruction in several broad temperature regimes, normalized to the total formation. The first two regimes correspond mainly to stage 1 of the models; most of the net production (shown in green) of MF, GA, and AA is seen to occur during stage 1, when dust temperatures are below 10 K and the gas density is reaching its peak, resulting in rapid adsorption of gas-phase atoms and molecules onto the grain surfaces.

At these early stages in all three models, methyl formate is predominantly formed on the grain surfaces through the 3-B reaction of radicals HCO and CH_3O, in which either the HCO or the CH_3O radical is formed close to its reaction partner. For example,

$$[\mathrm{H} + \mathrm{CO}] + \mathrm{CH_3O} \rightarrow \mathrm{HCO} + \mathrm{CH_3O} \tag{2.3a}$$

$$\mathrm{HCO} + \mathrm{CH_3O} \rightarrow \mathrm{HCOOCH_3} \tag{2.3b}$$

In this case, the initiating reaction between H and CO occurs through a typical diffusive mechanism, following the adsorption of H onto the grain surface from the gas phase.

In model (ii), the high CRIR results in a large gas-phase abundance of atomic H (due to CR-induced dissociation of H_2), around 100 times the model (i) value. The rate of H adsorption onto the grains is commensurately higher than in model (i), leading to more efficient hydrogenation of CO and H_2CO, and a higher production rate for MF. The final gas density in model (ii) is also higher by a factor of 100, but this high density is reached very late in stage 1, after much of the gas-phase CO used to form COMs has already frozen out onto the grains.

As discussed by G22, the chemical network includes the 3-BEF mechanism, which in this case allows the energy of formation of the just-formed CH_3O radical to overcome the activation energy barrier to immediate reaction with nearby CO. The product of this reaction, the radical CH_3OCO, may then recombine with atomic H through a normal diffusive reaction to produce MF:

$$\mathrm{H} + \mathrm{CH_3OCO} \rightarrow \mathrm{HCOOCH_3} \tag{2.4}$$

Under certain circumstances, this process may temporarily become the dominant MF-formation process in the model, but overall it contributes only on the order of a few percent maximum to the total production of methyl formate.

As seen in Fig. 2.4, in model (ii) there is some substantial production of MF at later times and higher temperatures during stage 2. This is described in detail in Secs. 2.4.2 and 2.4.3.

For glycolaldehyde, the formation mechanisms are more complicated, as there is interconversion between glyoxal (HCOCHO), glycolaldehyde (GA), and ethylene glycol ($(CH_2OH)_2$), which affects the overall production and destruction of GA. Atomic H may react with each of the three species, mediated by activation energy barriers, to add or abstract a hydrogen atom, producing a radical. Reaction of H with such a radical may further add or subtract an H atom to the structure (without an activation barrier). As discussed by G22, the degree of interconversion is thus dependent on a number of factors, including how rapidly the ice is building up on the grain surface.

However, ultimately it is the radical recombination reactions:

$$\mathrm{HCO + HCO \rightarrow HCOCHO} \tag{2.5}$$

$$\mathrm{HCO + CH_2OH \rightarrow CH_2(OH)CHO} \tag{2.6}$$

$$\mathrm{CH_2OH + CH_2OH \rightarrow (CH_2OH)_2} \tag{2.7}$$

that add new material into this triad of related species. During the cold stage 1 when most of this material is formed, each of these reactions occurs mainly via the 3-B mechanism. The CH_2OH is formed mostly through the barrier-mediated diffusive surface reaction

$$\mathrm{H + CH_3OH \rightarrow CH_2OH + H_2} \tag{2.8}$$

More detail on the interconversion between glyoxal, glycolaldehyde, and ethylene glycol can be found in G22. Essentially all of the net positive production rates of GA in model (ii) occur at the end of the cold collapse stage; GA production continues at later times in moderate amounts, but it is not sufficient to overcome photoprocessing in the ice, as well other destructive mechanisms described below.

AA production occurs mainly during stage 1 also; however, unlike MF and GA, the earliest stages of ice formation at low visual extinction also provide an opportunity for external UV to drive AA production. Much of this production occurs through the two reactions

$$\mathrm{CH_3CO + OH \rightarrow CH_3COOH} \tag{2.9}$$

$$\mathrm{CH_3 + COOH \rightarrow CH_3COOH} \tag{2.10}$$

Several mechanisms can produce the radical CH_3CO, including H-abstraction from acetaldehyde (CH_3CHO) and the barrier-mediated reaction of CH_3 with CO, while OH abundance is maintained by the photodissociation of water ice. The CH_3 radical is an intermediate in the hydrogenation of atomic C to form methane, while the COOH radical can be produced by the destruction of formic acid (HCOOH).

The high CRIR in model (ii) has more dissociating photons than in the other two models, even at high visual extinction, meaning that PDI-driven AA production continues strongly even into stage 2. This behavior, shown visually in Fig. 2.4 may be contrasted with that presented by G22 (in their Figure 13) for "standard" conditions, in which most AA is formed at very early times in stage 1 when external UV is still able to penetrate.

2.4.2 Grain-Surface Split in MF and GA Abundances

Early in the stage-2 evolution of model (ii), as seen in Fig. 2.2, MF and GA abundances stay relatively steady in relation to each other, showing a slight downward trend with time that is due to gradual CR-induced photodissociation of the ices. Then, as marked in the figure, beginning at a temperature of $\sim$17 K (or a time in stage 2 around 2.5×10^4 yr), a split appears in the behavior of grain-surface GA and MF; GA abundances falls, while that of MF (and of dimethyl ether) rises. This divergence is complete by around 35 K ($\sim 4.5 \times 10^4$ yr). The new MF:GA ratio is retained in the ice until strong desorption occurs at temperatures >100 K. Note that the grain-surface abundances shown in the figures correspond to the total ice present in the bulk ice and the outer surface layer combined.

This divergence in grain-surface abundances is a bulk-ice chemistry effect. Below $\sim$17 K, bulk diffusion of atomic H is slow, and is governed by tunneling between interstitial sites in the ice matrix. Above this temperature, thermal diffusion takes over, with a rate that grows rapidly as the grains become warmer. This change in

H-diffusion behavior occurs in all of the stage-2 models; however, in model (ii), with its 100-times higher CRIR than the standard value, there is also a much greater production rate for atomic H, making the change in H mobility in the bulk ice much more important. This combination of high production-rate and high mobility of atomic H manifests in several chemical effects in model (ii).

We first consider the rise in MF abundance. There is more MF present at the beginning of stage 2 in model (ii) than there is in e.g. model (i), for reasons described above. But there is also a correspondingly higher abundance of the related radical $COOCH_3$. At low temperatures ($<$17 K) the latter species is formed in the bulk ice when MF is attacked by atomic H at the aldehyde end of the molecule. Although this reaction is mediated by an activation energy barrier ($\sim$4000 K in this model; Good & Francisco, 2002), the site-to-site diffusion rate of atomic H is low enough that reaction through the barrier is competitive with the alternative outcome in which the H atom simply diffuses away before reaction occurs. Thus, when an H-atom meets MF in the ice, it efficiently produces the CH_3OCO radical:

$$\mathrm{H} + \mathrm{HCOOCH_3} \rightarrow \mathrm{CH_3OCO} + \mathrm{H_2} \tag{2.11}$$

When another H atom meets with this radical, MF is reformed through reaction 2.4, which is assumed to have no substantial activation energy barrier.

The H in the bulk ice is formed exclusively through CR-induced photodissociation of the various molecules in the ice, dominated by H_2O. At low temperatures, the formation and destruction of $HCOOCH_3$ and $COOCH_3$ through reactions with H are fairly slow, and the ratio of MF to its related radical is stable.

As the temperature climbs above 17 K, thermal diffusion of atomic H takes hold; the efficiency of the H-abstraction reaction falls, because when an H-atom meets a

MF molecule, diffusion away from MF becomes more probable than reaction. At the same time, the rate for the barrierless reaction of H with $COOCH_3$ increases with temperature, due to faster diffusion.

In model (ii), in which there is a lot of H being formed through CR-induced photodissociation of various species, the balance shifts strongly at $T>17$ K, such that most $COOCH_3$ in the ice is converted to MF without being converted back. Furthermore, in model (ii), there is already a lot of this radical present in the ice ($HCOOCH_3$:$COOCH_3 \simeq 2$) at the beginning of stage 1, thus the MF abundance rises substantially when this conversion takes place. In model (i) and other models with relatively low CRIR, there is less H being produced in the ice during both stages 1 and 2, meaning that the H-abstraction/addition cycle is already much slower (by $\sim$100 times). As a result, there is a lower initial ratio of $HCOOCH_3$ to $COOCH_3$ in the ice, while the change in diffusion behavior with temperature has only a very mild influence on that ratio during the stage-2 warm-up.

In Figure 2.4, which shows production rates from model (ii), we see net formation of MF not only in the <10K regime but also again in the 10-50K (and 100-200K) temperature regime, occurring sharply in the $\sim$17–30 K range.

A similar effect involving H addition and abstraction is also seen to influence the abundance of solid-phase dimethyl ether (CH_3OCH_3) in model (ii).

For GA, much of the fall in its ice abundance in model (ii) occurs at around 25–35 K. In relative terms, this decline is a little less drastic than the rise in MF. In this case, conversion into ethylene glycol ($(CH_2OH)_2$) and, to a lesser extent, glyoxal (OHCCHO) accounts for much of the loss in glycoladehyde. The lowest barriers against either abstraction or addition of atomic H (several radical structures are possible) are quite low, on the order of 1000 K or less. This means that, upon the meeting of H and GA in the ice, a reaction is the most likely outcome versus diffusive escape of the H atom, even at temperatures as high as ∼35 K. Until this temperature approaches, conversion of GA continues effectively, while above this temperature, the diffusion of H away from GA is more likely than overcoming the barrier to addition or abstraction. While the H could in principle return to the GA to attempt reaction again, it is more likely to meet and react with a radical elsewhere in the ice, which would occur immediately upon meeting, rather than being hampered by a barrier.

In Figure 2.4, we see that for GA there is a net destruction at <10K and 10-50K, with the latter negative spike being representative of the destruction of GA described here.

For the models with low CRIR, such as model (i), again the lower production rate of atomic H in the bulk ice means that the conversion of GA is much slower than in model (ii), such that it has very little practical effect on its abundance.

Thus, the divergence in grain-surface abundances of MF and GA in models with high CRIR is driven by the changing mobility of H atoms in the ices, amplified by the greater production of H by the CR-induced photodissociation of other molecules. The divergence stabilizes again when the H atoms become too mobile for barrier-mediated reactions to be efficient versus recombination with radicals in the ice.

As described by G22, we note that in the present models diffusive radical-radical reactions play only a small part in the production of the COMs of interest here, although non-diffusive reactions between radicals are very influential. The diffusion of atomic H, either on the ice surface or in the bulk ice, is important in driving many of these non-diffusive reactions, by producing new radicals in close proximity to others.

2.4.3 Gas-Phase Split in MF and GA Abundances

The split in gas-phase abundances of MF and GA in model (ii), also marked in Fig. 2.2, is more drastic than the earlier grain-surface split. This divergence is ultimately related less to the higher CRIR of model (ii) than to the higher gas density. However, the reason that MF and GA are differently affected is their different binding energies.

As the dust temperature begins to rise during stage 2, some of the more volatile components of the ice start to desorb, such as CO and CH_4. However, in this three-phase chemical model, as material is lost from the surface monolayer, material in the bulk ice beneath is exposed, becoming the new surface. While some of this material is also composed of volatiles, other molecules with much higher binding energies, such as water, are also present. Thus, as volatiles leave, the upper layer becomes more concentrated in non-volatiles, leading to a trapping effect that acts to retain species of lower binding energy that would otherwise desorb at that temperature. The more volatile species are trapped until temperatures are achieved at which the less volatile species holding them in place may themselves thermally desorb.

Because of this effect, much of the total ice content is retained on the grain surfaces until temperatures around 120 K are achieved (see G22), when water itself begins to sublimate substantially from the grains. In this model, water has a binding energy of 5700 K, while the value for MF is 4210 K (Burke et al., 2015), based on desorption from a water-ice surface. Hence, as soon as water in the upper monolayer desorbs, any uncovered MF immediately desorbs, giving it a very short lifetime on the surface. Although it takes some time for the water to desorb entirely from the grains (the process being essentially complete at a temperature of ~160 K; G22), MF nevertheless desorbs as soon as it is exposed on the surface.

Conversely, GA has much greater binding energy (5630 K; Burke et al., 2015) compared with MF, similar to that of water in this model, due to the hydroxyl group on the molecule that allows it to form hydrogen bonds with the water surface. As a result, GA has a lifetime on the water surface that is similar to water itself, taking some time to fully desorb.

During its much longer residence time, GA comes under a sustained chemical attack before it can leave the surface. In particular, H atoms from the gas phase may stick briefly to the surface, where they can diffuse to meet reactants, including GA. In spite of the activation energy barriers, H may react with GA to abstract another H atom, forming H_2. Much of the abstraction occurs at the aldehyde end of the molecule, producing the $CH_2(OH)CO$ radical. The latter may recombine with another H atom to re-form GA, or it may thermally desorb with a slightly lower binding energy than GA (as assumed in this model). Alternatively, an H-atom may be abstracted from the other end of the GA molecule, producing a radical that can react with another H atom to produce glyoxal (OHCCHO). The latter may also desorb more easily from the icy grain surface than GA.

Thus, much of the what was previously glycolaldehyde actually desorbs in a different form, so that the post-desorption gas-phase GA abundance is lower than the pre-desorption solid-phase abundance. Other radicals on the surface, freed by the gradual desorption of the water overlayers, may also react with the radicals formed from the hydrogen-atom attack on GA molecules, producing alternative species with higher binding energies.

Because the attacking H atoms derive from the gas phase, the degree of destruction experienced by GA molecules prior to complete desorption from the grains is strongly dependent on the gas density, which determines the rate of adsorption. The high CRIR also increases the abundance of H atoms in the gas, which has a lesser but significant effect on the rate of GA destruction.

In summary, the trapping of MF beneath the water-ice surface, at temperatures above its own desorption temperature, means that the lifetime of any individual MF molecule on the surface is very short. Conversely, because GA is retained on the grains for longer, i.e. with individually longer surface lifetimes, it is strongly susceptible to attack by H atoms adsorbed from the gas, before it is able to escape. The effect of H-atom attack on GA is accelerated primarily by the higher gas density, and secondarily by the higher CRIR, in model (ii).

We note also that in model (iii), as shown in Fig. 2.3, a similar gas-phase split is seen between MF and GA. In this case, although the CRIR is much smaller, the gas density is high, while the warm-up timescale is long. This leads to a longer period over which GA is exposed on the hot grains prior to desorption, while the high density supplies atomic H rapidly to the surface.

The MF abundance in model (iii) is seen to increase further during the desorption period, beyond what is even present on the grains. A similar – and related – effect is seen for dimethyl ether at around the same time. It should be noted that the abundances of both MF and DME in the ices in model (iii) are lower than those in model (ii). However, the very low CRIR in model (iii) means that the radicals CH_3OCO and CH_3OCH_2 that build up in the ice are far less likely to encounter an H atom with which they may recombine, allowing them to build up in the ices until late times. When each of these radicals becomes exposed to the surface, and to the accompanying flux of H atoms from the gas phase, they rapidly recombine to produce MF and DME, respectively, which then thermally desorb.

2.4.4 General Effects of each Parameter on MF:GA:AA ratios

The effects of cosmic-ray ionization rate, initial visual extinction, final hydrogen number density and warm-up timescale on the broad trends in MF:GA and MF:AA ratios are now considered.

Fig. 2.5 maps the logarithm of the MF:GA ratio produced by each model in the parameter space, based on the comparison of peak molecular abundances as described in Sec. 2.3.3. The panels are labeled A–N, with each panel corresponding to a particular combination of ζ and $A_{\rm v,init}$; the upper row corresponds to $A_{\rm v,init}$=2, and the lower to $A_{\rm v,init}$=3. Within each panel, the MF:GA ratio is mapped as a color contour as a function of $n_{\rm H}$ and $t_{\rm wu}$. The contours are based on the model values at positions marked with diamonds. The highest abundance ratios are shown in red, and the lowest in purple, while regions of white space indicate models that do not meet the abundance thresholds for methanol and MF as described in Section 2.3.3. Fig. 2.6 maps the MF:AA ratio in an identical way. In panel J of each figure, the "standard" model setup indicated in Table 2.1 is marked with a square symbol. Other symbols shown in these figures are described in Sec. 2.4.5.

Cosmic-Ray Ionization Rate, ζ

When comparing the fourteen contour plots for each of the two molecular ratios, basic trends emerge as to which conditions yield higher abundance ratios. In general, high MF:GA ratios are achieved toward the top-right of each panel (high density and long warm-up timescale). For a fixed $n_{\rm H}$ and $t_{\rm wu}$ combination (i.e. a fixed coordinate in any panel), increasing the CRIR (shifting panels from left to right) tends to increase the MF:GA ratio. This occurs as the result of the grain-surface split in MF and GA abundances described in Sec. 2.4.2. As noted in Sec. 2.4, higher ζ-values also tend to produce more COMs overall in the ices, especially during the initial collapse stage.

However, the absolute abundances of methanol, MF and GA suffer in the gas phase with the more extreme ζ values, due to rapid ion-molecule destruction rates. In the extreme cases, this causes those models to produce very low peak COM abundances, hence excluding them from the matching procedures. This is especially true for models with long warm-up timescales, in which the desorption of COMs from the grains in outpaced by their gas-phase destruction. As a result, the highest MF:GA ratios produced by acceptable models are found not for the highest CRIR case but for the next two lower values.

Toward the lower end of the CRIR distribution (left panels), most of the parameter space produces MF:GA ratios that are somewhat less than one order of magnitude, but the MF abundance is always greater than that of GA. The "standard" model itself falls into this lower MF:GA ratio regime.

The MF:AA ratio is fairly stable within each panel, but varies slightly for CRIRs of 1.3×10^{-16} s^{-1} and higher. The MF:AA ratio is low under conditions of lower CRIR, and increases as the CRIR increases, until the MF:AA ratio drops off again with high CRIR. The fact that the MF:AA ratio is so stable within each panel shows that the final gas density and the warm-up timescale have little influence. Since these are the two model parameters that are most closely associated with the stage-2 chemical behavior, one may infer that the MF:AA ratio is essentially fixed at early times, during the stage-1 collapse. The "standard" model (panel J) has a MF:AA ratio of 32, which is in the mid-range of values determined in NGC 6334I.

Initial Visual Extinction, $A_{\mathrm{v,init}}$

The parameter space includes visual extinctions of 2 and 3 mag, which in Figs. 2.5 and 2.6 are arranged as the top seven panels (A–G) and lower seven panels (H–N), respectively. A slight decrease in the abundance ratios of both MF:GA and MF:AA in the 3 mag models in comparison to those at 2 mag suggests that there is only a very slight influence from the visual extinction on the distinct behavior of MF, GA, and AA. In stage 1 of the model, the initial visual extinction determines the degree to

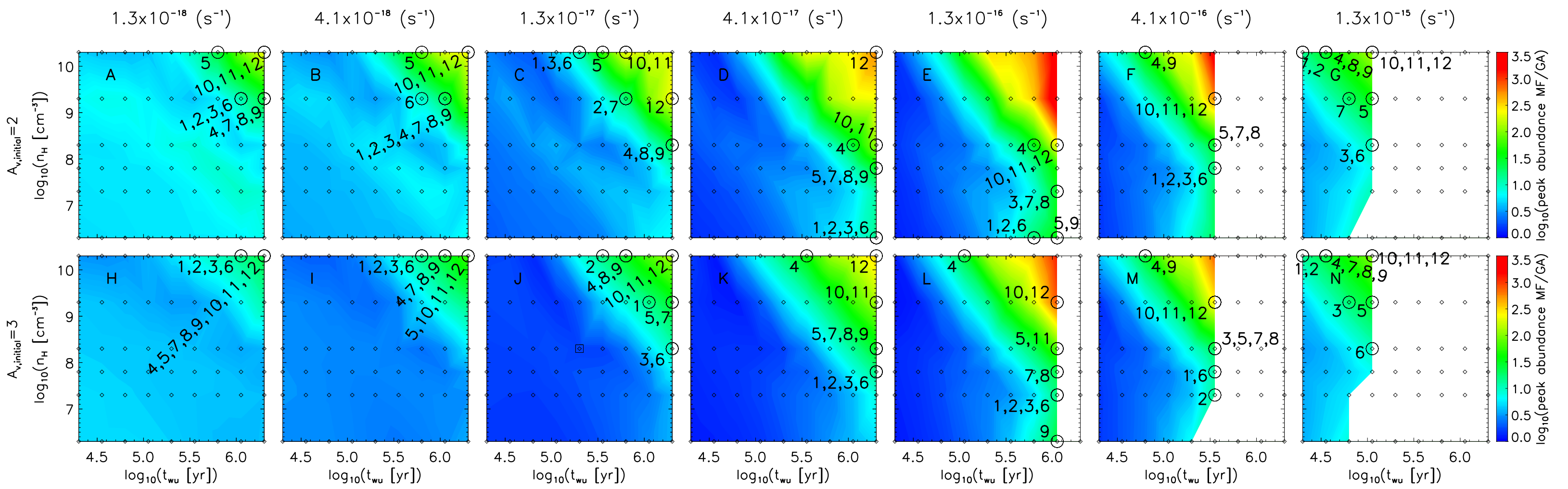

Figure 2.5 The ratio of the peak abundances of methyl formate to glycolaldehyde produced by the entire chemical model grid. Each panel corresponds to a specific cosmic-ray ionization rate, ζ and initial visual extinction, $A_{v,init}$. Within each panel, models varying in final gas density and warm-up timescale are indicated with diamonds. The "standard" model is also marked with a square. The best-matching models for the sources in NGC 6334I, using matching procedure #2, are marked with circles, with numbers indicating the ID number of the source as listed in Table 2.2.

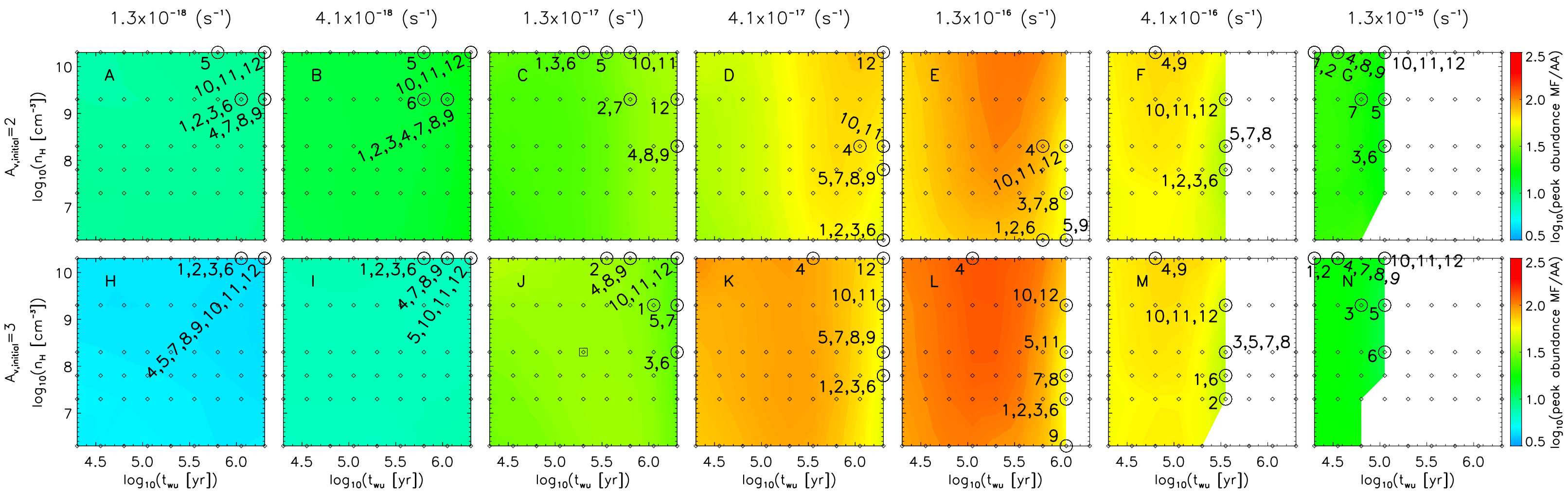

Figure 2.6 As Fig. 2.5, but showing the ratio of methyl formate to acetic acid.

which the molecules are shielded from outside UV radiation during the early stages of collapse. All three $C_2H_4O_2$ isomers are formed strongly in stage 1 of the model.

The slightly higher UV flux seen early in the models with $A_{v,init}$=2 might, on its own, be expected to lead to somewhat higher photodissociation-driven production of the three isomers in the ice, especially AA. Meanwhile, similar mechanisms might be expected also to destroy those same species to some extent. However, a more important effect related to the visual extinction is the dust temperatures achieved at early times during the collapse. The initial dust temperature in the $A_{v,init}$=3 case is ~14.7 K, where it remains through much of stage 1, only falling substantially as higher density/extinction conditions (around $n_H > 4 \times 10^3$ cm^{-3} and $A_v > 3.5$) build up toward the end of the collapse. In the $A_{v,init}$=2 case, the initial dust temperature is ~16 K at early times, and higher dust temperatures than in the $A_{v,init}$=2 case is maintained through most of the collapse phase. As a result, with the lower A_v, the grain-surface diffusion of hydrogen in particular is faster throughout the stage-1 model, including near the end of the model run, when the gas density is highest.

This has an important impact on grain-surface radical-radical chemistry, which occurs mainly through the nondiffusive 3-B process, with dominant COM production occurring under the low-temperature conditions (< 10 K) that obtain toward the end of the stage-1 collapse phase. The higher dust temperatures reached in the $A_{v,init}$=2 case lead to more rapid recombination of radicals with mobile atomic H, reducing the surface coverage of those radicals, thus reducing the likelihood that the spontaneous production of another radical in close proximity would lead to COM production. Conversion of CO to CO_2 is also more efficient at higher temperatures, especially above 12 K (see Garrod & Pauly, 2011), leading to fewer CO-related COMs.

Under low CRIR conditions (panels A and H), while the MF:AA ratio is higher in the $A_{v,init}$=2 case (panel A), the overall abundances of MF, GA & AA are collectively lower due to the weaker production at the highest density conditions. In the $A_{v,init}=3$ case (panel H), although the production of AA at early times is weaker due to the lesser UV field, the stronger production of AA late in the collapse stage overcomes this effect, so that ultimately this model has a smaller MF:AA ratio.

In the low CRIR models, the MF:GA ratio also tends to be marginally smaller in the $A_{v,init}=3$ case. The difference in MF:AA ratio between the two A_v values becomes somewhat less important at higher CRIR values, which drives more COM production in the bulk ices throughout the entire stage 1 and stage 2 evolution.

Hydrogen Number Density, n_H

Fig. 2.5 shows the most extreme MF:GA ratios values being achieved in high-density, long warm-up timescale models (i.e. $n_H > 2 \times 10^8$ cm^{-3} and $t_{wu} > 10^5$ yr). As described in Sec. 2.4.3, the principal mechanism leading to these extreme values relates to the long lifetimes of GA molecules on the grain surfaces as the ices desorb, compared with those of MF. The latter easily escapes the hot grains as soon as it is exposed on the ice surface, due to its lower binding energy, while GA cannot escape rapidly enough to avoid chemical reactions with atomic H that is abundant in the gas phase. However, this effect only occurs if there is sufficiently high gas density for adsorption of atomic H, and its subsequent reaction with GA, to compete effectively with the thermal desorption of GA. Furthermore, for this process to substantially reduce the GA abundance during desorption, the warm-up timescale must be long enough that the grain-surface GA is not lost to the gas phase too rapidly, giving the atomic H time to destroy it. In each panel of Fig. 2.5, the MF:GA ratio is fairly stable in most of the (density-timescale) parameter space, only rising above a value ~3 when some combination of density and warm-up timescale is achieved (crudely defined as $\log(n_H) + \log(t_{wu}) \gtrsim 14$).

In Fig. 2.6 it may be seen that within each panel, the MF:AA ratio changes little with density, in strong contrast to the MF:GA ratio. The reason for this is that, while AA has an even greater binding energy (6615 K; Burke et al., 2015) than GA, the H-abstraction reaction with atomic H has a much greater barrier (3710 K in this model, based on Evans-Polanyi fitting; see Garrod, 2013) than for its structural isomers, due to the abstraction occurring from a methyl group rather than the aldehyde group present in MF and GA.

Warm-up Timescale, t_{wu}

In Figure 2.5, the highest MF:GA ratios tend to concentrate around the medium to long warm-up timescales (i.e. $t_{\mathrm{wu}} > 10^5$ yr). These longer warm-up timescales tend to prolong the gas-phase chemistry occurring in any given temperature range; for MF, GA and AA, that chemistry is primarily destructive. However, a similar effect is seen in prolonging the period over which the grain-surface GA may be attacked by atomic H that adsorbs from the gas phase, preferentially lowering the ultimate peak gas-phase abundance of GA, and thus raising the MF:GA ratio.

Under high CRIR conditions ($> 10^{-16}$ s^{-1}), warm-up timescales greater than $\sim 10^6$ yr can be too destructive to COMs to be a plausible match to observed abundances, with such effects occurring on shorter timescales with increasing CRIR. The white sections in Figs. 2.5 and 2.6 indicate peak MF abundances $< 10^{-8}\, n_{\mathrm{H}}$ or peak methanol abundances $< 10^{-6}\, n_{\mathrm{H}}$. This destructive effect is very strongly associated with the degree of ion-molecule destruction occurring in the gas phase during COM desorption.

2.4.5 Comparisons with NGC 6334I sources

The model grid appears capable of producing broadly appropriate MF:GA and MF:AA ratios for comparison with the observed values on lines of sight toward NGC 6334I.

Here we consider more carefully which models match those sources most closely, with a view to understanding the possible physical basis for the observed bimodal behavior.

Table 2.2 lists the results for each matching procedure (see Section 2.3.3), the observed abundance ratios of MF:GA and MF:AA, and the best-match modeled abundance ratios along with their respective physical conditions. With no constraints on the selection of the best-match models for each of the twelve sources (matching procedure #1), many of the best-match models tend to have hydrogen number density values on the higher end of the tested range (2×10^{10}cm^{-3}), with a mix of results for the other parameters. The ζ values span almost the full three orders of magnitude sampled by the model grid. For most of the best-match models, the MF:GA and MF:AA ratios achieved fall very close to the observed values, within around 10%. For the observational lines of sight that reach the more extreme MF:GA ratios, the best-match models can reach similarly extreme ratios, but they are not such a close match; for example, the best model for source MM2-iii (ID number 12) reaches MF:GA and MF:AA ratios of 577 and 43.1, respectively, while the observations indicate values 374 and 28.3. It is likely that the lesser quality of match in these cases is due to the limited sampling of parameter space. With a finer resolution in the parameters in the high-density, high-ζ, long warm-up timescale regions of the parameter space, better matches with individual models could probably be found.

Matching procedure #2 essentially evaluates the best match for each source based on just the models shown within each individual panel in Figs. 2.5 & 2.6, corresponding to a particular ζ and $A_{v,init}$. Within each panel, the best-match model for each source is marked with a circle and labeled with a source ID number, 1–12, as shown in Table 2.2. Sources 1–9 are the MM1 sources; sources 10–12 are the MM2 sources. The best-match model setups shown in the table for procedure #2 are based on the overall best-matching combination of ζ and $A_{v,init}$.

It is apparent that the best matching models in each panel of Figs. 2.5 & 2.6 tend to lie toward the top-right corner, where the peak abundance of MF:GA ratio is most variable. Additionally, the sources corresponding to the MM2 hot core region (our labels 10,11,12) are consistently grouped together in all panels, and are usually furthest toward the top-right.

The panel in Figs. 2.5 & 2.6 with the best overall match using procedure #2 is the top right panel (G), having CRIR of 1.30×10^{-15} s^{-1} and initial visual extinction of 2. The second best matching panel has CRIR of 1.30×10^{-17} s^{-1} and visual extinction of 3 (panel J). The third (C) and fourth (N) best-match panels have similar setups, with CRIR of 1.30×10^{-17} s^{-1} and 1.30×10^{-15} s^{-1}, and initial visual extinctions of 2 and 3, respectively.

Thus, while the ζ and $A_{v,init}$ can be constrained over the whole list of sources, the top-ranked best-matching *panels* are not adjacent in the parameter space. The best-matching panel (G) has an overall m-value of 1.050; this would be equivalent to both modeled molecular ratios diverging from the observed values by a factor ∼1.64 for all sources. The second best-matching panel has an m-value of 1.125, indicating an average divergence by a factor ∼1.70. This small difference between models whose ζ-values are divergent by a factor 100 would tend to suggest that the CRIR value is not well constrained by MF/GA/AA ratios at the sampling resolution tested in the grid.

There is also a possibility that MM1 and MM2 sources have different physical conditions (matching procedure #3). When executing the matching process separately for MM1 and MM2, the best-match models for MM1 remain the same models as for procedure #2. However, the best match models for MM2 have conditions with a lower cosmic-ray ionization rate of 4.1×10^{-18} s^{-1} (panel B) and a longer warm-up timescale of 2×10^6 years. Each of the MM2 sources are best matched by the same model. Although the best-match CRIR and warm-up timescale are now different, the high density value of 2×10^{10} cm^{-3} and visual extinction of 2 mag are the same as in matching procedure #2 for these three sources. This suggests again that gas density is more determinative than CRIR of the final molecular ratios achieved in each model.

2.5 DISCUSSION

Although the models include a large number of chemical species, understanding how different variations in physical parameters might affect the ratios between the $C_2H_4O_2$ isomers methyl formate, glycolaldehyde and acetic acid, is of primary consideration.

The results of the model grid indicate firstly that the range of observational ratios obtained by El-Abd et al. (2019) can be achieved by the models. Indeed, although we identify the "best-match" model for each of the sources in NGC 6334I, a number of different model setups can reproduce the observed values with a reasonable degree of accuracy. For some of the smaller observed MF:GA and MF:AA ratios, some of the models come very close to the exact values (based on values for matching procedure #1, as seen in Table 2.2). When the observed values become most extreme, mainly for the MM2 sources, which are based on upper limits for the column density of glycolaldehyde, the models are also capable of reaching appropriately extreme ratios, but they are less likely to be an exact match. This is the result of having only a limited parameter resolution in the model grid. The warm-up timescale parameter has four different values per order of magnitude variation; the cosmic-ray ionization rate two; in most cases, the gas density has only order-of-magnitude variation in the tested values; while visual extinction is assigned only two possible values in total.

One might expect that with a more finely spaced (and computationally expensive) parameter grid, the best-match models might sometimes vary from those found here. For example, while the models produce a (near-)perfect match (using matching procedure #1) for our source 1 (NGC 6334I MM1-i) in Table 2.2, the match for source 5 (NGC 6334I MM1-v) is notably less accurate. In the former case, further tuning in the parameters would probably produce only a limited change in the underlying physical parameters. In the latter case, parameter-tuning might produce not only a better match but a substantial change in the underlying parameters due to the degeneracy of the models in reproducing a limited set of observational data.

An example of the potential degeneracy of, in particular, the cosmic-ray ionization rate in producing similar outcomes may be seen for source 11 (NGC 6334I MM2-ii). Matching procedure #1 by definition provides the overall best-match model from our model grid. Since the observed MF:GA ratio for source 11 is based on an upper limit for glycolaldehyde, any modeled ratio greater than the observed value is deemed a perfect match, and in fact the best-match model produces a MF:GA ratio that is almost double the observed minimum value. Using matching procedure #2, which requires all sources to adopt a uniform CRIR, the best-match model still appears to be a fairly acceptable match to observations, while the collective CRIR is nearly three orders of magnitude greater than that obtained using matching procedure #1. When using matching procedure #3, which allows MM2 sources to adopt their own collective CRIR (versus MM1 sources), the original best-match model returns for source 11. Under this scheme, the other two MM2 sources, 10 & 12, are also forced to adopt the same CRIR, but the quality of match is not strongly affected in these cases either.

Of the three main physical parameters varied in the grid, CRIR should probably be viewed with the greatest caution as to the importance of its influence over the model MF:GA and MF:AA ratios. The stage-2 gas density and warm-up timescale, however, appear to be somewhat more robust when imposing the three different matching procedures.

2.5.1 Comparison of Peak Abundance Values

As described in Sec. 2.3.3, the MF:GA ratios are determined based on peak abundance values for each molecule. However, due to their different binding characteristics, there is variation in precise the times and temperature at which MF, GA, and AA peak. In fact, the MF and GA abundances do indeed peak at the same temperature and time in some models , while in others they technically reach their peaks at very different points. The maximum peak-to-peak temperature difference between MF and GA in all our models is 237 K. In this case, MF and GA both reach something very close to their peak values at around the same temperature, but the MF abundance creeps up marginally over time until the end of the model, creating a seemingly large divergence. An example of this effect may be seen in Figure 2.1; GA and MF abundances peak at 242 K and 319 K, respectively, while the actual MF:GA ratio at these two temperatures varies only marginally. A similar effect is seen in Figure 2.3. Figure 2.2 demonstrates a more meaningful difference in peak temperatures of 27 K.

Given the typically large errors on observationally determined excitation temperatures (often tens of K), with which we may associate the peak-abundance temperatures discussed here, the variations between molecules in the models are at least consistent with observations. For the purposes of comparing between MF:GA ratios within the dataset, the models will necessarily display some variation depending on whether the ratio is taken, for example, at the time/temperature of the MF peak, or that of GA. In the interests of simplicity, this variation is not taken into account in the model comparisons. However, it is unclear to what degree this omission is meaningful without using a more physically accurate physical model of the source structure than the present modeling setup can provide. The observed molecular abundances are dependent on the spatial arrangement of the molecules and the local density and temperature structure. Multi-dimensional hydrodynamical and chemical modeling of hot-cores, coupled with direct simulation of emission spectra, may provide the ultimate solution.

2.5.2 Density and timescale thresholds for large MF:GA ratios

We may tie this varying influence of the physical parameters back to the chemical causes of the variation in the MF:GA ratio as discussed in Secs. 2.4.2 & 2.4.3. It was noted that high ζ-values drive an initial split in the solid-phase abundances of MF and GA, which then carries through to the ultimate gas-phase abundances of those molecules; however, this divergence is limited in scale. The much greater divergence needed to reproduce very large gas-phase MF:GA ratios is the outcome of a very selective grain-surface destruction process affecting GA, that occurs during the period of rapid ice desorption. The long residence time of GA once exposed on the grain surface allows it to be attacked and destroyed by atomic H adsorbed from the gas phase. This effect was seen to occur most strongly in models with high gas density and long warm-up timescales, while an elevated CRIR would tend to increase the amount of H present in the gas to some degree. As found by Padovani et al. (2018), the production of atomic H in dense regions is almost exclusively caused by cosmic rays, through interactions with electrons released by the initial H_2-ionization event.

To illustrate this effect more clearly, Fig. 2.7 plots the peak MF:GA ratio produced in the models against the stage-2 gas density, n_{H}, arranged in panels that correspond to the same fixed values of initial visual extinction and CRIR as in Figs. 2.5 & 2.6. Each curve corresponds to a different warm-up timescale, with circles indicating the best-match models for each source under procedure #2. Regardless of the best-match models in each case, what may be clearly seen in most panels and for most warm-

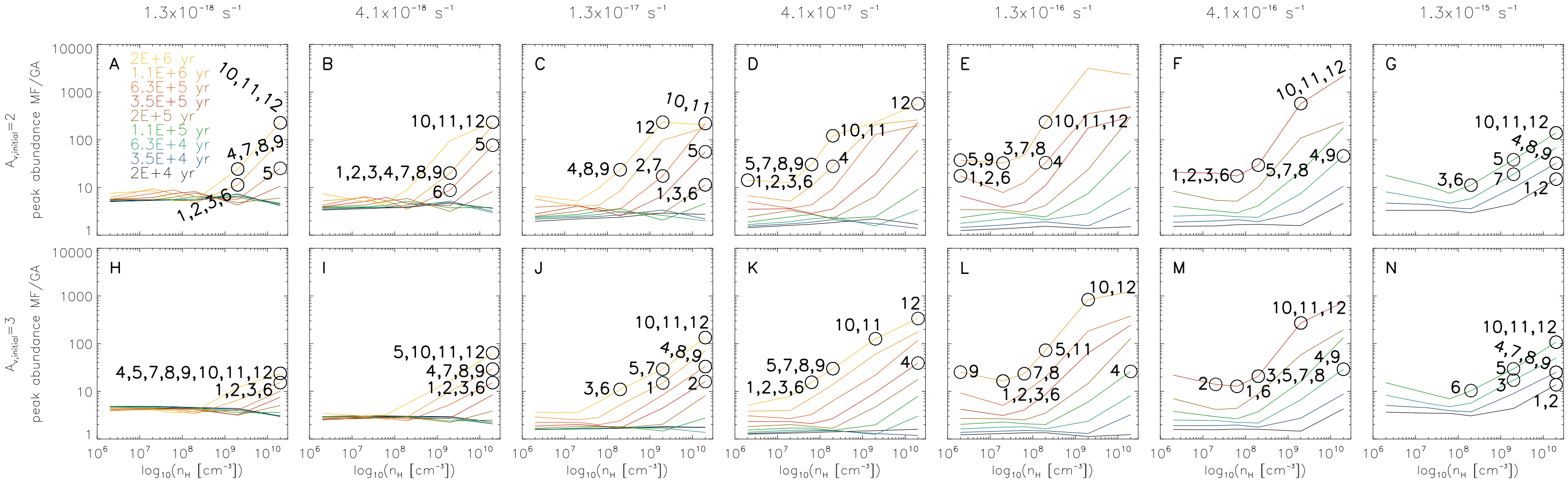

Figure 2.7 Peak MF:GA ratios from the models as a function of stage-2 gas density n_{H}. Each curve corresponds to a different stage-2 warm-up timescales. Best match models from matching procedure #2 for each panel are circled and marked with their respective source, labeled as per Table 2.2. Only data points for models that satisfy the minimum abundance thresholds for methanol and methyl formate are shown.

Table 2.3 The time from when GA becomes available to desorb off the grain surface to when it is finished desorbing ($t_{\mathrm{des,GA}}$) is listed next to its respective warm-up timescale.

t_{warmup} (yr)	$t_{\mathrm{des,GA}}$ (yr)
2.00×10^4	1.15×10^3
3.56×10^4	2.05×10^3
6.32×10^4	3.65×10^3
1.12×10^5	6.49×10^3
2.00×10^5	1.15×10^4
3.56×10^5	2.05×10^4
6.32×10^5	3.65×10^4
1.12×10^6	6.49×10^4
2.00×10^6	1.15×10^5

up timescales is the appearance of a threshold gas density above which the MF:GA ratio grows steadily. This is seen most clearly in the lowest-CRIR panels, in which all warm-up timescales achieve very similar MF:GA ratios when gas densities are low. At higher CRIR-values the longer warm-up timescales tend to achieve somewhat higher MF:GA ratios even at low densities. Nevertheless, in all panels a marked uptick is apparent, typically around densities of $\sim 10^8 - 10^9$ cm^{-3}, where the MF:GA ratios begin to rise substantially above 10. A more accurate threshold for this rise in MF:GA ratio is given by the product of the gas density and warm-up timescale for each model; a value $n_{\mathrm{H}} t_{\mathrm{wu}} \simeq 3 \times 10^{13}$ cm^{-3}yr crudely marks the point at which the upturn begins.

While the precise physical conditions most applicable to an individual source are still difficult to determine with certainty based on a comparison using only two key molecular ratios, and while the model grid is only a simplistic representation of the physical conditions in such a source, the models do indicate that extreme MF:GA ratios are the result of some combination of an extreme gas density during the period of rapid ice desorption, and a relatively long period spent in that temperature regime. Below a threshold value of these combined parameters, the MF:GA ratio is expected to be stable at the commonly observed value of $\sim$10, although the precise value is still somewhat dependent on the full set of physical parameters. Considering the critical timescale threshold for adequate COM abundances (see Sec. 2.4.4) decreases as the CRIR increases (see Figs. 2.5 and 2.6), this in turn leads to a shorter timescale needed at high CRIR to reproduce the observed high MF:GA ratio.

Under what specific conditions might this threshold be exceeded? Although average gas densities toward hot cores are often determined to be on the order of $\sim 10^7$–10^8 cm^{-3} (Jørgensen et al., 2020; Herbst & van Dishoeck, 2009), the presence of a circumstellar disk could plausibly push up the gas densities to rather higher values, such as the maximum adopted in our model grid, of 2×10^{10} cm^{-3}. In this scenario, the emission from MF, GA, AA and presumably the other COMs detected in the hot core would be originating primarily from that disk (or from its surface, as dust optical depth would likely be important).

It is worth considering the influence of the sticking coefficient of atomic H at these higher temperatures. As in G22, these models assume a sticking coefficient of unity for all species, under all conditions. Measurements by He et al. (2016) and calculations by Dupuy et al. (2016) indicate the sticking coefficient of atomic H to be near unity at dust temperatures around 10K, which is appropriate when most of the ice build-up takes place. (Dupuy et al., 2016) also calculated rates at dust temperatures as high as 70 K; with a gas temperature of 150 K, they determined a sticking coefficient of H to an amorphous water-ice surface of $\sim$0.3. In our model, GA destruction by adsorbed atomic H occurs mainly in the temperature range $\sim$125–160 K; a decrease in the H adsorption rate by a factor of $\sim$3 in that regime would have a similar effect as lowering the gas-density by that same factor. The use of a temperature-dependent sticking coefficient in the model would therefore be expected to shift the density threshold to a higher value than the present models suggest, likely by a factor of a few.

In accordance with G22, this work assigns a binding energy of 661K to atomic hydrogen (Senevirathne et al., 2017) rather than the value of 450 K that was used in past models (Garrod & Herbst, 2006). We may consider the effect of this change on the MF:GA ratios; firstly, the greater binding energy produces a lower desorption rate for atomic H. Because desorption is the dominant loss process for surface hydrogen (far beyond any surface reaction) at the high temperatures (>100 K) at which surface GA is being destroyed, this increases the surface lifetime of H atoms, which is equivalent to increasing the average surface population of H. This in turn increases the rate of GA destruction by H by a commensurate factor, as the latter is given more time to find its reaction partner before it desorbs. At 150 K, the higher binding energy would provide a surface lifetime around 4 times higher, and thus 4 times more rapid destruction of surface GA. However, this assumes the same diffusion barrier to be used in either case. If the diffusion barrier were scaled down by the same factor as the binding energy, the effect would be lessened (to a net factor ∼2). Our use of binding-energy and diffusion-barrier values that were calculated in the same study has the advantage of self-consistency between the two values.

Achieving the highest MF:GA ratios is assisted by elevated ζ-values, due to cosmic rays producing the H atoms in the gas phase that attack GA on the ice surfaces during the desorption period. But the warm-up timescales required under high-ζ conditions are still on the higher end of the parameter space tested here. How plausible is a warm-up timescale as long as 2×10^6 yr for a high-mass star-forming source? In fact, such a long timescale is not required to produce the extreme MF:GA ratios. The highly prescribed warm-up profiles used in the present models cover a very wide range of temperatures, not all of which are important to the MF:GA ratio.

At this point it is worth noting more precisely how the nominal warm-up timescale used in the models affects the MF:GA ratio. Due to the nature of the destruction mechanism, the timescale that is important is not the warm-up timescale *per se*, i.e. the period taken to go from 8 K to 200 K; instead, the important timescale is the time taken between the onset of water-ice desorption (when GA trapped in the ice first becomes exposed on the ice surface) and the moment when most GA has left the grains and can therefore no longer be attacked on the grains. This corresponds broadly to a temperature range of ∼125–160 K, although this varies somewhat between different models.

Hence, all of the time required to approach the point of onset of water-ice desorption, i.e. the time to go from 8–125 K, should be of little influence to the MF:GA ratio if the MF and GA behavior depends principally on the proposed high-temperature surface-destruction mechanism for GA. Therefore the preference for longer warm-up timescale models in matching the more extreme MF:GA ratios is a constraint on a relatively short window in time, rather than a constraint on the full timescale for hot-core evolution.

Table 2.3 indicates the time-period taken to pass through the ∼125–160 K desorption regime for each of the model warm-up timescales. This desorption timescale is shorter by a factor of ∼17 compared with the corresponding full warm-up timescale; all are $\lesssim 10^5$ yr. The combination of a gas density even higher than the maximum of 2×10^{10} cm^{-3} used here, representing gas in a circumstellar disk, combined with an intermediate timescale for desorption on the order of 10^4 yr would seem achievable even for rapidly evolving hot-core sources. The attainment of a high MF:GA ratio in such an environment might then be the result of an exceptionally high-density or long-lived circumstellar disk, especially a disk that remained at a temperature of between 125–160 K for a long period.

The timescales to go from 125–160 K may be compared with those determined in the chemical/dynamical models of Barger et al. (2021); those authors presented

Table 2.4 Original and reduced activation-energy barrier values for grain-surface/ice reactions of atomic H with glycolaldehyde. Barriers in the test models are reduced by 25%.

Reaction	Original (K)	Reduced (K)
$H + CH_2OHCHO \rightarrow H_2 + OH_2CCHO$	992	744
$H + CH_2OHCHO \rightarrow H_2 + CHOHCHO$	1530	1150
$H + CH_2OHCHO \rightarrow H_2 + CH_2OHCO$	374	281
$H + CH_2OHCHO \rightarrow CH_2OHCH_2O$	1100	825
$H + CH_2OHCHO \rightarrow CH_2OHCHOH$	2520	1890

1-D radiation hydrodynamical (RHD) models for hot cores of several different mass-accretion rates. Chemical models (without nondiffusive dust-grain processes) were then run in post-processing for trajectories traced by Lagrangian particles. Many of these particles remained in the 125–160 K regime for around 1500 yr, although the temperature was not always a monotonically increasing value (see below). Those 1-D models therefore provide a foundation for the timescales shown in Table 2.3. Higher-dimensionality RHD models might allow more sustained periods in the appropriate temperature regime with high gas density.

It is worth noting finally that the models involve a monotonically rising temperature with time. The model timescales taken to go from the onset of water-ice desorption to the end of GA desorption are tied to that gradual ramp-up behavior. A model that topped out at a temperature within the 125–160 K range should still ultimately lose all of its water and GA ice (as well as MF and AA) to the gas phase, but the timescale required for complete desorption of the ices would depend on the final value of that temperature. Identifying a very specific timescale or density required to produce a high MF:GA ratio would be best achieved using a more physically and dynamically exact model of hot-core evolution, such as one that includes circumstellar disk evolution.

2.5.3 Activation-Energy Barrier Testing

Having identified a very specific chemical behavior as the cause of the observed extreme MF:GA ratios, it is valuable to test the sensitivity of the model outcomes to the activation-energy barrier adopted for the critical destruction reactions between diffusive atomic H and glycolaldehyde on the grain surfaces. In particular, we have sought to test the effect on the threshold densities beyond which the surface GA mechanism begins to take hold.

In a set of test models, the activation-energy barriers of the grain-surface/ice reactions of atomic H with glycolaldehyde were reduced by 25%, as shown in Table 2.4. This value was chosen to correspond to the approximate degree of variation in activation energy barriers for these reactions calculated by Álvarez Barcia et al. (2018) when adopting different functionals (see their table A.2).

Three timescales were chosen to evaluate the effect of the lowered reaction barrier, using a setup that adopts the standard ζ-value and an initial A_V of 2. The first timescale chosen (2×10^5 yr) is that in which the uptick in MF:GA first begins to manifest strongly in Fig. 2.7.

Fig. 2.8 contrasts the peak MF:GA ratios obtained in the regular models (solid lines) with the new runs (dashed). The lowered reaction barrier data is shifted up slightly in its peak MF:GA ratio. By lowering the barriers for reactions that form GA, those reactions are able to proceed easier and therefore more GA is made in the models. This alteration of the GA reaction barriers has a modest and fairly uniform effect on the models tested, especially at densities greater than the threshold value. However, the threshold density itself is essentially unaffected by the change. We therefore expect that uncertainties in the precise activation-energy barrier value may have a moderate influence on model outcomes, but not on the qualitative result nor on the quantitative determination of the density threshold value.

2.5.4 Cosmic-Ray Ionization Rates

While the cosmic-ray ionization rate is meant to represent a generic galactic value, it is commonly assumed in chemical modeling studies that the rate is constant in a local region. However, there is evidence (Gaches & Offner, 2018) that the protostar itself can contribute to the cosmic-ray ionization rate especially in denser regions. MM1 would seem to have much more potential for internally accelerated cosmic rays as it is driving a non-thermal jet component (Brogan et al., 2018) and this could be evidence of cosmic-ray acceleration (see for example Padovani, Marco et al. (2021)). In constrast, MM2 shows only thermal radio emission consistent with a hypercompact HII region.

The MM1 sources in NGC 6334I have lower MF:GA abundance ratios than MM2, while our matching procedure #3 indicates that MM1 sources should collectively be best matched by a much higher CRIR than MM2; a value of 1.30×10^{-15} versus 4.11×10^{-18} s^{-1}.

At the end of stage 1 (collapse), the difference in chemical abundances of our key species, MF, GA, and AA, in our models is mainly affected by the CRIR value. When comparing Figures 2.1, 2.2, and 2.3, the starting abundances of these species is higher in conditions with high CRIR, due to the greater abundance of radicals on grain surfaces and in the ices, as described in Section 2.4. Although the CRIR does have an effect on the inheritance of MF, GA, and AA from stage 1 to stage 2, the main influence on high MF/GA ratios appears later on in stage 2, when GA is destroyed on the grain surface as described in 2.4.3.

Given the relatively small effect that the CRIR has (versus that of the gas density and warm-up timescale) on the MF:GA and MF:AA ratios in the models, the apparent

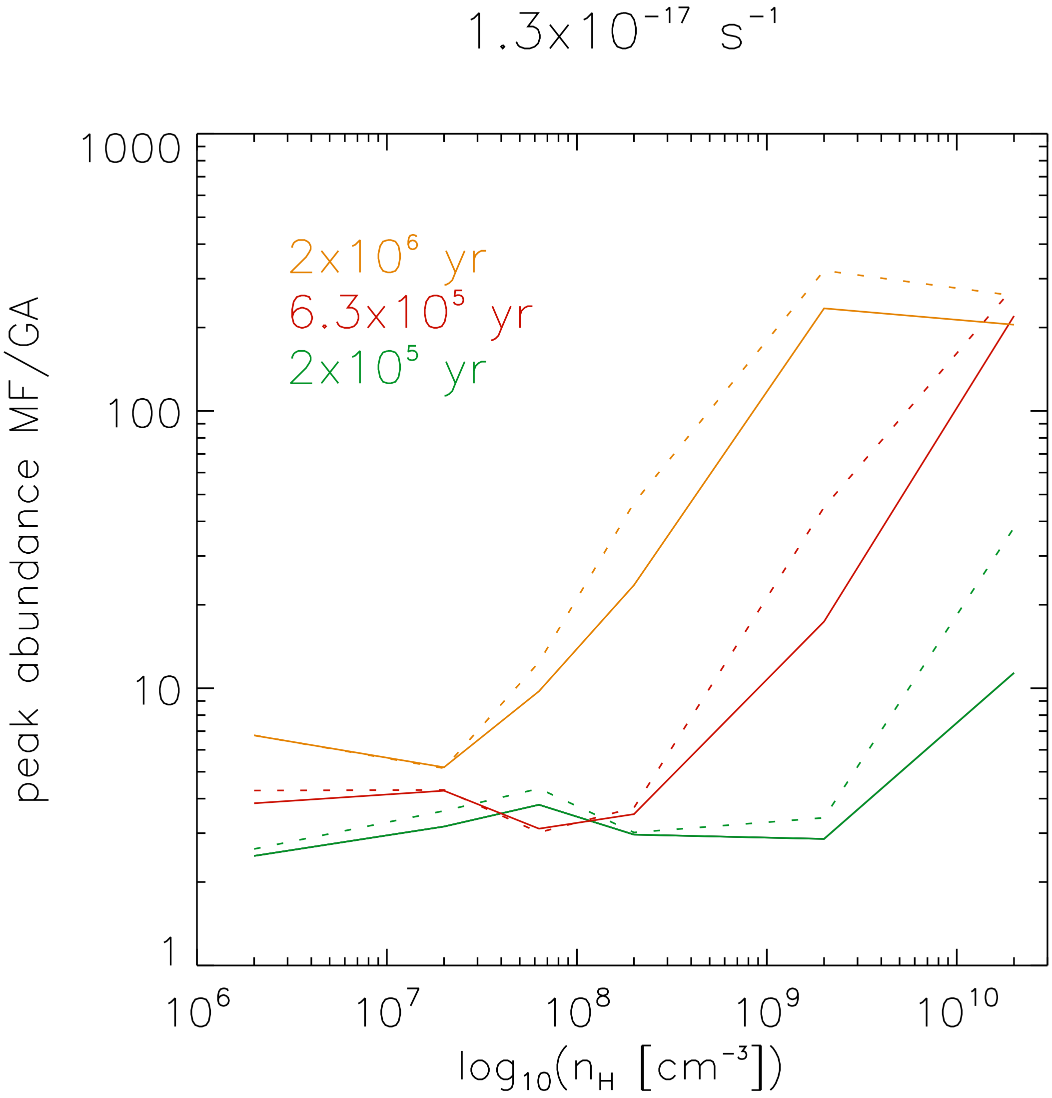

Figure 2.8 A test on the effect of a lowered reaction barrier on GA formation reactions on the peak abundances of MF:GA. Original reaction barrier models are shown as solid lines and barriers reduced by 25% are shown as dashed lines.

variations between MM1 and MM2 may be not ultimately be very meaningful. The large range of ζ-values provided by the unrestricted matching procedure #1, which notably produces a wide range of values even within the MM1 and MM2 sources, appears to indicate that ζ is not well constrained.

It is also noteworthy that, in spite of the MM2 sources having the greatest MF:GA ratios (i.e. only upper limits for the observed GA column densities), these sources are best matched by models with very low CRIR values, which would tend to *decrease* the MF:GA ratio in each model. It seems most likely, therefore, that the overall smaller effect of CRIR on the MF:GA ratio is acting to fine-tune the match parameter to produce the best possible match to the observed ratios while not being the main influence on it. Thus, as already noted, the use of a model grid with greater resolution in all of the main physical parameters may be required to tune the CRIR rate in a more meaningful way.

Ultimately, the smaller influence of CRIR on the MF:GA and MF:AA ratios means that these ratios are not sufficient to determine the most likely CRIR for each source. With this particular goal in mind, a larger range of molecules would be necessary for the comparison, such as we have for the comparison of the models with IRAS 16293B and Sgr B2(N2) molecular abundances (see Appendix A.1).

2.5.5 Influence of luminosity outbursts

NGC 6334I is one of few (high-mass) star-forming regions found to have exhibited an outburst event; Hunter et al. (2017) observed an outburst at mm wavelengths originating in NGC6334 I-MM1 corresponding to a four-fold increase in the millimeter continuum flux density and an estimated 70-fold increase in luminosity near the peak of the event. Hunter et al. (2021) further observed the outburst at mid-IR wavelengths four years into the event, confirming a luminosity increase at a factor of 16.3±4.4, and noting that the outburst had persisted for at least 6 yr. Hunter et al. (2017) noted also that sources MM2–MM4 appear not to have altered in luminosity.

It is interesting to consider the possible influence of an accretion outburst on the scheme described above to explain extreme MF:GA ratios. A luminosity outburst would produce an increase in dust temperature that could either lead to rapid desorption of ice mantles, or indeed, depending on radial distance from the protostar, could elevate colder grains to a temperature conducive to GA destruction. We note that the observational study of the HMYSO G24.33 by Hirota et al. (2022) shows evidence of changes in thermal line emission due to an accretion event (although in this case it is one of the smaller, periodic events rather than a stronger, stochastic event). In the case of the loss of ice mantles, subsequent cooling of the grains could also lead to the re-adsorption of gas-phase molecules onto the grains. It is therefore difficult to make predictions as the likely effects on the chemical models without an explicit multi-dimensional physical treatments that includes recurring outburst events. Although variable protostellar UV emission is also to be expected, the influence on the large-scale chemistry may be more muted due to local absorption close to the protostar.

We note that, while MM1 has experienced an outburst, extreme MF:GA ratios are thus far detected only toward MM2, which appears stable in its luminosity on recent timescales. Any immediate influence on the abundances of COMs in MM1 might be expected to have shown up in the data of El-Abd et al. (2019). However, according to the simulations of Meyer et al. (2021), such outburst events are a common feature of high-mass star formation, accounting for 40–60% of mass accreted, over multiple events. Those models indicate that individual outbursts may last a few years up to some tens of years, while the integrated burst duration time over the star's lifetime could last up to some hundreds of years. In that case, the monotonically increasing temperature profiles used in the present chemical models may not be accurate. However, the overall time spent in the key temperature range for grain-surface GA destruction may still be valid, especially if the re-accretion of desorbed molecules onto cooling grains can occur.

2.6 Conclusions

We have presented a large parameter grid using the astrochemical model MAGICKAL to investigate the physical conditions that lead to a high methyl formate (MF) to glycolaldehyde (GA) gas-phase abundance ratio in the MM2 hot-core cluster in NGC 6334I observed by El-Abd et al. (2019). The present study uses essentially the same model setup as Garrod et al. (2022) for simulating hot-core chemistry, but with a much larger parameter space tested, focusing mainly on the cosmic-ray ionization rate, final gas density, and warm-up timescale. The effect of varying the initial visual extinction used in the collapse stage of the models was also tested in a limited way. In these models, it was already found that most of the MF and GA, along with many other oxygen- and nitrogen-bearing COMs, were formed on the dust grains, often during the early, cold, collapse stage. Those COMs would be retained in the icy mantles of the dust grains until much higher temperatures were achieved due to the onset of star formation, leading to the desorption of the mantles into the gas phase.

We identify the destruction of GA on dust grains as the most influential cause of the divergence in gas-phase MF:GA ratios between different sources. The mechanism occurs when water-ice desorption becomes rapid at temperatures greater than $\sim$125 K, leading to GA and other COMs in the bulk ice being exposed on the surface of the ice before they desorb into the gas phase. Under the high gas densities present in the hot core, H atoms from the gas phase can adsorb briefly onto the ice surface, where they may react with and destroy molecules on the surface. Methyl formate, the structural isomer of GA, may be attacked by atomic H; however, because it has a relatively low binding energy to a water-ice surface (lower than that of water itself), it actually leaves the surface almost immediately once it is exposed by the loss of the water molecules that would otherwise trap it in the bulk ice. This means that surface reactions of MF with atomic H are rare. Glycolaldehyde, on the other hand, has a high binding energy and remains on the ice surface for a longer period of time before desorbing. Hence, during this period, there are more chances for it to be attacked and destroyed by atomic H coming from the gas. Although acetic acid (AA) also has a large binding energy, leaving it exposed on the surface for a long period, the absence of an aldehyde group (-CHO) on this molecule makes it less liable to attack by atomic H, so the MF:AA ratio is unaffected.

The influence of this mechanism is strongly dependent on the period of time over which the GA molecules are exposed on the icy grain surface prior to desorption, as well as on the number density of atomic H in the gas that may adsorb and attack it. Below a threshold value of the product of gas density and exposure timescale, this chemical attack does not strongly affect the abundance of GA on the grains, meaning that its ultimate gas-phase abundance is also unaffected. Under these conditions the models retain fairly regular MF:GA ratios over a range of physical conditions. Above the density–timescale threshold, GA destruction becomes stronger and stronger, leading to increasingly extreme MF:GA ratios.

We therefore propose that the existence of certain, selected sources with extreme MF:GA ratios, i.e. extremely low GA abundances, may be the result of the emission from those molecules (and other complex organic molecules, COMs) emanating from a region with (i) an unusually high gas density and/or (ii) an extended period in the critical temperature regime of ∼125–160 K at which GA can be attacked while exposed on the icy grain surfaces. This might indicate that the COM emission in those extreme sources is especially dominated by molecules in a circumstellar disk, where those higher densities might be achieved. For sources with more typical MF:GA ratios, emission may be coming from some more extended hot region of lower gas density. A more dynamically exact physical model of hot core evolution to accompany the chemical models would be necessary to explore this idea.

Another important mechanism that produces a divergence in MF and GA abundances occurs in the ice mantles, and becomes influential when cosmic-ray ionization rates are high. The greater dissociation of molecules such as water in the ice mantles, caused by the secondary UV field induced by CRs, leads to a higher production of atomic H in the ice. Above around 17 K, this H becomes highly mobile in the ices, leading to: (i) recombination with large radicals formed earlier in the model, to produce stable molecules including MF; and, (ii) reaction with GA to produce the related ethylene glycol and glyoxal molecules. Although this effect is notable, it does not appear sufficient on its own to reproduce the observed extreme MF:GA ratios.

The cosmic-ray ionization rate also influences the abundance of atomic H in the gas-phase, which can act to increase the efficiency of GA destruction on the ice surfaces. However, it appears to have a weaker influence on MF:GA ratio than the gas density or warm-up timescale used in the model grid. In models with the most extreme cosmic-ray ionization rates, gas-phase ion-molecule reactions lead to low COM abundances, so that – regardless of the MF:GA – the absolute abundances of these molecules are simply too low to be applicable to hot core observations. Models with the highest CRIR values in the parameter space do require a shorter warm-up timescale to reproduce observed MF:GA ratios. Otherwise, long timescales at high CRIR will lead to absolute COM abundances that are too low.

Using a selection of matching parameters to compare the model data with observed molecular ratios for hot core sources in NGC 6334I, the gas density and warm-up timescale used in the models seem to be the most consistently determined parameters; however, the CRIR is not very well constrained. A grid of models with higher resolution in the key physical parameters might improve this situation, but it is more likely that there is simply not enough observational data in the comparison with two observational ratios to allow other than the most powerful influences on MF and GA abundances to be constrained. As a result, we advise some caution in using the best-match chemical models as an explicit guide to the local conditions present in the NGC 6334I sources with which we have done our most extensive comparisons. The MM2 sources appear to be best represented by higher densities in the hot-core emission regions, with a more sustained period of ice desorption rather than a rapid heating period to eject COMs from the grains. These conditions might be complemented by somewhat elevated CRIR values, but this cannot be determined with certainty.

We summarize the main conclusions of this modeling study below:

(i) The chemical models are capable of reproducing the full range of MF:GA and MF:AA ratios observed.

(ii) A combination of higher gas density and longer timescales for ice desorption appears to be the physical cause of the unusually high MF:GA ratios in the NGC 6334I MM2 sources.

(iii) Such conditions might be indicative of COM emission emanating mainly from a dense and perhaps long-lived disk.

(iv) The main chemical mechanism driving GA destruction occurs on the icy surfaces of dust grains, when atomic H adsorbed from the gas phase attacks GA before it has time to desorb.

(v) High gas densities allow destructive atomic H to adsorb and attack GA more readily.

(vi) A long period of time spent in the temperature range of ~125–160 K (i.e. between the times when water begins to desorb and when GA has left the grains entirely) leads to more GA destruction by atomic H.

(vii) The different binding energies of MF and GA on water ice are crucial to the selectivity of the surface destruction mechanism; individual MF molecules escape the surface as soon as they are exposed by water loss, while GA lingers and can be substantially destroyed by H, given the right conditions.

(viii) Below a threshold combination of gas density and warm-up timescale, modeled MF and GA ratios are stable and in keeping with more typical observational values.

(ix) Acetic acid on the ice surface is not affected by the presence or absence of atomic H adsorbed from the gas, in spite of its high binding energy, due to the higher barriers to reaction with atomic H.

(x) An increased cosmic-ray ionization rate results in greater production of most COMs in the ice, although extreme values also act to destroy gas-phase COMs very rapidly. A higher CRIR also produces modest enhancement in the MF:GA ratio, but not sufficient to explain the observed extreme MF:GA ratios.

(xi) Varying the initial visual extinction produces no significant changes in the MF:GA ratio.

2.7 Chapter Acknowledgements

This work was funded by the National Science Foundation, through grants AST 1906489 and AST 2206516. This paper makes use of the following ALMA data: ADS/JAO.ALMA#2012.1.00712.S, ADS/JAO.ALMA#2013.1.00278.S, ADS/JAO.ALMA#2011.0.00017.S, and ADS/JAO.ALMA#2012.1.00012.S. ALMA is a partnership of ESO (representing its member states), NSF (USA) and NINS

(Japan), together with NRC (Canada), NSTC and ASIAA (Taiwan), and KASI (Republic of Korea), in cooperation with the Republic of Chile. The Joint ALMA Observatory is operated by ESO, AUI/NRAO and NAOJ. The National Radio Astronomy Observatory is a facility of the National Science Foundation operated under cooperative agreement by Associated Universities, Inc. We also thank Mélisse Bonfand for helpful discussions.

CHAPTER 3

COUPLED CHEMICAL AND RADIATION HYDRODYNAMICAL MODELING OF HOT CORINOS: FORMATION AND PROCESSING OF ICES

"Without a nickel to my name. Hopped a bus, here I came. Could be brave or just insane. We'll have to see"

La La Land, *Another Day of Sun*

3.1 Abstract

The work presented here is in preparation to submit to The Astrophysical Journal, with myself as the corresponding author. Radiation hydrodynamical modeling was completed by others in the UVA astronomy department, Yisheng Tu, Andy Lam, and Prof. Zhi-Yun Li. This work will follow the submission of the hot core paper by Dr. Mélisse Bondfand.

We present a coupled multidimensional radiation hydrodynamic and chemical model of a hot corino, using the hydrodynamical code *ATHENA++* and the three-phase chemical kinetics code *MAGICKAL*. Our models trace the evolution of ice chemistry from the pre-stellar collapse through disk formation, capturing the spatial distribution of simple species and COMs through these stages. With the recent James Webb Space Telescope launch, here we focus on modeling hot corino ices. We compare our calculated column densities with JWST and Spitzer data for all three YSO stages (Classes -I, 0, and I). We examine the effect of viewing angle on column density and find that the most variation occurs for inclinations between 60 and 90 degrees (edge-on). Our current chemical model underproduces carbon-bearing ice species, indicating that there may be a higher abundance of carbon-bearing molecules on the grains than we currently simulate. The model also reveals the effect of meridonial circulation in the disk structure and the movement of material - some of which experiences hot core-like behavior leading to low abundances of some species on the grain surface. We find pathways for trajectories that are able to survive the harsh environment of the protostar, giving insight to the potential species preservation that might be incorporated into comets. These results have direct implications for understanding the molecular origins of the early solar system and interpreting future observational studies of protostellar chemistry.

3.2 Introduction

Recent findings indicate that many complex – and potentially pre-biotic – molecules present in the young solar system may have their origins in the very earliest stages of star formation (Drozdovskaya et al., 2019). Observations of low-mass star-forming cores called "hot corinos" may therefore provide us with insight into the chemical conditions that were present when the young Sun was forming, prior to the formation of the protoplanetary disk (the Class II Young Stellar Object or YSO stage) that eventually yielded planets and comets. Hot corinos, associated with YSOs of Class 0–I, are particularly noteworthy due to the great diversity and complexity of gas-phase organic molecules that are detected there, through microwave molecular emission spectroscopy using instruments such as the Atacama Large Millimeter Array (ALMA). The largest complex organic molecules (COMs) detected in hot corinos include species such as methanol (CH_3OH) and glycolaldehyde ($HCOCH_2OH$) (Jørgensen et al., 2012); the most complex species detected in hot, star-forming sources are usually detected in hot cores, the high-mass equivalents of hot corinos, and include propanol (C_3H_7OH) (Belloche et al., 2022; Jiménez-Serra et al., 2022) and urea (NH_2CONH_2) (Belloche et al., 2019).

The origins of many COMs are understood to involve chemistry occurring on dust grain-surfaces when the core is still relatively cold ($\sim$10 K), producing ices that later desorb during the "hot" stage ($T \gtrsim 100$ K), when the protostar warms the surrounding dust and gas (Herbst & van Dishoeck, 2009). ALMA has provided much evidence concerning COMs in the hot regions (Jørgensen et al., 2020), and now data coming from James Webb Space Telescope (JWST) projects such as CORINOS (Yang et al., 2022), the Early Science Project IceAge (McClure et al., 2023; Rocha et al., 2025), and JOYS+ (Rocha et al., 2024) are providing further information about the presence and spatial distribution of solid-phase COMs in solar-type systems.

Much evidence now points to many COMs being present in the very first stages of star formation, during the pre-stellar stage before a protostar is even formed (Megías et al., 2022; Bacmann et al., 2012; Marcelino et al., 2007; Öberg et al., 2010; Jiménez-Serra et al., 2016), when dust and gas temperatures are $\lesssim$10 K. Laboratory experimental data indicate that COM production at such temperatures can be efficient on ice surfaces in tandem with the chemical production of simpler, more abundant ice species such as formaldehyde and methanol, through the repetitive hydrogenation of CO (Fedoseev et al., 2015, 2017; Chuang et al., 2015). Chemical kinetics models similarly show efficient low-temperature COM production, with non-diffusive chemistry playing the key role in reproducing the observed abundances of molecules in star-forming regions (Jin & Garrod, 2020; Garrod et al., 2022; Ioppolo et al., 2020). However, further chemistry – both on grains and in the gas phase – is expected to occur after the protostar has formed within its surrounding envelope (Class 0) and as the envelope accretes substantially onto the protostar and nascent disk (Class I).

While the collapse of the core and the evolution of the protostar will naturally impart a time-dependence to the chemistry of a hot corino, the spatial distribution of molecules at any particular moment must also be a function of the spatial variation in physical conditions such as density, temperature and radiation fields, as well as the chemical history of any parcel of gas and dust up to that time, throughout the pre-stellar and protostellar stages. For example, as parts of the protostellar envelope and disk reach high temperatures ($>$100K), grain-surface species nearest to the protostar will desorb into the gas-phase and ultimately be destroyed, while molecules on the dust grains in the cold outer envelope should survive by avoiding the protostar's harsh environment (Drozdovskaya et al., 2019). The latter would thus constitute the inheritance of complex molecules passed on to comets.

The viewing angle of a source is also expected to have an effect on the observed column densities. There has been discussion as to whether the viewing angle of the observer to the disk (edge on, face-on, or somewhere in between) would affect whether a source is observed to be COM-rich or COM-poor (Nazari et al., 2022). When viewed edge-on, the mm-wavelength emission used to determine the column density of a molecule must comprise contributions from material under a range of conditions radially through the disk and envelope. However, the dust itself may make a substantial contribution to the opacity, leading to the obscuration of the molecular emission. When looking at a source face-on, the observations are looking through the center of the disk, and might be affected by the outflow, as well as potentially being affected by dust opacity, especially at sub-mm wavelengths. The observed column densities of some species may be more affected by viewing angles than others, depending on their distribution within the source.

To determine from a modeling perspective the nature, distribution and origins of COMs and their emission in hot corinos, it is necessary to have: (i) astrochemical models that are capable of simulating COM chemical kinetics both on the dust grains and in the gas; (ii) realistic physical/dynamical models to combine with the chemical models, so that the motions of gas and dust, beginning in the pre-stellar stage and culminating in the formation of a disk, can be properly coupled to the chemical evolution; and (iii) the ability to simulate the coupled molecular and dust radiative transfer that leads to molecular line spectra that can be converted into estimates of column density as they would be measured in real observations. Only then can a full spatial picture of COM chemistry be built up.

A number of combined chemical and dynamical simulations have been carried out over the past few years, although relatively few have included a substantial gas-grain chemical network capable of modeling COM chemistry. The 1-D models of Aikawa et al. (2008, 2012) using the radiation hydrodynamics (RHD) models of the formation of the first hydrostatic core (FHSC) by Masunaga et al. (1998) and of the second collapse by Masunaga & Inutsuka (2000), traced the infall of multiple parcels of gas beginning in the prestellar core phase. Adopting the grain-surface radical-chemistry scheme of Garrod & Herbst (2006), they found that COMs could be formed at intermediate temperatures, with gas-phase spatial extents determined by their desorption temperatures. Carbon-chain molecules were formed both on the grains and in the gas phase. Although those authors also approximated disk-like conditions by holding the final dynamical state steady for a period, such 1-D treatments naturally cannot simulate an actual circumstellar disk. More recently, Jin et al. (2022) combined the MAGICKAL chemical model (Garrod, 2013; Garrod et al., 2022) with 1-D simulations of the evolution of the envelope around Class 0 protostar Cha-MMS1. They simulated in particular the ice abundances of COMs toward this source. They found that many solid-phase COMs should have potentially detectable abundances during the Class 0 stage, with ethanol being the most abundant of these.

Models by Visser et al. (2009, 2011) used a 2-D semi-analytical approach to model circumstellar disk formation, using the radiative transfer model RADMC to calculate the temperature and UV field. These models concentrated on simple species like water, focusing only on the final state of the disk, rather than the larger envelope. Visser et al. (2015) considered the chemical effects of episodic accretion bursts, by adjusting the luminosity of a protostar in a spherical protostellar model; they found long-lasting variations in CO and H_2O spatial distributions in the envelope.

Multi-dimensional treatments have been used to simulate solar-mass protostellar collapse, often terminating at the first hydrostatic core (FHSC) stage before disk formation (e.g. Furuya et al. (2012); Commerçon et al. (2012); Hincelin et al. (2016). The recent chemo-dynamical simulations of Coutens et al. (2020) considered the formation of a rotationally supported disk, but the evolution ends essentially at the FHSC. They showed that the protostellar collapse stage is the most important period for many COMs to form, based on purely diffusive grain-surface chemistry.

Models by Jensen et al. (2021) used a 3-D MHD model to simulate the collapse of a molecular cloud to form protostars, to study water deuteration. They used RADMC-3D to post-process the radiation fields. However, these models did not produce disks, and did not consider detailed COM chemistry.

Here we present calculations using advanced chemo-dynamical models that include explicit RHD treatments of the Class 0 – I stages, and a semi-empirical treatment for the formation of the preceding prestellar core. A detailed chemical treatment of both gas-phase and grain-surface ice and COM production is coupled with the outputs of the dynamical models. This approach will be necessary to properly interpret current and future JWST and ALMA observations and to test hypotheses on the origins of COMs in hot corinos.

We use the astrochemical model MAGICKAL (Model for Astrophysical Gas and Ice Chemical Kinetics and Layering), which is a three-phase chemical kinetics model (gas, grain-surface, and mantle-ice chemistry (Garrod, 2013)). This model has many capabilities including the ability to trace ice and gas abundances of Young Stellar Objects (YSOs) from Class 0 through I. The model has perhaps the most advanced network for COMs, and is unique in having a full, self-consistent framework for the treatment of both diffusive and non-diffusive grain-surface and bulk-ice chemical reactions, using the framework set up by Jin & Garrod (2020) and Garrod et al. (2022). Coupled with a multidimensional hydrodynamics model that provides time-dependent gas-density and dust-temperature distributions under solar-type conditions, it creates a self-consistent chemical and physical picture of COM chemistry during the early stages of Solar System formation.

The present paper focuses on the ice column densities over time and their distribution throughout the disk as time evolves. A follow-up paper will focus on the analysis of the simulated gas-phase molecular data. Both ice and gas data will be compared to ALMA and JWST observations.

For this paper, the models are compared with existing JWST ice data and other sources found in literature. These include JWST observations by McClure et al. (2023), Rocha et al. (2024), and Rocha et al. (2025) as well as the reported observational values in Boogert et al. (2015). Details of those works can be found in Section 3.4.4.

3.3 Methods

Two main computational codes are used to carry out the simulations: *ATHENA++* for the radiation hydrodynamics (RHD) and *MAGICKAL* for the chemistry, with the latter run in post-processing, based on physical conditions determined from Lagrangian tracer particles. In this main section we present an overview of the basic modeling approach. More specific descriptions of the RHD treatment and the placement of tracer particles are presented in Secs. 3.3.1 and 3.3.2, respectively. The chemical model is described in Sec. 3.3.3. Greater detail on the entire modeling framework can be found in (Bonfand et al. (in prep.)).

The 2D axisymmetric RHD model simulates the evolving density, temperature, and velocity structure of the gas leading to the formation of a YSO, beginning from a singular isothermal sphere with power-law density distribution ($\rho \propto r^{-2}$) representing a prestellar core, and ending with a structure representing a protostar, circumstellar disk, and envelope. A semi-empirical model is used (see Lam, 2022, and Bonfand et al. 2025) to determine the physical/dynamical evolution of the object prior to the initial conditions of the RHD simulation, beginning from a uniform, cold, spherical cloud and ending with the power-law density distribution. In this treatment, the initial cloud is treated as a set of spherical shells, with each initially moving at nearly constant velocity; toward the end of this condensation stage, the velocity gradually decreases to smoothly match the initial conditions of the accretion phase.

Lagrangian tracer particles calculated in post-processing are used consistently across the two stages of dynamical evolution, so that the chemistry can be systematically simulated throughout. The time-dependent gas density, temperature, and radial visual extinction values for each tracer are fed to the chemical model. The chemical simulations for each tracer are then run independently from each other, in two stages corresponding to the initial condensation from a uniform cloud (which we label stage 1) and the RHD simulation (stage 2).

This coupled dynamical/chemical treatment is essentially the same as that employed by Bonfand et al. (in prep.), but using a lower total mass in the simulations, and with a more complex system of assigning tracer particles (see Sec. 3.3.2).

Stage 1 of the model is identified with the formation of a prestellar core, sometimes referred to as Class -I. Stage 2 of the model is identified with the evolution of the prestellar core into a Class 0 source, and then into Class I. In the analysis of our model, we designate the moment when the protostellar mass first exceeds half of the total mass in the simulation ($M_{\rm tot} \simeq 1\ M_\odot$) as being the threshold between the Class 0 and I stages. The RHD model is stopped when the disk reaches a radius of ~300 AU, which is achieved at time $220,000$ yr.

In stage 1, the gas density of the cloud is initially set at a uniform $n_{\rm H} = 2000$ cm^{-3}, evolving to the power-law profile in 1 Myr. The final gas densities range approximately from $10^4 - 10^{10}$ cm^{-3} from edge to center at the end of stage 1; the final central density is 6.45×10^{10} cm^{-3}. Because a semi-empirical treatment is used for the stage-1 evolution, no explicit hydrodynamical calculation is required, and instead the positions

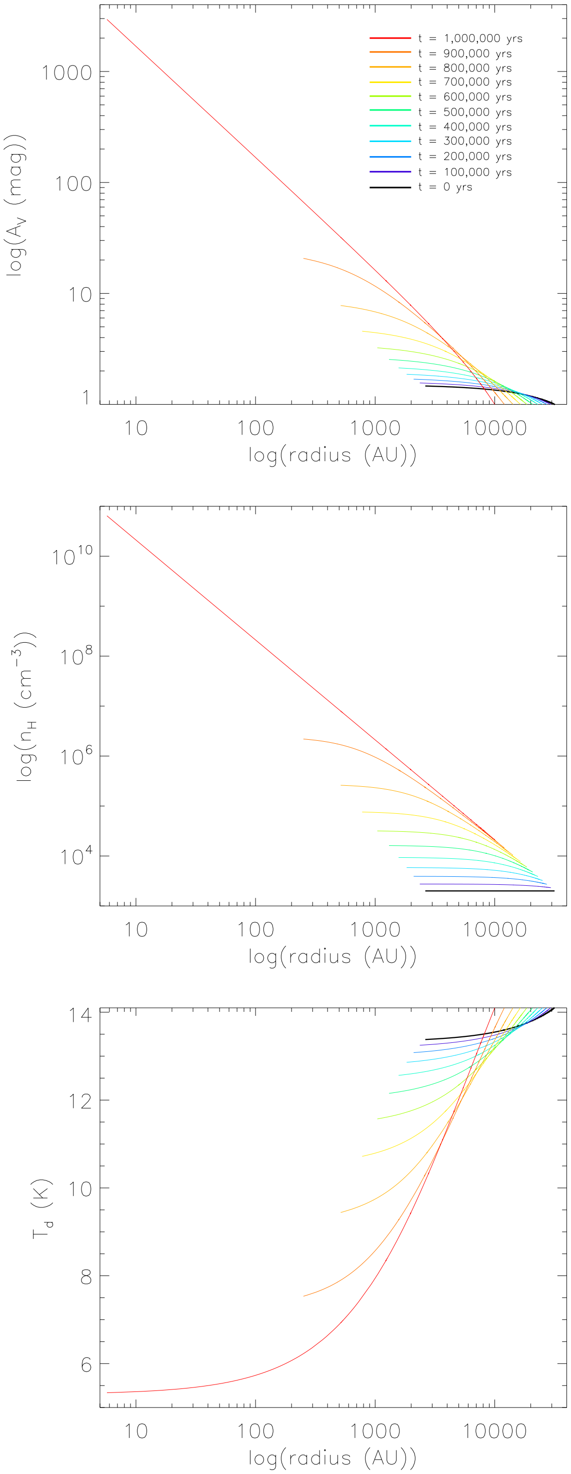

Figure 3.1 Stage 1 (Class -I) physical conditions with respect to the radial distance of the collapsing cloud. Each color represents a different time within the model. Selected times are 100, 000 years apart. **Top:** Visual extinction. **Middle:** Density. **Bottom:** Dust temperature.

and physical characteristics of each tracer particle are calculated individually.

The behavior of the visual extinction, density, and dust temperature with respect to radius during the stage 1 collapse is shown in Figure 3.1. Physical data are plotted for every 100,000 years as represented by the various colors labeled in the legend. The density of each particle increases monotonically during stage 1. The outer radius of the cloud starts at 3.16×10^4 AU and contracts to 10^4 AU.

The visual extinction for each tracer particle during stage 1 is calculated based on the total hydrogen column density integrated radially outward of the present particle position, using the relation $A_\mathrm{V} = N_\mathrm{H} \times 3.1/(5.8 \times 10^{21})$ (Bohlin et al., 1978). A background visual extinction of 1 mag is added to this value to represent external material not explicitly considered in the simulations. Stage 1 begins with a central visual extinction of 1.46 mag and reaches a final value of $\sim$3000 mag.

The gas temperature is fixed at 10 K throughout stage 1 while the dust temperature follows the visual extinction dependence given by Hocuk et al. (2017). At the start of stage 1, the dust temperature ranges from 14.1 K to 13.3 K between the outermost edge of the cloud and the center. The central dust temperature falls to 5.3 K by the end of stage 1.

In stage 2, the full RHD model is employed (see Sec. 3.3.1) and the pre-collapse power-law profile achieved at the end of stage 1 undergoes gravitational collapse. Material that reaches a central sink region (radius 5 au) is lost from the envelope, representing mass accretion onto the central protostar, thus allowing the protostellar mass and luminosity to increase over time. Radiation from the protostar heats the surrounding dust, which rises to a maximum temperature of $\sim$730 K close to the protostar. Over time, mass continues to concentrate around the protostar, forming a disk that reaches a maximum density $n_\mathrm{H} \simeq 4 \times 10^{11}$. During stage 2, the total luminosity reaches a maximum value of 25 $L_\odot$. The final stellar luminosity is just over 1 $L_\odot$, while the final stellar mass is $\sim 0.744 M_\odot$ at the end of the model (See Figure 3.2).

Lagrangian tracer-particle trajectories are calculated in post-processing, and the resultant time-dependent physical conditions are fed to the chemical models to calculate the stage-1 and stage-2 evolution. In stage 2, the chemistry for each tracer particle is calculated throughout the simulation time or until it enters the inner boundary representing the protostar. Careful selection of the tracers is required to ensure good spatial coverage for the chemistry at any particular moment. A total of 12 evenly spaced “snapshot times” are chosen, and tracer particles selected, such that the instantaneous distribution of tracers provides good spatial coverage of the chemical results at those times (see Sec. 3.3.2).

As in the stage 1 model, the visual extinction values provided to the chemical models in stage 2 are based on a radial integration of the total hydrogen column density from the present position of each tracer. While this is simplistic, due to the divergence from spherical symmetry in stage 2, significant divergence only occurs relatively close to the center of the simulation, where visual extinctions are already so high that no external photons are able to penetrate. No protostellar UV-visual radiation is considered in the chemical modeling in the present simulations.

The RHD model is set up with a minimum temperature of 5 K. The protostellar luminosity influences the dust temperatures directly, but the gas temperatures are assumed to be fully coupled with the dust in the stage-2 simulations. When the dust temperature information is fed to the chemical models for each tracer particle, the values from the RHD model are combined with a visual extinction-dependent dust temperature obtained in the same way as in stage 1, such that the higher of the two values is always used. The extinction-based values never fall below around 5.3 K, thus this corresponds to the practical minimum value used in stage 2. For the

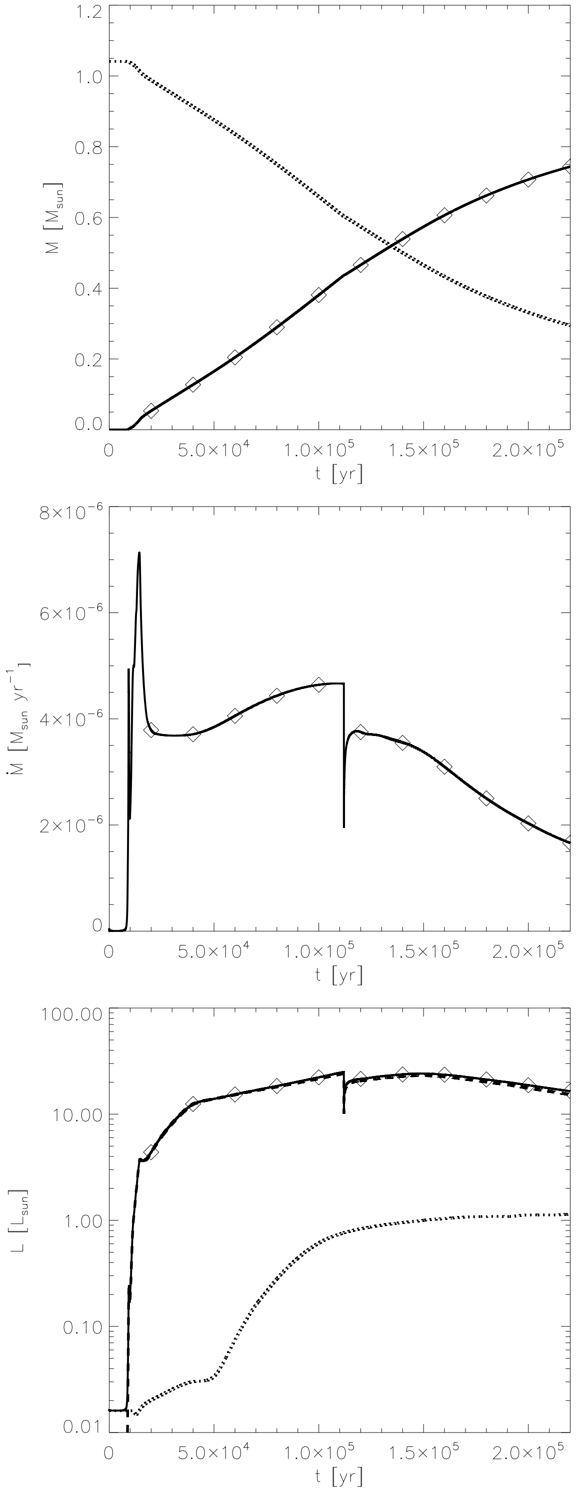

Figure 3.2 **Top:** Protostellar mass (solid) and envelope mass (dotted) during stage 2, the accretion phase. **Middle:** Mass accretion rate. **Bottom:** Total luminosity (solid), protostellar luminosity (dotted), and accretion luminosity (dashed). The twelve snapshot times are represented by diamond markers on each plot.

gas temperatures, the RHD-model temperatures are adopted, but with an imposed uniform minimum value of 10 K.

3.3.1 Radiation Hydrodynamical Model

The dynamical treatment uses a private version of the publicly available *ATHENA++* v20.0 code (Stone et al., 2008, 2020) that includes radiation, self-gravity and dust modules. These 2-D simulations use a fixed spherical-polar grid assuming ϕ displacement symmetry. The protostellar collapse starts from a power-law density profile (with $\rho \propto r^{-2}$), with an initial solid-body rotation and viscosity assigned. Matter that passes inside the central boundary (5 au radius) is added to the mass of the protostar. As the mass of the protostar grows, it irradiates the surrounding dust with photons, raising the temperature; the mass-luminosity relations of Hosokawa & Omukai (2009) are used.

A more detailed description of the dynamics of the collapse and accretion stages and the respective RHD equations is found in Bonfand et al. (in prep.), but using conditions appropriate to a hot core instead of the present hot-corino setup. The initial mass of the stage 2 protostar (i.e. that contained within the 5 au boundary) is 5.21×10^{-4} M$_\odot$; the final protostellar mass is $\sim$ 0.744 M$_\odot$. The initial mass of the envelope is $\sim$ 1.04 M$_\odot$ and the final envelope mass is $\sim$ 0.295 M$_\odot$. Figure 3.2 shows the protostellar (solid) and envelope mass (dotted) over time. The diamonds represent the twelve snapshot times in stage 2. The protostellar mass exceeds the envelope mass at $t = 134,610$ yr, which falls between the 7th ($t = 120,000$ yr) and 8th ($t = 140,000$ yr) snapshot times. The $t = 120,000$ yr snapshot time therefore represents the end of the Class 0 stage, under our simple definition.

The accretion rate of material falling onto the protostar ramps up quickly to a maximum value of 7.1×10^{-6} M$_\odot$ yr^{-1}, then falls over time. After the brief initial adjustment, the accretion rate of material falling onto the protostar stabilizes around $4 \times 10^{-6}\ M_{\odot}\ \mathrm{yr}^{-1}$ until the disk formation around 1.1×10^{5} yr. Afterward, the mass accretion rate drops to about $3.5 \times 10^{-6} M_{\odot}\ \mathrm{yr}^{-1}$ as a result of the mass retained by the disk, and it continues to decline later in the simulation as more and more mass accumulates in the disk. The luminosity of the protostar reaches 10 $\mathrm{L}_{\odot}$ early on and varies between 10 and 25 $\mathrm{L}_{\odot}$.

3.3.2 Placement of tracer particles

The placement of tracer particles and the calculation of their trajectories are conducted in post-processing to ensure that adequate 2-D spatial coverage is obtained at a series of 12 key "snapshot" times between the beginning and end of the RHD simulation, distributed in 20,000 year increments. Good spatial coverage is necessary in order to determine the spatial distribution of molecules at a particular moment, and thence to calculate column densities or molecular emission that can be directly compared with observational data.

As in the study of Bonfand et al. (in prep.), the RHD simulations (stage 2) are conducted first, with tracer particles assigned based on the completed stage-2 results. Tracer particles are initially placed in the final snapshot frame ($t = 220,000$ yr), and then evolved backward in time toward the start time of the dynamical calculations, based on the instantaneous local velocity vectors. Tracers are placed only in the upper quadrant, because the upper and lower quadrants are symmetrical in the dynamical calculations. This first set of tracer particles is by definition the group that survives throughout the entire RHD model run, i.e. they never traverse the inner boundary that represents the protostar nor are they lost through the outer boundary. At the penultimate snapshot time, there exists a central region that is (mostly) devoid of tracers belonging to the first set; this region must be re-populated with new particles.

These are added and their trajectories are also backward-calculated to the start time. New tracers are added for each earlier snapshot time, and this process continues until adequate spatial coverage is achieved at all snapshot times. The number of snapshot times required is thus a key determinant of the number of chemical models that must be run.

The adequacy of spatial coverage is determined based on several key criteria, set to ensure that the disk and the inner and outer regions of the envelope are well sampled. In the same way as in Bonfand et al. (in prep.), tracer particles are populated into a space based on a minimum spatial separation between new particles, as well as adding additional particles to ensure good sampling as a function of local density and density gradient. Because of the smaller scale of the hot corino setup, the innermost regions are overpopulated with tracers using this method, which initially produces ∼25,000 tracers. An additional routine is used to thin the population, such that: in regions at radial distances >300 au, particles are never closer than 250 au; in regions within this boundary, particles are never closer than 5 au; and in regions at radial distances <200 au where the local temperature exceeds 80 K, particles are never closer than 3 au. These stipulations ensure that sampling is much smaller than the scale size of the disk, especially as its temperature approaches the sublimation temperature of the ices. A total of 3413 tracer particles are ultimately simulated with the chemical models.

The distribution of the tracer particles at large spatial scales during the stage-2 evolution is shown in Figure 3.3. Note that the tracers are placed in the upper quadrant and are shown mirrored in the lower due to the symmetry of the simulations. The first six panels represent Class 0 and the bottom six represent Class I. The apparent concentric rings correspond to high concentrations of tracer particles associated with the inner regions of the core at later snapshot times; particles within

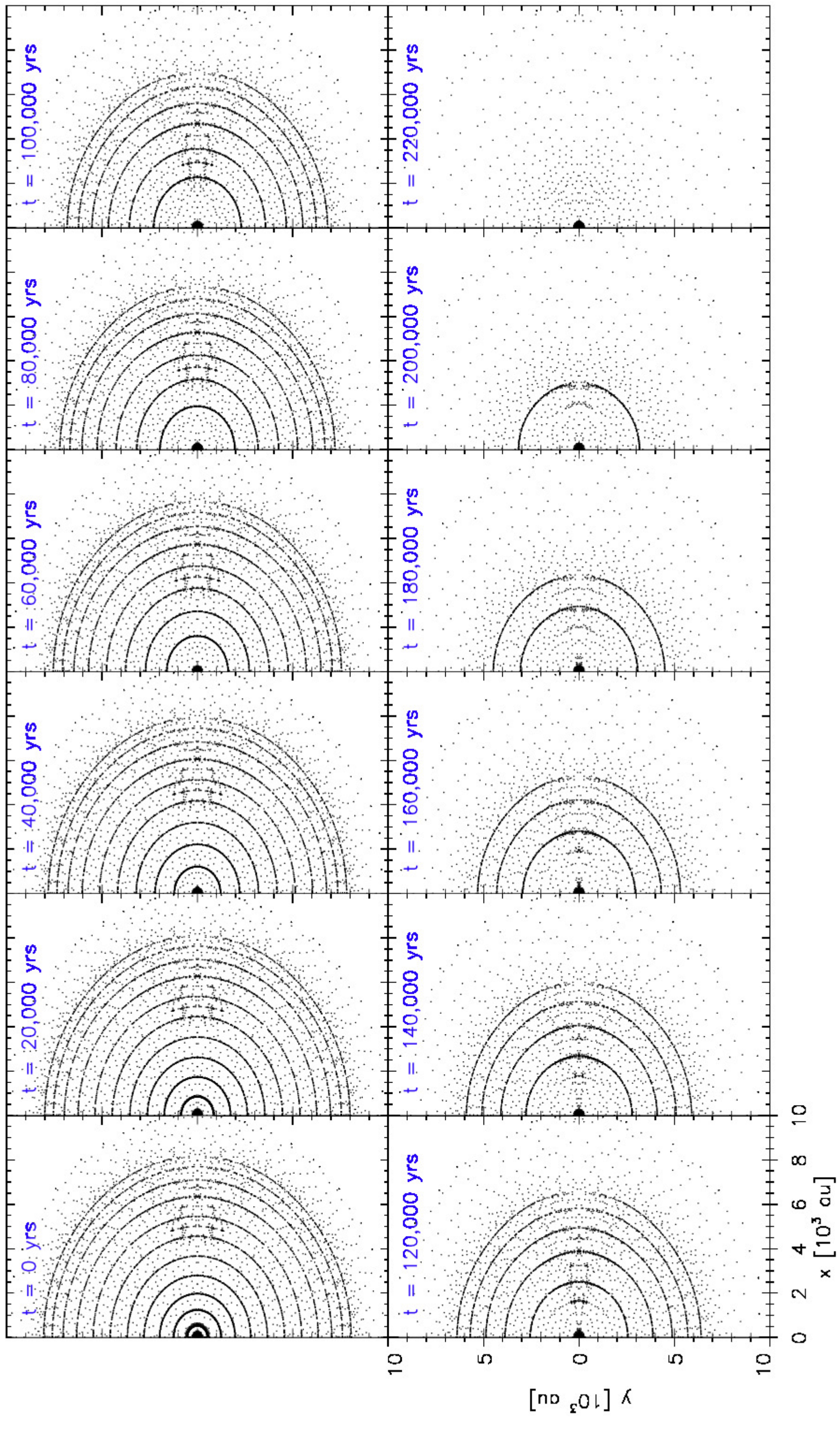

Figure 3.3 The trajectory positions over the twelve snapshot times.

the "rings" become more spatially distinct as they get closer to the protostar since they trace gas parcels that experience forces of different strengths and directions and thus follow different trajectories to the central region.

Once the positions of the tracer particles in stage 2 are determined, they are traced backwards in time through stage 1, all the way to a uniform cloud. The collected stage-1 and stage-2 trajectory information, consisting of gas density, dust temperature, and visual extinction, is then provided to the chemical model to run forward in time for each tracer particle.

3.3.3 Chemical Model - MAGICKAL

This project uses the three-phase (gas/surface/ice-mantle) gas-grain chemical kinetics code MAGICKAL (Garrod, 2013). The network contains a total of 1511 species in the gas, surface, and bulk with 4,238 independent grain reactions, 543 cosmic-ray induced UV photodissociation reactions, 554 external UV reactions, and 661 gas-phase reactions. The cosmic-ray ionization rate is set at a constant value of 1.3×10^{-17} s^{-1}. Initial elemental abundances also follow (Garrod, 2013).

MAGICKAL has a full, self-consistent framework for the treatment of both diffusive and non-diffusive grain-surface and bulk-ice chemical reactions. Production of COMs on grains in the early pre-stellar stage when grain temperatures are on the order of 10 K requires non-diffusive mechanisms. The present framework follows Jin & Garrod (2020) and Garrod et al. (2022), who formulated rate treatments for non-diffusive mechanisms including "three-body" reactions, in which an initiating surface reaction leads to an immediate follow-on reaction of the product with some other nearby species, without mediation by thermal diffusion. This framework was also applied to photodissociation-driven chemistry, thus avoiding any requirement for the thermal diffusion of radicals in the bulk ices, removing much of the temperature dependence, and shifting the onset of photo-production of COMs to low temperatures, in line with laboratory evidence (e.g. Henderson & Gudipati, 2015).

Identical to the Bonfand et al. (2025) model, when temperatures exceed 250 K and the number of surface and bulk-ice atoms or molecules fall below 10 and 1, respectively, the MAGICKAL code shifts into 2-phase mode (i.e. grain-surface and gas-phase chemistry only), which does not affect model outcomes but makes it significantly more efficient. The code switches back to 3-phase operation when any of these conditions no longer apply.

3.3.4 Column Density Calculations

In this paper, we calculate the column densities of various species and compare with observations. Because our principle focus here is the ice abundances, we simply calculate a straight-line integration of column densities from the edge of the core to the center, at any particular point in time.

During the stage 1 isotropic contraction of a cloud, the physical conditions of all tracer particles are dependent only on radial position. Thus, the chemical results for every tracer particle in stage 1 can be used to provide a high radial-resolution profile for each molecule. These profiles are integrated to give an isotropic column density for each species. Although in stage 1 there is no central IR source (i.e. protostar) against which ice absorption spectra would be observed, we use an edge-to-center integration method to be consistent with stage 2. Stage 1 contains 1000 time-points and due to the absence of a central sink, all of these times may be considered spatially well sampled.

The stage 2 column density calculations follow the same method; however, due to the 2D behavior of the core, it is no longer appropriate to calculate purely radially dependent values. With the formation of the disk around the class 0/I transition, this is especially apparent. Thus in stage 2, each molecular column density integration is carried out along a specific inclination angle, ending at the inner edge of the simulation.

3.4 Results

3.4.1 Hydrodynamical Data

An important part in understanding the results of the subsequent chemical modeling of each trajectory is first evaluating how the hydrodynamical model is behaving. In Section 3.3, we describe the model setup by detailing how the stage 1 and stage 2 conditions vary over time. In Section 3.3, Figure 3.1 shows the visual extinction, density, and temperature behavior across the cloud radius over time. Here we give the results of the density, temperature, and trajectory pathways in stage 2. In stage 2, the physical conditions start to vary throughout the envelope, so we present a contour map of the density and temperature.

Figure 3.4 shows the gas density distribution of the RHD model in the inner 300 AU of the simulation for twelve snapshot times in stage 2. The first six snapshots, from $t = 0$ yrs to $t = 120,000$ yrs, correspond to a class 0 YSO. At the eighth snapshot, the mass of the surrounding envelope is less than the protostar mass, which then classifies it as the first snapshot for a class I YSO. At the snapshot time of $120,000$ yrs, a disk starts to form as demonstrated by the sudden jump in density around the midplane.

The temperature distribution over the twelve snapshot times is shown in Figure 3.5. Once the disk starts to form at $t = 120,000$ yrs, the temperature profile starts to evolve to form a lower temperature distribution towards the midplane of the disk. The inner 50 AU encompasses temperatures that go as high as 729K.

Another physical feature of the hydrodynamical setup is the effect of the density

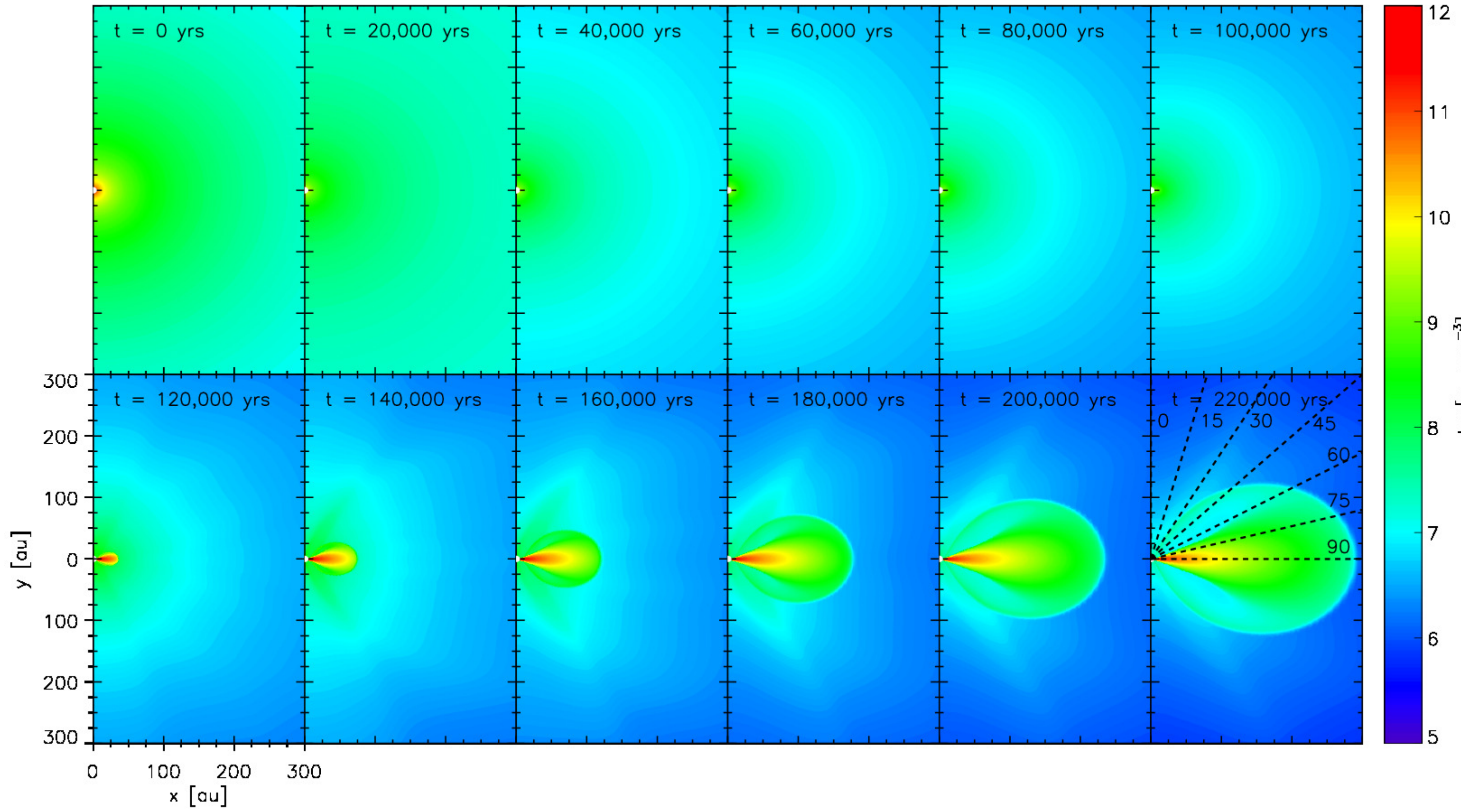

Figure 3.4 The density distribution over the twelve snapshot times. The last panel includes an overlay of selected inclinations, or viewing angles, into the disk, ranging from 0° (face-on) to 90° (edge-on).

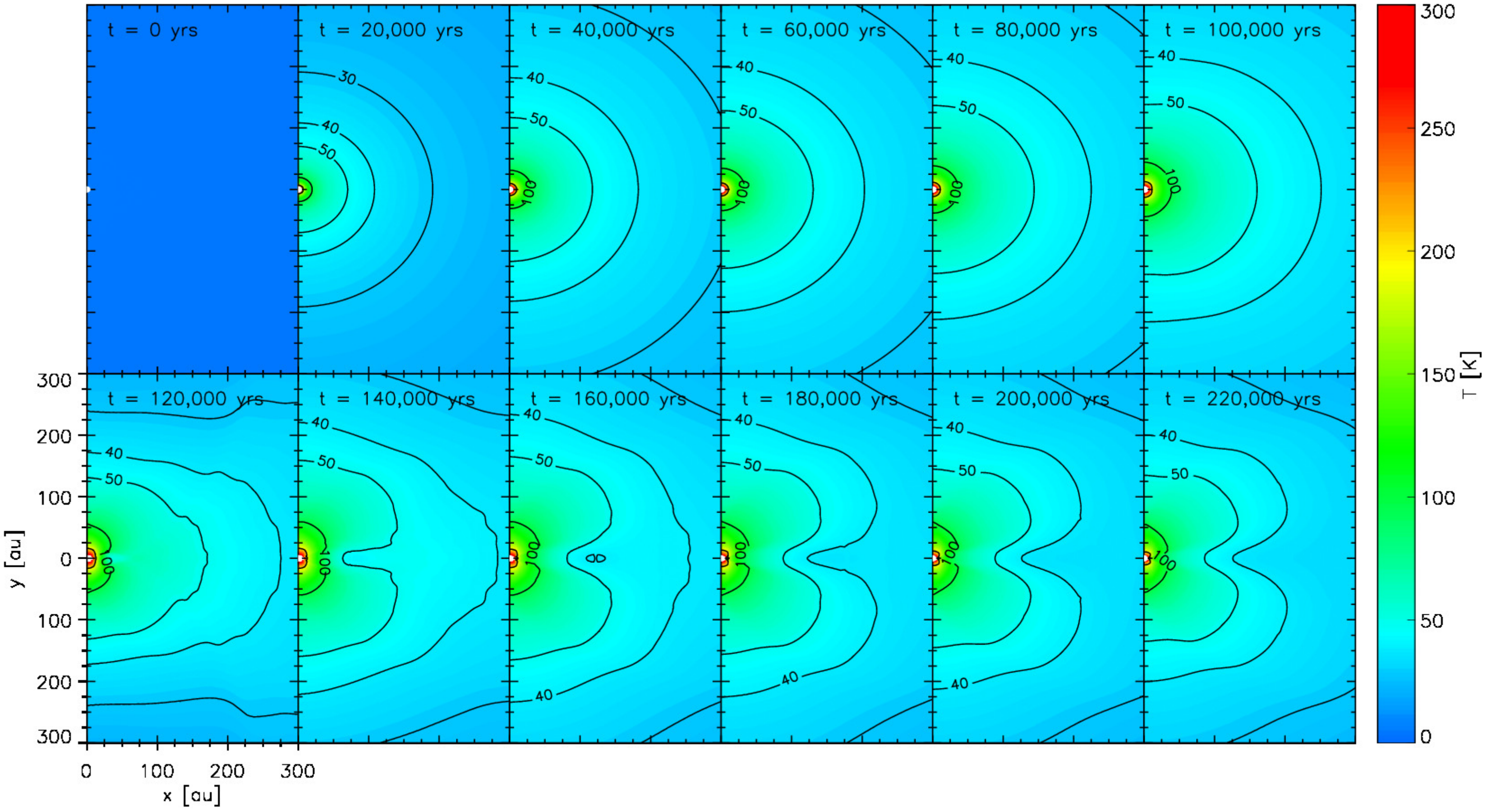

Figure 3.5 The temperature distribution over the twelve snapshot times. The innermost, unlabeled contour value corresponds to 200 K, with the labeled rings corresponding to 100 K, 50 K, and 40 K. The unlabeled outermost contour is 30 K.

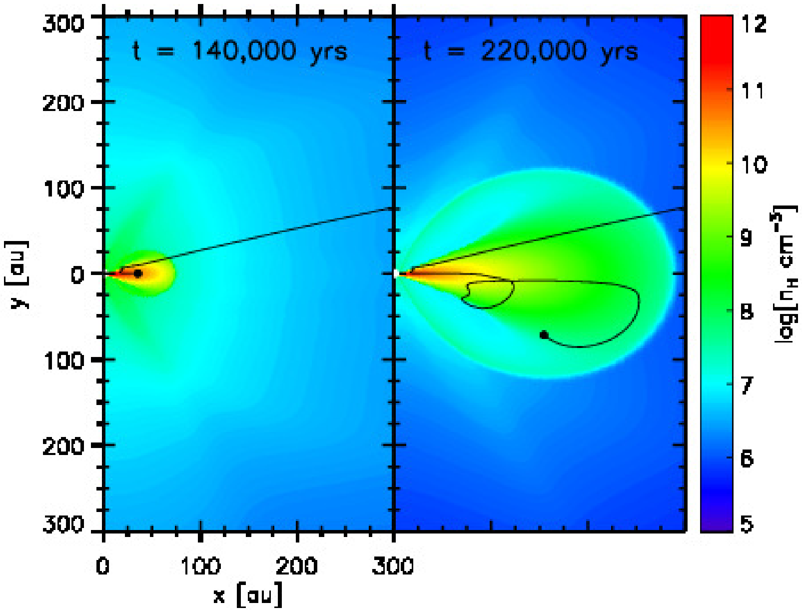

Figure 3.6 The pathway of a trajectory that experiences meridonial circulation.

profile and disk velocity field on the pathways of the trajectories. As the disk starts to form around $t = 120,000$ yr, the trajectories that accrete onto the disk will, in general, continue to travel outwards with the growing disk. Most trajectories are pulled toward the protostar and if their velocity is such that they join the disk, we have found that the trajectories are traveling outward along the midplane, likely as a result of angular momentum redistribution inside the disk, with the midplane material gaining angular momentum and thus expanding outward. The midplane expanding gas is stopped near the (radial) outer edge of the disk by the envelope infall, where it is forced to move upward (away from the midplane) before circulating back toward the central protostar, forming large meridional vortices that were also present in Tu et al. (2022) and Bhandare, Asmita et al. (2024); the latter authors considered the flow pattern a form of “turbulence." This physical effect is demonstrated in Figure 3.6 in which the (past) path taken by a tracer is shown, with a dot indicating the current position. This effect occurs within the disk and also occurs on the outer edge of the disk.

3.4.2 Pre-stellar Ice Abundances

In stage 1, the collapse stage, the molecular cloud is assumed to be spherically symmetric but the physical conditions are allowed to vary radially. Therefore, we are capable of tracing how the chemical abundances change with radius as the cloud collapses. In this stage, due to cold temperatures (<10K) COMs are mostly formed on the grain through non-diffusive mechanisms.

Figure 3.7 shows the abundances of simple solid-phase species and COMs for the time halfway through the pre-stellar collapse, at $t = 500,000$ years. The abundances are plotted against radius (bottom x-axis) and visual extinction (top x-axis). Figure 3.8 shows the chemical abundances against radius at $t = 1,000,000$ years, the end of stage 1. The species selected in these plots are the same species that we have observational data for above in Table 3.1.

For the species HCN, CH_3CN, HNCO, and OCS, there is an increase in chemical abundance around a radius of $0.9 - 1.5 \times 10^4$ AU. This increase is happening at visual extinctions of 1.2-1.8 mag. This abundance increase is in effect at all times in the stage 1 model and is seen in both Figure 3.7 and Figure 3.8. At the visual extinction of 1.2-1.8 mag, the conditions become more favorable for ice production. Outwards toward the edge of the cloud, the visual extinction will decrease down to 1 mag, and these molecules are more strongly affected by the external UV radiation and the molecules are destroyed by UV photodissociation. Inwards from this threshold radius, the abundance decreases again because of the increasing density and visual extinction. The increasing hydrogen number density increases the hydrogen accretion onto the grain and these species are converted into other species by H-atom addition.

The remaining species do not experience this decrease in abundance toward the

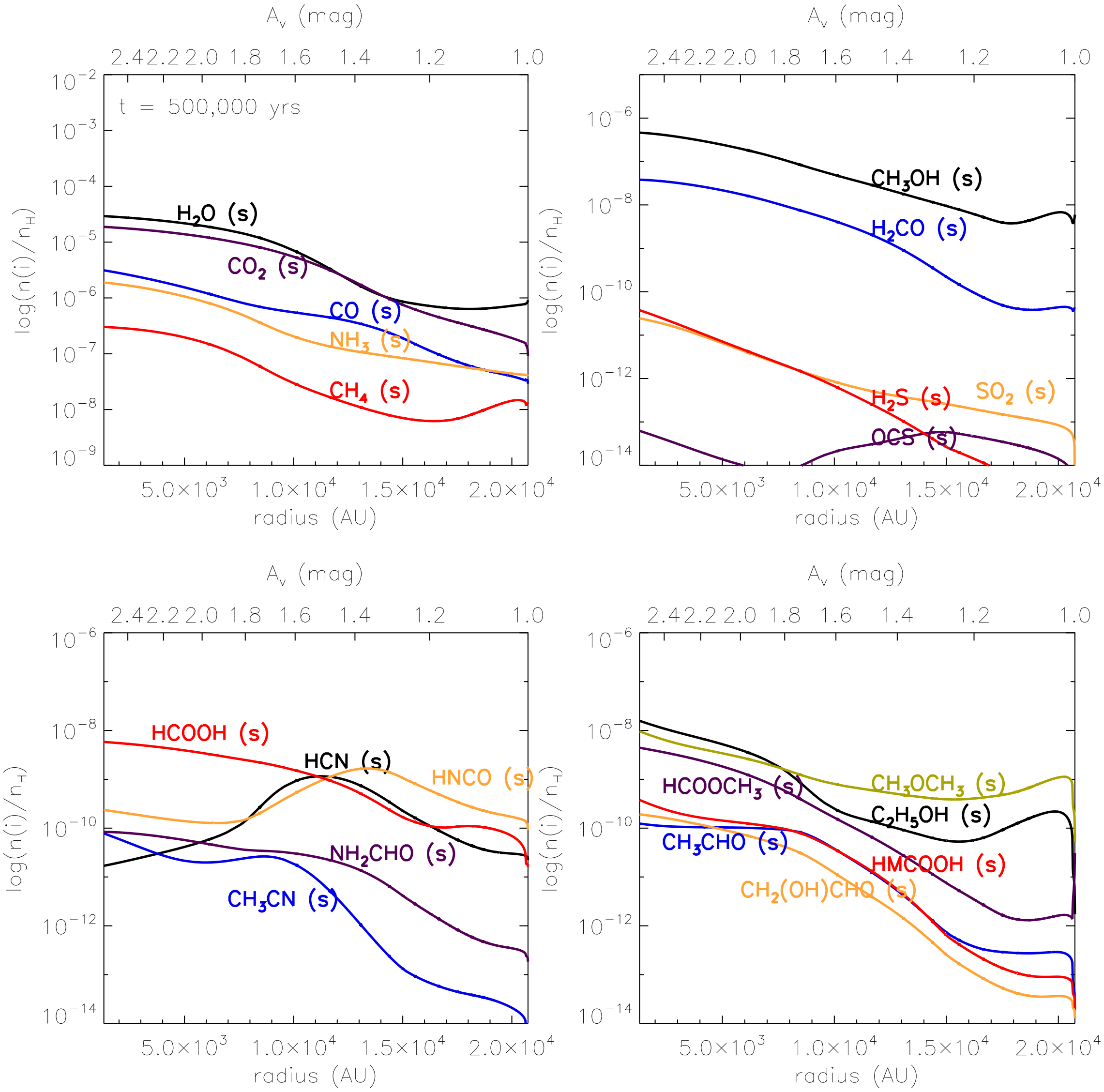

Figure 3.7 Abundances of various chemical species at $t = 500,000$ yrs during the pre-stellar collapse.

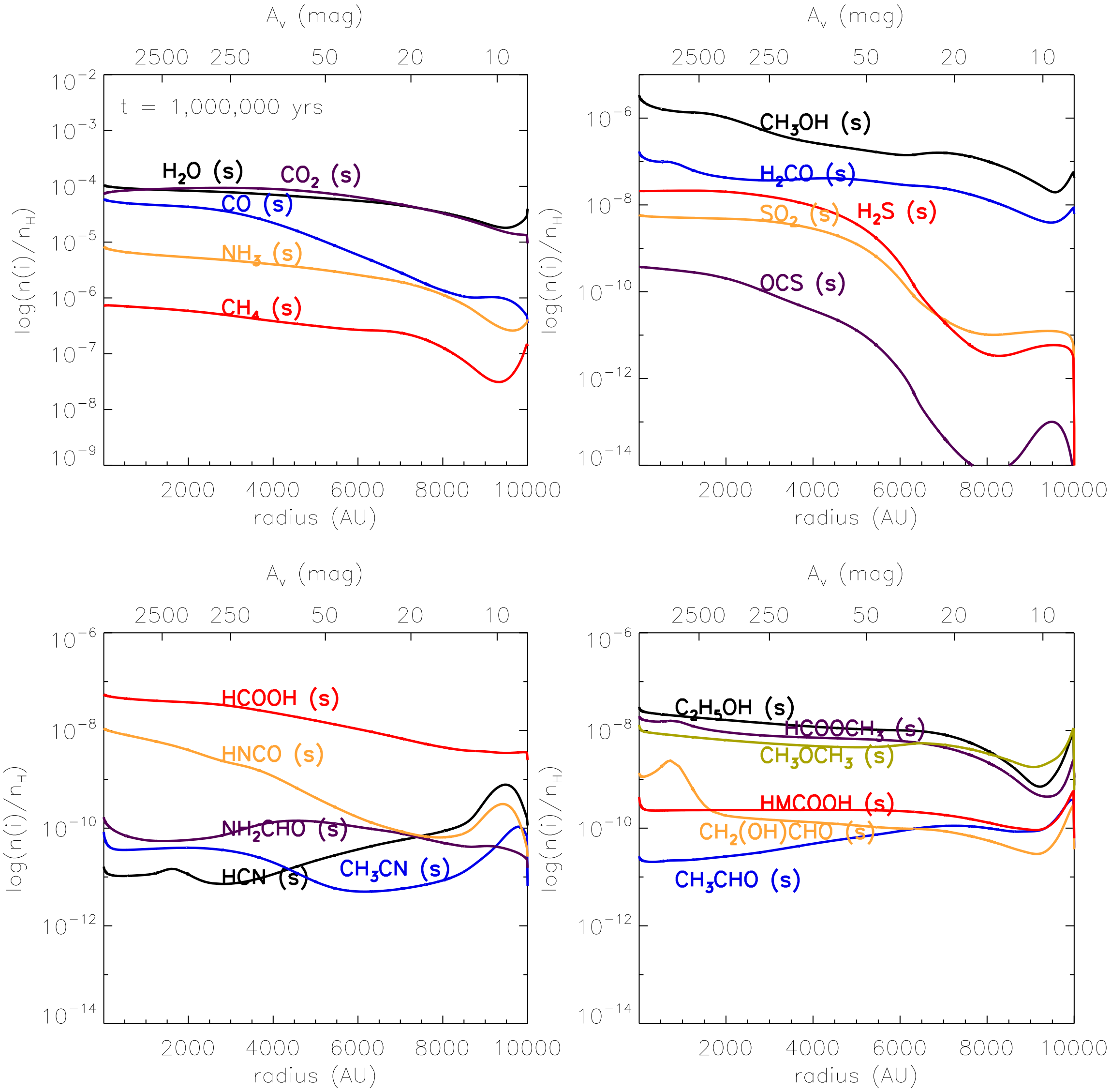

Figure 3.8 Abundances of various chemical species at $t = 1,000,000$ yrs during the pre-stellar collapse.

inner part of cloud because they have a higher hydrogenation barrier. Therefore, their abundance will remain stable.

As time progresses and the density increases toward the center of the cloud, the ice production increases in a wave from inner radius to outer radius. As the ice production ramps up in the inner part of the cloud, the abundances of the species increase, but the outer radii has not been affected as it takes time for the outer radii abundances to catch up. Therefore, as time progresses and outer radii reach higher density values, the abundance increases in a wave-like behavior. This behavior is seen more clearly when comparing the abundances between closer increments of time but it can also be seen in Figures 3.7 and 3.8. For example, if you trace the abundance of acetic acid, CH_3COOH, between the two figures the abundance has increased by $\sim$2 orders of magnitude at outer radii from $t = 500,000$ years to $t = 1,000,000$ years.

For the species SO_2, OCS, and H_2S, there is an even more apparent general destruction trend as the radius increases. H_2S specifically is desorbed very rapidly (Garrod et al., 2007) due to cyclic hydrogen abstraction reactions that have a very low activation energy (Garrod et al., 2007).

3.4.3 Protostellar Ice Abundance Maps

Whereas in the pre-stellar collapse phase where there is only radial variation in abundance, the protostellar phase involves a two-dimensional spatial dependence due to the formation of a disk. In general, as the disk structure begins to form, the density increases towards the midplane (see Figure 3.4) and the temperature will decrease along the midplane (see Figure 3.5. Temperatures are highest nearest the protostar and reach values as high as 729 K.

During the protostellar phase, there are various hydrodynamical processes in place that affect the pathways of trajectories as described in Section 3.4.1.

In Figure 3.9, the top panel shows the chemical abundance of CO for the last six snapshot times, representing the formation of a disk. This plot shows the paths of two representative trajectories that result in different chemical abundances due to physical effects. Each trajectory's path is indicated by the line that follows behind. The solid-line trajectory path is pulled towards the protostar as it falls inward with other accreting material. Instead of falling into the protostar, it is pushed along the midplane of the disk until it ends up near the middle of the disk, with a "normal" abundance.

However, the dashed-line trajectory experiences a different path and subsequently, a lower abundance. This trajectory gets closer to the protostar than the solid-line trajectory. This path closer to the protostar makes this trajectory subject to higher temperatures. The dashed-line trajectory experiences a temperature of 164K nearest the protostar, which is higher than the temperature required to desorb water in our model (120K). In contrast, the solid-line trajectory only reaches a temperature of 116 K. Once water is desorbed from the grain surface for the dashed-line trajectory, other grain species will rise to the surface and desorb. Each species will desorb depending on the temperature required to desorb them from the surface. The dashed-line trajectory reaches a temperature high enough to desorb CO from the grain surface and results in a lower CO abundance on the grain.

After the close approach to the protostar, the dashed-line trajectory is then pushed out along the midplane. This trajectory is then subject to meridonial circulation, as described in Sec. 3.4.1, in which it is pushed out of the midplane and then recycled back into the midplane of the disk. The trajectory continues along the midplane but is then pushed out at the edge of the disk due to the external pressure due to the sharp pressure drop and is recycled once again. However, in the case with this trajectory, this trajectory has a much lower abundance than the solid-line trajectory.

This is denoted by the lower abundance color (green) in comparison to the solid-line trajectory's higher abundance color (orange), which represents over two orders of magnitude of abundance difference.

These two trajectories are just examples of two common paths for trajectories, and similar effects are seen in other trajectory paths. All trajectories that end in a low-abundance pocket experienced high enough temperatures as they approached the protostar to desorb CO off the grain.

In addition to this low-abundance effect in place along different trajectory paths, it is also seen across species. Not only is CO subject to this low-abundance pattern, but so are other simple species and COMs. The abundance maps for methyl formate ($HCOOCH_3$) and glycolaldehyde ($CH_2(OH)CHO$) are also included in Figure 3.9 as examples of this low-abundance behavior present for other species. The dashed-line trajectory for methyl formate experiences a drop in abundance of about 2 magnitudes, similar to CO. However, glycolaldehyde's dashed-line trajectory only experiences a drop of less than one magnitude by the end of stage 2. Figure 3.10 plots the ice abundances over time of simple species and COMs for the dashed-line trajectory. The plot on the left shows species that experience the low-abundance effect. Glycolaldehyde desorbs off the grain but partially regains its abundance by the end of stage 2. In comparison to methyl formate, glycolaldehyde has a higher binding energy. Methyl formate will more easily desorb due to its lower binding energy and will stay desorbed. However, because of glycolaldehyde's higher binding to the surface due to its hydroxyl group that forms hydrogen bonds to water on the grain surface, it accretes back onto the grain over time. The relationships between methyl formate and glycolaldehyde are explored in more detail in Jin & Garrod (2020); Garrod et al. (2022); Shope et al. (2024).

In the plot on the left side of Figure 3.10, note the drop in abundance not only

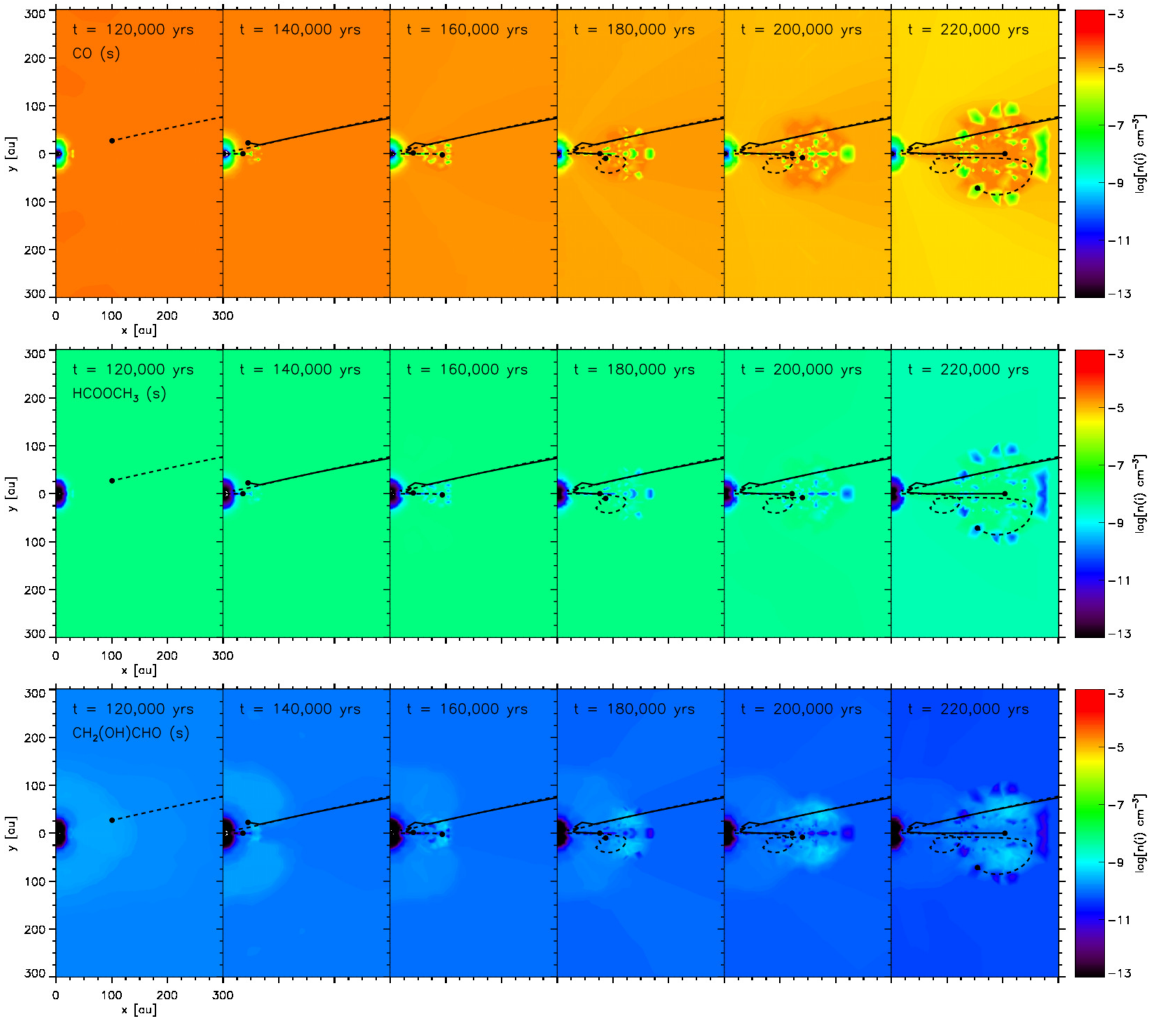

Figure 3.9 Abundance map of CO, HCOOCH$_3$, and CH$_2$(OH)CHO with respect to hydrogen. The solid-line corresponds to typical trajectory in the model. The dashed-line corresponds to a trajectory that has a near approach to the protostar, experiences high enough temperatures to desorb species from the grain, and results in a low-abundance pocket at the end of the model.

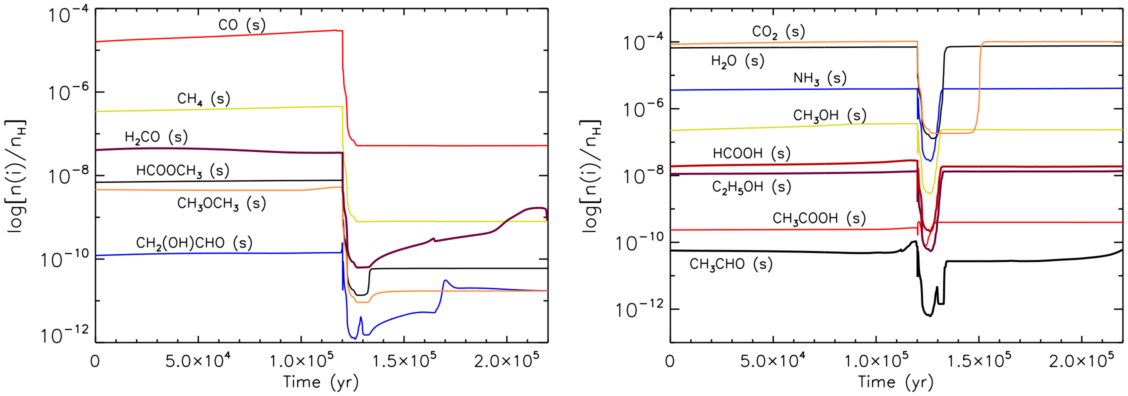

Figure 3.10 Chemical abundances of various ice species over time for the dashed-line trajectory that has a close enough approach to the protostar to affect final species abundances. **Left:** Ice species that experience a rapid decrease in abundance and never fully recover. **Right:** Ice species that experience a rapid decrease in abundance but are able to recover to an abundance close to its original value before the close approach.

in CO and methyl formate, but also in other species such as CH_4 and CH_3OCH_3. The right side plot in Figure 3.10 shows ice species that are able to recover their abundances after their exposure to high temperatures. These species are desorbed but due to their high binding energies, they accrete back onto the grain.

3.4.4 Ice Column Densities

In order to compare to observations, we calculate the column density of each species along a line of sight (see Sec. 3.3.4). The lines of sight we consider are different inclinations, or viewing angles, into the protostar. For Class -I, every viewing angle yields the same column density as we assume spherical symmetry in the molecular cloud and there is no substantial effect on the column densities due to inclination until the model reaches Class I when the protostellar disk starts to form. Figure 3.11 plots the stage 1 (Class -I) and stage 2 (Classes 0 and I) absolute column density of water over time. In stage 2, there are twelve snapshot times we consider and each are denoted by a symbol. A vertical line that divides Class 0 from Class I is placed over the snapshot time in which the disk starts to form. The symbols correspond to a different inclination. Although inclinations from 0 to 90 were examined in increments of 15 degrees, Figure 3.11 shows only the inclinations of 90, 75, 60, and 0. The inclinations between 0 and 60 degrees are not shown in Figures 3.11, 3.12, 3.13, 3.14, and 3.15 as the values are all very close to each other, as will be discussed in the following sections.

The range of the absolute column density values of water are in Table 3.1 for Class -I and Table 3.2 for Classes 0 and I.

In addition to the absolute water ice column densities, the fractional column densities of various species with respect to water are plotted in Figures 3.12, 3.13, 3.14, and 3.15. The range of fractional column density values over time for Class -I is reported in Table 3.1. The range gives the minimum value reached and the maximum value reached. The range of fractional column density values for stage 2 (Classes 0 and I) are listed in Table 3.2 for all times and all inclinations.

Observational Comparisons

The model's calculated column densities of ices in Classes -I, 0, and I are compared to the column densities obtained from JWST data and other data taken from the literature. The JWST data includes observations of cloud ices toward two background stars NIR38 and J110621 from McClure et al. (2023), class 0 sources NGC 13333 IRAS 2A from Rocha et al. (2024), and class 0 source CED 110 IRS4A from Rocha et al. (2025). NIR38, J110621, and IRS4A observations were a part of the Early Release Science program, *Ice Age*, and details of their observations can be found within their referenced articles.

NIR38 and J110621, observed by McClure et al. (2023), are sightlines associated

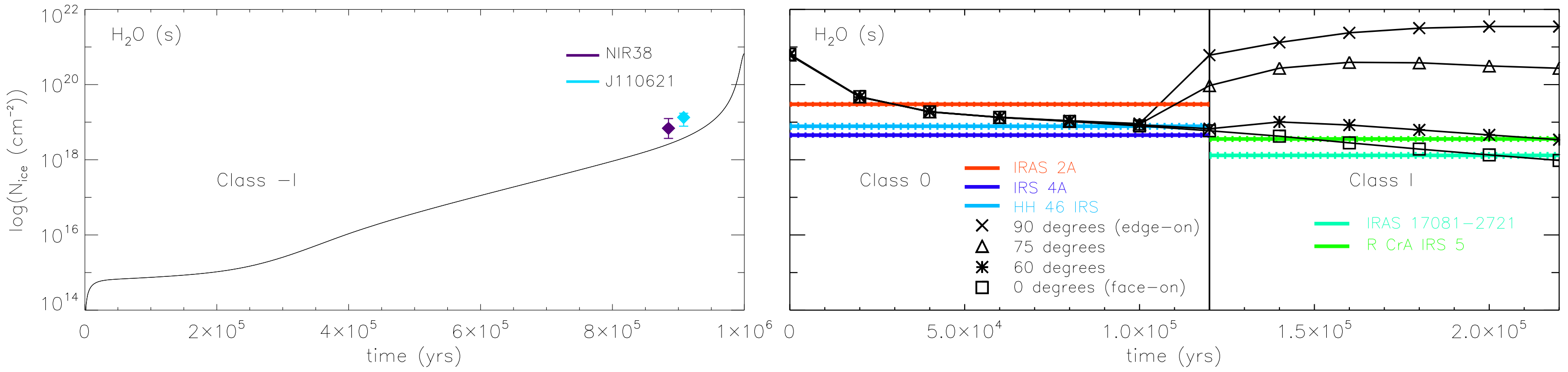

Figure 3.11 Stage 1 (Class -I) and stage 2 (Class 0 and I) ice column densities of water obtained from our model. Stage 1 column density of water is compared to ice observations towards two background stars, NIR38 and J110621 (McClure et al., 2023). The observational values of the NIR38 and J110621 sources have been placed at the time in the model in which the visual extinction matches the source's calculated visual extinction. The calculated visual extinctions of NIR38 and J110621 are 34 mag and 47 mag, respectively (Jimenez-Serra et al. (in prep)). Stage 2 water column density is compared to observations of IRAS 2A (Rocha et al., 2024), IRS4A(Rocha et al., 2025), and HH46 IRS (Boogert et al., 2008) for Class 0 and IRAS 17081-2721 and CrA IRS 5 (Boogert et al., 2008) for Class I. The vertical black line separates Class 0 and Class I. In stage 2, there are twelve snapshot times represented by a symbol, with different symbols corresponding to various inclinations. Inclination of 90 degrees (edge-on) is marked by a cross symbol, 75 degrees is a triangle, 60 degrees is an asterisk, and 0 degrees (face on) is a square. The vertical line aligns with the first time in the model where there is a divergence in column density due to inclination.

Table 3.1 Observed and modeled absolute column density value of water, N_{ice}, and column densities with respect to water, $X_{\mathrm{H_2O}}(\%)$ for Class -I. Values for NIR38 and J110621 are reproduced from McClure et al. (2023) and the range reported in Boogert et al. (2015) for various molecular cloud sources is listed. Modeled column densities are obtained by integrating the abundances in the uniform molecular cloud from edge to center. The reported model values give a range from minimum column density to maximum column density over all time in stage 1.

Species	NIR38	J110621	Boogert 2015	Model Class -I
$N_{\mathrm{ice}}(\times 10^{18}\mathrm{cm}^{-2})$				
H_2O	6.88	13.38	-	0-669
$X_{\mathrm{H_2O}}(\%)$				
H_2O	100	100	100	100
CO	43.02	27.50	9-67	7.84(-2)-55.9
CO_2	20.06	13.00	14-43	2.69(-1)-85.0
CH_3OH	8.87	3.36	<12	2.63(-1)-2.78
NH_3	4.36	4.93	<7	3.54-7.76
CH_4	2.62	1.87	<3	6.33(-1)-4.02
OCS	0.15	0.15	<0.22	2.01(-8)-3.61(-4)
SO_2	0.05	0.04	-	2.26(-9)-5.60(-3)
H_2S	0.58	-	-	7.34(-7)-2.08(-2)
HCN	0.87	0.67	-	1.30(-5)-2.47(-2)
CH_3CN	2.03	1.42	-	3.63(-5)-8.44(-4)
H_2CO	-	-	-	3.02(-4)-1.42(-1)
HCOOH	-	-	<2	4.64(-4)-5.15(-2)
CH_3CH_2OH	-	-	<2	1.25(-2)-1.39(-1)
CH_3CHO	-	-	-	2.26(-5)-1.72(-3)
$HCOOCH_3$	-	-	-	6.61(-6)-1.75(-2)
CH_3COOH	-	-	-	1.22(-6)-1.14(-3)
$CH_2(OH)CHO$	-	-	-	5.25(-7)-1.73(-3)

Table 3.2 Observed and modeled absolute column density value of water, N_{ice}, and column densities with respect to water, $X_{\mathrm{H_2O}}(\%)$ for Class 0 and I. IRAS 2A column density values are reproduced from Rocha et al. (2024), IRS 4A values from Rocha et al. (2025), and HH 56 IRS, IRAS 17081-2721, and R Cr A IRS 5 values reproduced from Boogert et al. (2008). The range reported for modeled column densities include all inclinations over all time for each respective YSO class.

Species	IRAS 2A	IRS 4A	HH 46 IRS	IRAS 17081-2721	R Cr A IRS 5	Model	Model
$N_{\mathrm{ice}}(\times 10^{18}\mathrm{cm}^{-2})$							
H_2O	30.0	4.52	7.79	1.31	3.58	5.92-639	9.58(-1)-3.51(3)
$X_{\mathrm{H_2O}}(\%)$							
H_2O	100	100	100	100	100	100	100
CO	-	-	-	-	-	18.7-56.1	4.53-34.0
CO_2	-	24.5	-	-	-	65.4-149	19.5-162
CH_3OH	7.7	2.1	5.5	3.3	6.6	4.72(-1)-3.00	1.24(-1)-5.21(-1)
NH_3	-	6.4	-	-	-	5.56-7.84	2.86-6.70
CH_4	1.6	1.7	-	-	-	2.80(-1)-7.25(-1)	7.12(-2)-5.62(-1)
OCS	-	-	-	-	-	3.09(-4)-1.72(-3)	2.72(-4)-4.18(-3)
SO_2	0.2	-	-	-	-	5.58(-3)-1.88(-2)	1.83(-3)-4.15(-2)
H_2S	-	-	-	-	-	9.32(-3)-2.30(-2)	7.54(-4)-1.55(-2)
HCN	-	-	-	-	-	1.43(-5)-7.75(-4)	2.57(-5)-8.29(-4)
CH_3CN	-	-	-	-	-	4.29(-5)-1.46(-4)	1.38(-5)-1.34(-4)
H_2CO	4.1	<7.5	-	-	-	2.22(-2)-1.52(-1)	6.00(-3)-4.65(-2)
HCOOH	1	2	2.7	<2.4	<4.1	3.90(-2)-5.18(-2)	2.56(-2)-4.88(-2)
CH_3CH_2OH	1.2	-	-	-	-	1.89(-2)-2.76(-2)	1.14(-2)-2.29(-2)
CH_3CHO	0.7	-	-	-	-	2.40(-5)-1.79(-4)	5.16(-5)-1.62(-4)
$HCOOCH_3$	0.10	-	-	-	-	4.99(-3)-1.80(-2)	1.48(-3)-1.14(-2)
CH_3COOH	0.3	-	-	-	-	2.84(-4)-9.88(-4)	4.86(-4)-1.22(-3)
$CH_2(OH)CHO$	-	-	-	-	-	2.06(-4)-1.24(-3)	4.45(-5)-2.35(-4)

with the molecular cloud that is close in the sky to CHA MMS 1. Although these sightlines might note be directly related to a star-forming core, it is valuable to compare their ice abundances with our calculations during the pre-stellar core stage. Both sightlines were measured to have visual extinctions of 34 and 47 mag, respectively (Jimenez-Serra et al. (in prep)). In these measurements, the visual extinctions are based on absorption of the background stars' light through the entire cloud. To compare with our model, we therefore find the time which the model reaches an inner visual extinction equal to half the observed value, which is 17 mag and 23.5 mag for NIR38 and J110621, respectively. Therefore, the times that our inner most trajectory experiences visual extinctions of 17 mag and 23.5 mag are at times $t = 88,500$ years and $t = 90,800$ years in stage 1. These are the times where the data points are placed for NIR38 and J110621.

IRS4A was another source of study in the *Ice Age* program looking at the ice inventory in the class 0 source. IRS 4A has a visual extinction of 30 mag (Persi et al., 2001). The Rocha et al. (2024) JOYS+ program explored COM ice signatures in the low-mass class 0 IRAS 2A source. IRAS 2A is reported to have a bolometric luminosity of 20-25 $L_\odot$ (Brinch et al., 2009) and the mass of the envelope is 1.7 $M_\odot$ (Jørgensen et al., 2005).

For the class -I model data, we also compare to the range of column densities reported in Boogert et al. (2015). The Boogert et al. (2008) paper reports on column densities from the c2d spectroscopic survey of ices around low-mass YSO using the Spitzer Space Telescope. Of the sources included, we include HH 46 IRS, IRAS 17081-2721, and R Cr A IRS 5, all of which have conditions comparable to our models, have column densities reported for H_2O, CH_3OH, and HCOOH, and are reported by Boogert et al. (2008) to be in the range of $\sim 0.1 - 10$ $L_\odot$. HH 46 IRS is a class 0/I source Rocha & Pilling (2020) and has a luminosity of 12 $L_\odot$ (Adams et al., 1987;

Emerson et al., 1984). IRAS 17081-2721 is a class I protostar (Rocha & Pilling, 2020) and R Cr A IRS 5 is a class I source (Rocha & Pilling, 2020) with a solar luminosity $<9\ L_{\odot}$.

These sources were chosen because their mass and/or luminosity are comparable to the model which has a range of 10-25 $L_{\odot}$ and $\sim$0-1$M_{\odot}$. We report above values we were able to find in the literature concerning mass, luminosity, visual extinction, and class. We determined that the information above was sufficient enough for our choice of these sources for comparisons to our models.

The observed column densities of various species for all these sources are reproduced in Table 3.1 for Class -I and Table 3.2 for Classes 0 and I. The observational data is also plotted in Figures 3.11, 3.12, 3.13, 3.14, and 3.15 for comparisons to our modeled data. The Boogert et al. (2015) data is a range of column densities collected from various literature sources so the dotted green lines are the maximum and minimum of the range and the solid line is the median value. Otherwise, each observational data point/line includes its respective error bar, plotted as a dotted line. The values of the error bars can be found in their referenced articles. Note that some observational data has small error bars. Each source is indicated by a different color in the plots. Some sources only have an upper limit error bar so there is only one dashed line above the solid observational data line. The Boogert et al. (2015) data sometimes also only has one dotted line and that is an upper limit. Horizontal lines are used for observational data from Boogert et al. (2015), IRS 2A, IRS 4A, HH 46 IRS, IRAS 17081-2721, as their visual extinctions are not defined. Therefore, their column density value is stretched across all time to compare with the model.

Absolute Column Densities of H_2O

As shown in the plot on the left side of Figure 3.11, ice formation increases as time progresses and the molecular cloud collapses. As the molecular cloud collapses and ice abundance increases, the visual extinction increases towards the inner part of the cloud (see Sec. 3.3). For Class -I, NIR38 and J110621 more closely align with the model data at a later time in the molecular cloud collapse, where their visual extinction values match in the model. Although the model data does not overlap within the error bars of the observational data in Figure 3.11, the data might align if the two sources have a higher visual extinction, which would move the data points to the right at a later time.

For Class 0, the absolute column density of H_2O matches the observational data for IRAS 2A earlier on in the model than HH 46 IRS. However, the model is within the bounds of all three observational comparisons. In Figure 3.11, The water ice falls as the center of the core warms up. In Class I, more ice is concentrated in the disk, so that the edge-on ice abundance grows as the disk grows. In the face-on case, ice column density falls as material is put into the disk and removed from the line of sight in the more polar directions.

When the model transitions to Class I, the inclination takes on a larger role in column density value. As mentioned above, the inclinations between 0 and 60 are not shown, due to their column densities closeness in value. After 60 degrees, the column density rises by at least an order of magnitude to 75 degrees, and then at least another order of magnitude to 90 degrees (edge-on). When referring back to Figure 3.4, the lines of sight for inclinations 60 to 90 go through the densest part of the disk, giving rise to a variance in column densities. The values from 0 to 60 degrees are outside the densest region of the disk and therefore, do vary greatly in their column density values.

Fractional Column Densities

In Figures 3.11, 3.12, 3.13, and 3.14, we present the column densities of all the species that have corresponding observational data from the literature. For completeness, we also have added glycolaldehyde, $CH_3(OH)CHO$, although there are no observational column densities for it from the sources we selected. It is included due to the fact that it is of observational interest and another isomer of $C_2H_4O_2$, and methyl formate and acetic acid are already included.

The sudden increase in absolute column density values in Figure 3.11, especially for those between 60-90 degrees, occurs when a disk starts to form. In Figures 3.12, 3.13, and 3.14, the effect of growth of a disk is taken away because the values plotted are the fractional value of a specific species to water. Therefore, any deviation in column density due to inclination gives insight on the formation or destruction of that specific species.

In Figure 3.12, the fractional column density of CO with respect to water for the edge-on inclination of 90 degrees falls below the other inclinations' column densities. From Figure 3.11, we know that the H_2O column density is increasing over time, so the only way for the fractional abundance to drop is for CO column density to drop. When the disk starts to form at $t = 120,000$ years, there is a drastic increase in density of H_2O near the protostar, particularly when viewing from an edge-on inclination. However, a disk with such close proximity to the protostar will be more heavily heated and water ice will not be able to retain CO. Therefore, the CO is lost at the early stages of disk formation. Once the disk grows outwards from the protostar, ices are able to regain CO on their surface. This is why there is an uptick in fractional column density at $t = 140,000$ years. By the end of the model simulation, the CO

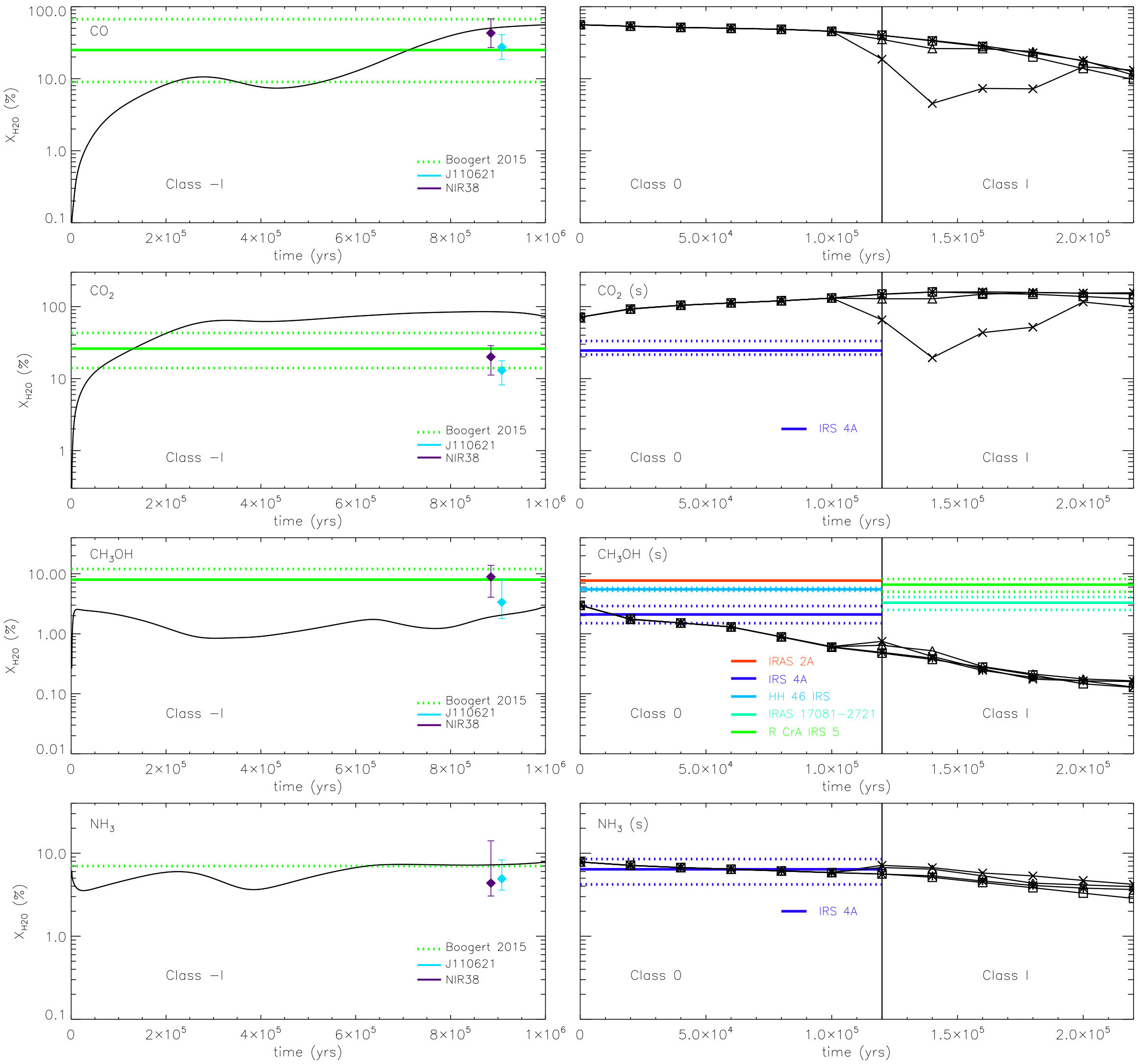

Figure 3.12 Stage 1 and 2 ice column densities with respect to water.

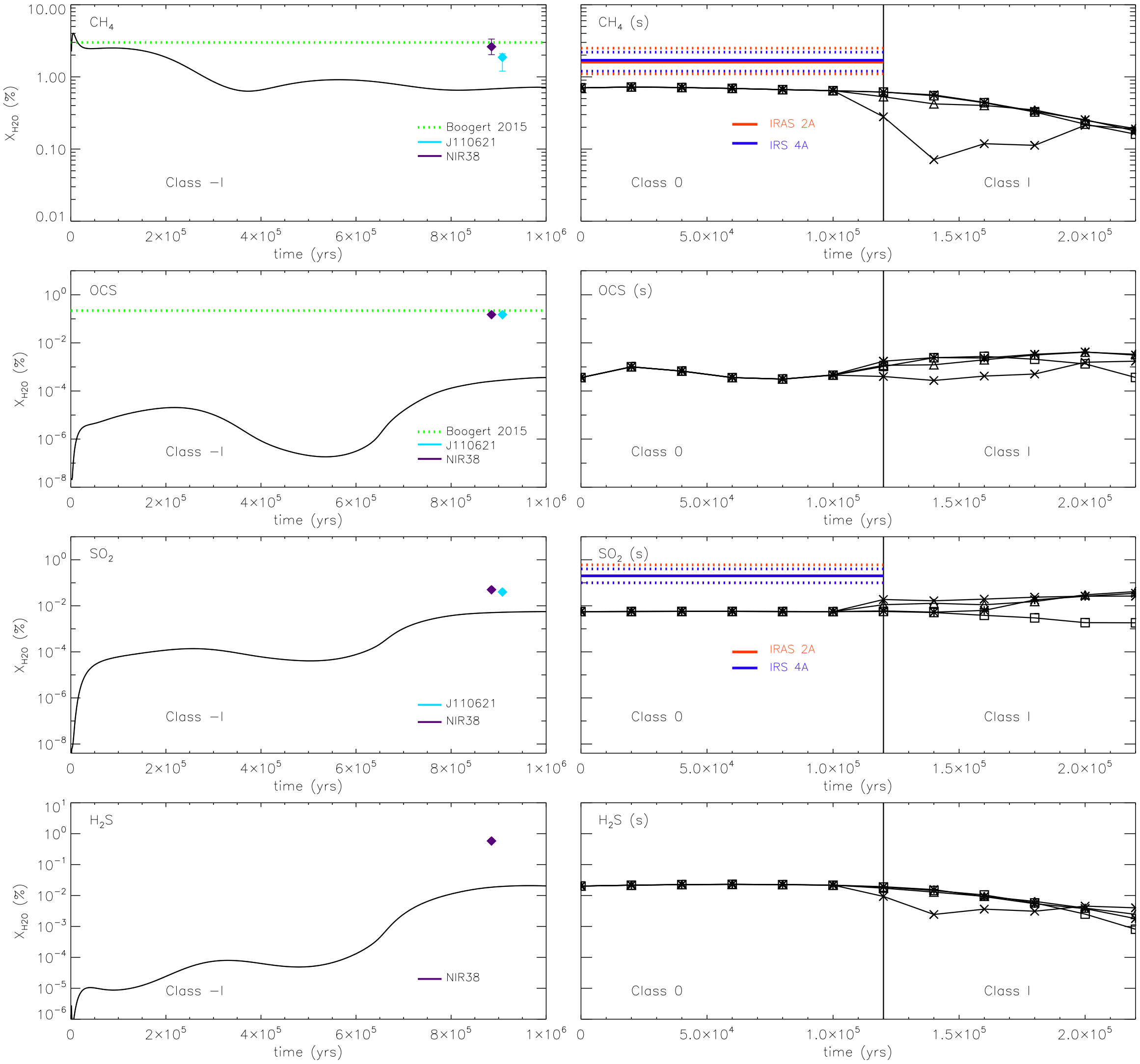

Figure 3.13 Stage 1 and 2 ice column densities with respect to water.

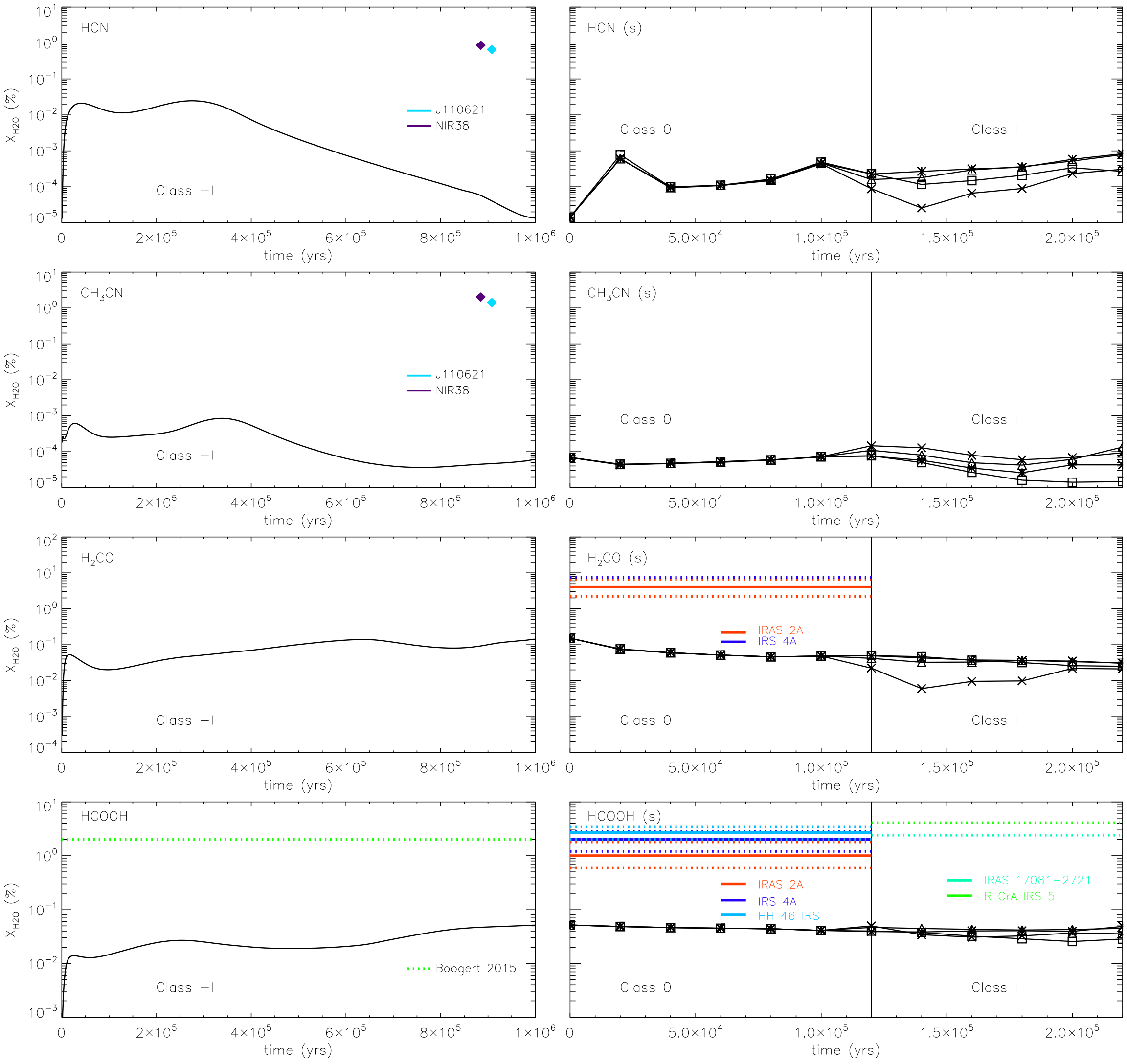

Figure 3.14 Stage 1 and 2 ice column densities with respect to water.

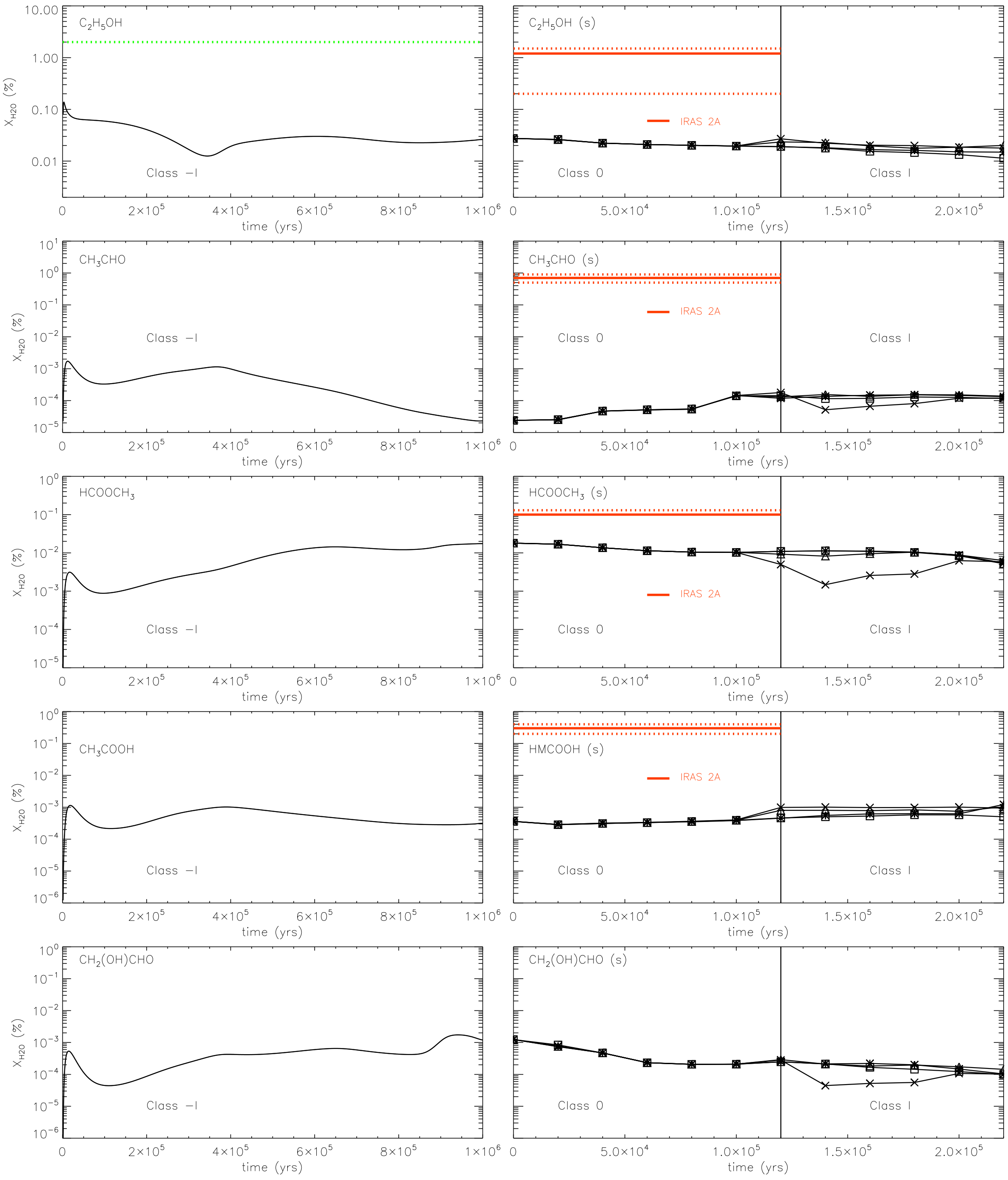

Figure 3.15 Stage 1 (Class -I) and 2 (Class 0 and I) fractional ice column densities with respect to water. Observational comparisons for each stage are the same as in Figure 3.11.
]

is able to regain is original column density and converges with the other inclinations' column density values.

This decrease in fractional abundance as the disk starts to grow occurs for other species as well and the effect is seen more drastically for CO_2 and CH_4, although other species such as H_2S, H_2CO, $HCOOCH_3$, and $CH_2(OH)CHO$ also show the trend in Figures 3.12, 3.13, and 3.14.

Another result to note is that the fractional column densities of CO, CH_3OH, NH_3, CH_4, and H_2S decrease as the disk evolves. At the end of stage 1, when the cloud has collapsed (see Figure 3.8), material on the outer edge of the cloud has a lower abundance than the inner part of the cloud. As the disk starts to form, the material from the outer part of the cloud will be added to the disk as the disk grows outward. When the material from the outer edge of the cloud joins the disk, these grains will have methanol at a lower abundance. Therefore, once these abundance values are now included in the column density calculation, the column density value will decrease over the remainder of Class I.

For CO column density values, there is only Class -I observational data to compare against. The model's column density values for all three sources falls within the range of the Boogert et al. (2015) data and fits within the error bars of the NIR38 data with the J110621 data not far off from the model.

For stage 1, the CH_3OH column density does fall within the error bar of J110621 and does not deviate more than an order of magnitude. For stage 2, the model intersects with the IRA 4A data during Class 0 but then continues to decrease through Class I and falls further away from observations of IRAS 17081 and R CrA IRS 5. In general, for the rest of the species, our model underproduces carbon-based species. If the initial carbon abundance is too low, subsequently, COMs will be underproduced as well.

However, our model's predictions for NH_3 align well with the Class -I, 0, and I observational data. Our model is within the error bars of both NIR38 and J110621 and under the upper limit from Boogert et al. (2015). For stage 2, the entirety of the model data for Class 0 falls within the error bars for IRS 4A.

The sulfur-bearing molecules, OCS, SO_2, and H_2S, are underproduced in our models. The initial abundance of sulfur in our model is based on past treatments in which this value was fine-tuned in order to have the correct abundance in the gas-phase for SO and SO_2, which are commonly observed gas-phase species in hot cores. This stems from a current general lack of knowledge surrounding sulfur chemistry in dense clouds. In dense regions, the sulfur budget does not add up to what has been observed in diffuse cloud regions, meaning that the sulfur is taking on an unknown form. It is unclear as to how much sulfur is in the gas or in the mantle in dense regions. In order for our gas-phase abundances of sulfur to match with observations, the sulfur on the ice had to be decreased, which helps us with matching observations in the gas-phase but leaves not enough sulfur on the grain. Therefore, it is expected that our models are underproducing sulfur-bearing species on the grain. In the gas-phase, sulfur is observed to be on the order of $10^{-}5$. In our models, we set the initial elemental sulfur at 8×10^{-8} and if the sulfur was increased 1-3 magnitudes higher in the model, then the ice abundances could match with observations, although this would result in us fine-tuning the ice but then skewing the gas-phase.

3.5 Discussion

The goal of this project is to gain insight on the physical and chemical processes from the prestellar collapse to the formation of a protostellar disk. The multidimensional nature of the hydrodynamical chemical model allows insight to the spatial effects on simple and COM species throughout the cloud and disk. By running the model from

Class -I through Class I, the model is able to trace the physical and chemical changes of ice species over time. The inclusion of inclination in the models allows for analysis of what column densities are obtained for various viewing angles. Analysis of the model's predictions with observational data gives insight as to how well our model behaves and what alterations may be needed.

3.5.1 Spatial Effects

As a 2D coupled hydrodynamical and chemical model, there are spatial effects on both the physics and chemistry. As discussed in Section 3.4.1, the physical conditions vary over space and as a result affect the chemical abundances. In Figures 3.7 and 3.8, chemical species abundances vary with the radius. External UV radiation decreases COM abundance on the outer edge of the cloud. As the cloud collapses, the increasing density encourages ice production toward the inner cloud. However, an interesting result is that towards the outer edge of the cloud, there is a location in which the abundances of species HCN, CH_3CN, HNCO, and OCS increases dramatically as a large "hump", indicating conditions favorable to ice production. These conditions have a visual extinction that is not too transparent to allow too much UV radiation that destroys molecules but not too opaque to slow ice production. Other molecules do not experience this effect due to their higher hydrogenation barrier.

A notable physical, spatial effect relates the forces that act upon the trajectories and move them through the disk structure in Class I. In Figure 3.6, the effect of meridonial circulation is demonstrated, showing how a trajectory is pushed through the midplane and out and around the outer disk as it meets the sharp contrast in density structure. Therefore, this gives evidence that grain particles experience movement throughout the disk and the material is cycled.

Another physical-related effect on the spatial map of molecules is the temperature a trajectory experiences. Specific trajectories get close enough to the protostar before being pushed back through the midplane, resulting in higher temperatures enough to desorb certain molecules as discussed in Section 3.4.3 and shown in Figure 3.9. The higher temperatures result in low-abundance pockets in the spatial abundance maps for COMs and simple, more volatile species. However, this effect occurred only for species that had a low enough binding energy that the high temperatures were enough to desorb them. Otherwise, molecules with higher binding energies were able to reaccrete onto the grain surface.

Alternatively, it can also be viewed that there is a pathway for the protection of species from the high temperatures and the species can survive at higher abundances in the outer disk. If the trajectories are able to not get too close to the protostar, and then are pushed through the midplane where temperatures are lower (see Figure 3.5), they are able to be preserved. This is a potential explanation of how species are preserved into Class II and eventually incorporated into comets.

3.5.2 Temporal Effects

Our coupled hydrodynamical and chemical model is able to trace chemistry from the pre-stellar collapse through the formation of a disk. Figures 3.7 and 3.8 both show not only how the abundance of simple species and COMs change over time but also that generally they are increasing over time. Figures 3.11, 3.12, 3.13, 3.14, and 3.15 demonstrate that most simple ice species and COMs are formed in the pre-stellar phase.

The species' abundances stay consistent throughout Class 0. Once inclination angles start to have an effect on column densities (discussed below), we see variation in column densities as time progresses. In Figure 3.11, the column density of water increases over time as the disk grows. In any plots of the fractional column densities with respect to water in Figures 3.12, 3.13, 3.14, and 3.15 that have a dip in column density is due to trajectories with lower abundances from the outer envelope joining the disk (see Section 3.4.4).

3.5.3 Inclination Angle Effect

Another goal of this project is to examine the effect that the inclination angle, or viewing angle, has on the column densities of various species. In Figure 3.11, the effect of inclination does not affect the column density values until Class I when the protostellar disk starts to form. At the first snapshot time for Class I (denoted by the vertical line in Figure 3.11) there is a large deviation of the absolute column density of water of about 2 orders of magnitude for face-on inclination vs an edge-on inclination. By the last snapshot time in Class I, the deviation between face-on and edge-on is about 3 orders of magnitude.

The largest jump in column density occurs for inclinations 60-90 degrees, with 90 degrees being the edge-on viewing angle. When comparing to Figure 3.4, these angles correspond to the densest part of the protostellar disk. As discussed in Section 3.4.4, anything below 60 degrees has a small variation in column density compared to face-on, with the variation between 60 and 0 degrees being only about half of an order of magnitude. This result indicates that in general, the column densities obtained from observations will be very sensitive to the inclination angle of a source and it should be expected that there will be variation of obtained column density values if observing sources that have inclination angles between 60-90 degrees.

The CORINOS project led by Yao-Lun Yang (Yang et al., 2022; Salyk et al., 2024; Okoda et al., 2025) has a project focus on determining any parameters that contribute to a source being considered COM-rich or COM-poor. The project considers four sources. Two COM-rich sources are B335 and L483 and the two COM-poor sources are IRAS 15398 and Ser-emb 7. The Corinos project also groups these sources into high and low luminosity sources, with B335 and IRAS 15398 having low-luminosities and L483 and Ser-emb 7 having high luminosities. Although this current project here does not consider luminosity effects, our results may shed light to the effect of inclination on whether a source is observed COM-rich or COM-poor with respect to ice column densities. The current inclination values obtained from radiative transfer calculations for each source are as follows: 87 degrees for B335 (Stutz et al., 2008), 70 degrees for L483, 69.4 for IRAS 15398, and 25 degrees for Ser-emb 7. For IRAS 15398, Vazzano et al. (2021), gives an estimate of 66 ± 14 degrees for the inclination. As discussed here, a variation of 14 degrees giving a max of 80 degrees or minimum of 52 degrees, can greatly affect the observed column density. Therefore, if IRAS 15398 errs on the lower end of the inclination range towards the low to mid-50 degrees, it may indeed be observed to be COM poor along with Ser-emb 7. This discussion points to the fact that there is a potential of a lot of variability in observations of hot corino sources and only sources of very similar inclinations can properly be compared to one another.

3.5.4 Comparisons to Observational Data

In Section 3.4.4, the model's calculated column densities are compared to observational values. These comparisons gives valuable insight to whether there is agreement between the model predictions and observations. Observational values are difficult to fit as they are based on compiled multiple molecules on top of each other. Therefore, caution must be taken as neither model or observations are inerrable.

However, given the observational data at hand, the comparisons between observations and model predictions tells us that overall our model needs more grain production since our column densities are generally low in Figures 3.12, 3.13, 3.14, and 3.15.

These column densities depend on the inputed elemental abundances at the start of stage 1 in the model. The results of Section 3.4.4 show that our models have too little carbon, which as a result, lowers the column densities of all carbon-species. Future implementation in the model could include running tests on the C/O ratio and seeing what ratio leads to better alignment with observations.

In addition to varying the C/O ratio, we can vary the initial visual extinction. The model presented here has an initial visual extinction of 1 mag at the outer radius. With a higher initial visual extinction set in Stage 1, the dust temperatures would not reach high temperatures so quickly as they do currently. With a delay in temperature increase, the conversion of CO to CO_2 will slow down, which would reduce the amount of carbon and oxygen being locked up into CO_2 (see Figure 3.12). In theory, less carbon and oxygen locked up in CO_2 would then allow higher abundances of COMS.

Sulfur species, OCS, SO_2, and H_2S, are underproduced as expected. Sulfur has been detected in diffuse regions in the gas-phase. In dense regions, the sulfur budget does not add up, meaning that it is unknown what form the sulfur is in. When observing hot cores, the amount in the gas-phase still does not add up even when after all the time has evolved, it is suspected that molecules would have desorbed off the grain. After adding together the sulfur bearing species, it still does not meet the sulfur budget from a diffuse cloud. In the models, we reduce sulfur budget down to get the correct abundance in the gas. However, this leaves us with not enough on the grain surface. We need another mechanism to meet observational data predictions of ice but also meet gas-phase sulfur.

In the gas-phase, sulfur is observed to be on the order of 10^-5. In our models, we set the initial elemental sulfur at 8×10^{-8} and if the sulfur was increased 1-3 magnitudes higher in the model, then the ice abundances could match with observations, although this would result in us fine-tuning the ice but then skewing the gas-phase.

3.6 Conclusions

We have presented a 2D coupled hydrodynamical and chemical model for a hot corino that traces the evolution of chemistry from the pre-stellar collapse through the formation of a disk. The radiation hydrodynamical model simulates the evolving density, temperature, and velocity structure of YSO Class -I into Class I. These values are fed into our chemical model, MAGICKAL, that are then run in post-processing to simulate the chemical evolution of each trajectory. MAGICKAL is a three-phase chemical kinetics model that simulates the gas, gas-grain, and mantle-ice chemistry. In this current project, we focus on the ice chemistry results and compare our results with recent JWST observations and other literature. Analysis of gas-phase chemistry is forthcoming in another paper.

The traced infall of trajectories and their movement through the disk has given better insight as to how the dynamics affects the chemistry. In the hydrodynamical results, we found evidence of meridonial circulation in the disk. This meridonial circulation allows the cycling of material throughout the protostellar disk and has a unique role in the spatial coverage of species. In Section 3.4.3, we discuss that trajectories that have a close approach to the forming protostar experience high enough temperatures that desorbs species from the grains surface. This close approach leaves these trajectories with lower ice abundances on the grain surface and as the motion of material throughout the disk pushes these trajectories out, they experience meridonial circulation and are pulled into low abundance pockets in the outer rim of the disk. This effect is amplified as time progresses in Class I.

In addition to the mechanism that cycles grains with low-abundances of select species, there is also movement of grains that are able to escape the harsh, higher temperatures near the protostar and are able to make their way through the motion of material within the disk with their high abundances of species still stable on the grain surface. In this case, the trajectories that keep stable abundances can be considered more pristine and may have a future role in conservation of COM material into comets.

This project also considered spatial maps for various species for all three YSO stages (Class -I, 0, and I). In the pre-stellar stage, the abundances are symmetrical around the cloud but vary with radius. In Section 3.4.2, we find that ice abundances are generally higher toward the inner cloud than the outer cloud due to the increasing density and COM production. However, for some species, such as HCN, CH_3CN, HNCO, and OCS, there is a peak toward the outer edge of the cloud where the conditions are optimal for ice production. In the spatial maps of Class 0 and I, the low-abundance effect was observed as discussed above.

Column densities were calculated for Class -I, 0, and I and compared to observational JWST and Spitzer data (McClure et al., 2023; Rocha et al., 2024, 2025; Boogert et al., 2008, 2015). These comparisons showed agreement for some simple species such as CO, CH_3OH, and NH_3, but overall the models are underproducing.

A research question of interest in this project was whether the inclination has a role in whether a source is observed COM-rich or COM-poor. Our model shows that for inclinations between 60-90 degrees, the column density values can vary greatly. Below 60 degrees the column densities only varied less than an order of magnitude.

We summarize the main conclusions of this modeling study below:

(i) Simple species and COMs are formed in the cold, pre-stellar stage, supporting the idea of early grain-surface production of COMs.

(ii) Pre-stellar disk has a ideal location towards the outer radius to avoid high visual extinction but not too low a visual extinction that UV photolysis overpowers and there is a unique response in chemistry for some species.

(iii) Meridonial circulation plays a role in the cycling of material throughout the disk.

(iv) As material accretes onto star, trajectories that get near protostar but do not fall in, experience high temperatures that desorb ices and leave them with low-abundances for certain species.

(v) Trajectories with low-abundances from the close encounter to the protostar are moved along the midplane and to the outer rim of disk by the effect of meridonial circulation, creating "low-abundance" pockets.

(vi) Trajectories that do not get as near the protostar during accretion are able to survive with stable abundances, which is potentially a pathway that allows COMs to survive in the future incorporation into comets.

(vii) Our models are generally underproducing grain chemistry, specifically for carbon-bearing species.

(viii) A higher initial visual extinction in the models could improve the COM column densities.

(ix) Our model's low predictions of sulfur in the grain allude to the ambiguity surrounding sulfur-chemistry given that the model's initial sulfur abundance is fine-tuned to result in the observed gas-phase sulfur column densities.

(x) Inclination angles between 60-90 degrees vary over three orders of magnitude and could have an impact on whether a source is observed to be COM-rich or COM-poor.

(xi) Inclination angles below 60 degrees do not have a large variation in column density values as they are outside the main density structure of the disk.

3.7 Chapter Acknowledgements

This work was funded by the National Science Foundation through the Astronomy & Astrophysics program (grant number 2206516).

CHAPTER 4

MODELING GAS AND ICE COLUMN DENSITIES OF COM-VARIABLE CORINOS SOURCES B335, L483, IRAS 15398, AND SER-EMB 7

"Run fast for your mother, run fast for your father. Run for your children, for your sisters and brothers. Leave all your love and your longing behind. You can't carry it with you if you want to survive. The dog days are over, the dog days are done. Can you hear the horses? 'Cause here they come."

Florence + The Machine, *Dog Days Are Over*

4.1 ABSTRACT

The formation of complex organic molecules (COMs) in star-forming regions is largely driven by grain-surface chemistry, yet observational constraints have historically focused on the gas phase. With ALMA, COMs have been widely detected in low-mass protostars, but variations in their abundances raise questions about underlying chemical and physical processes. The launch of the James Webb Space Telescope provides unprecedented access to solid-phase chemistry, complementing gas-phase data and allowing for a more complete understanding of molecular evolution. This study examines four Class 0 protostars from the CORINOS project - B335 and L483 (COM-rich) and IRAS 15398 and Ser-emb 7 (COM-poor) - to investigate whether COM variability arises from chemical evolution, physical conditions, or observational effects. Using a coupled radiation hydrodynamical and chemical model with a RADMC-3D pipeline, I simulate the chemistry from cloud collapse to protostellar disk formation and compare modeled gas-phase CH_3OH column densities with ALMA observations. Ser-emb 7, a COM-poor source with a low inclination (25 degrees), exhibits significantly lower modeled column densities, indicating that the viewing angle may influence its classification as COM-poor. Ice-phase column densities appear less sensitive to inclination during Class 0, highlighting a potential different dependency on inclination.

4.2 INTRODUCTION

It is now generally accepted that the formation of most complex organic molecules (COMs) in star-forming regions has a significant, and in some cases dominant, contribution from grain surface chemistry, rather than solely through gas-phase chemistry. With telescopes like the Atacama Large Millimeter Array (ALMA), many species and COMs have been detected in the gas-phase around high-mass and low-mass star-forming cores. Chemical modeling efforts that describe the reaction pathways have used the gas-phase observational data as a benchmark to the accuracy of the calculations. However, as is now generally accepted, we are missing half of the data if we are only comparing to gas-phase. Although telescopes such as the Spitzer Space Telescope have given us insight into the solid-phase through infrared observations, these telescopes lacked the spectral resolution and sensitivity comparable to gas-phase observations. With the launch of the James Webb Space Telescope (JWST), the solid-phase chemistry of star-forming cores can be resolved like never before. JWST ice observational data coming from McClure et al. (2023); Rocha et al. (2024, 2025) and Kim et al. (in prep), help prove furthermore that gas-phase chemistry is not solely responsible for what we observe and that grain-chemistry is needed for a complete picture.

Of particular interest is the solid- and gas-phase chemistry occuring in low-mass hot cores, called hot corinos. Hot corinos are representative of solar-type star formation and are classified through the Young Stellar Object (YSO) classification scheme, going through a cloud collapse (Class -I) and protostar and protostellar disk formation (Classes 0 and I). Gaining access to ice data in addition to the gas-phase data contributes to a more complete picture of the chemistry occuring in hot corinos. By extension, these observations will allow us a better understanding how the chemistry evolves and impacts the early formation of our solar system.

Although ALMA has been successful detecting COMs in hot corinos, not all embedded protostars have been found to exhibit a rich spectra of COMs. In the ALMA surveys by Belloche, A. et al. (2020) and Yang et al. (2021), only about half of the samples had COM detection. This begs the question as to whether this is due to a chemical or physical cause. If a chemical cause, then it is suspected that the gas-grain chemistry evolved differently in the COM-poor sources. If physical, the sources could have been subject to conditions that affect their COM abundances due to inefficient desorption, high dust opacity, luminosity outbursts, etc. Alternatively, observational effects could affect whether a source is considered COM-rich or COM-poor such as the viewing angle towards the source, whether the source is edge-on, face-on, or somewhere in between.

As part of the CORINOS project (Yang et al., 2022; Salyk et al., 2024; Okoda et al., 2025), four sources are considered in effort to investigate the cause behind COM-rich and COM-poor sources. Two sources, B335 and L483, are considered COM-rich in the gas-phase and sources IRAS 15398 and Ser-emb 7 are considered COM-poor. B335 has been studied by Imai et al. (2016, 2019); Okoda et al. (2024) and Lee et al. (2024), L483 by Oya et al. (2017); Jacobsen, Steffen K. et al. (2019) and Agúndez, M. et al. (2019), IRAS 15398 by Okoda et al. (2023), and Ser-emb 7 by Bergner et al. (2019) through ALMA observations. Ice-data exists for both B335 and L483 from Chu et al. (2020). IRAS 15398 ice-data have been obtained by Kim et al. (in prep), Boogert et al. (2008); Pontoppidan et al. (2008), and Öberg et al. (2008). There is currently no published ice data for Ser-emb 7.

For this project, I use a coupled radiation hydrodynamical and chemical model that simulates the evolution of chemistry from cloud collapse through formation of a protostellar disk. The preliminary paper by Shope et al. (in prep) describes the model in detail and presents comparisons with JWST and Spitzer data. Here, we use the RHD/chemical model to compare model column densities with the existing literature values - both gas-phase and ice - for the four CORINOS sources. To make proper gas-phase comparisons with observational data, we use the radiative transfer software, RADMC-3D (Dullemond et al., 2012), to calculate column densities and excitation temperatures that take dust attenuation into account. This treatment has been developed my Bonfand et al. (in prep).

Through comparisons of gas- and solid-phase column densities with our coupled chemical and hydrodynamical model, we investigate the following questions: 1) Is chemical complexity rooted in ices? 2) How do the gas- and solid-phase results benchmark our current chemical model? and 3) Does the viewing angle play a role in observed column densities?

As the process of obtaining gas-phase column densities is more involved, due to the need of radiative transfer calculations, this current project specifically focuses on modeled gas-phase column density of CH_3OH to observed gas-phase column density values across the four sources. Future projects will consider more species such as ethanol (C_2H_5OH), acetaldehyde (CH_3CHO), and methyl formate ($HCOOCH_3$). Concerning ice column densities, these values were readily available from the preliminary paper by Shope et al. (in prep). Therefore, existing ice column densities from literature are compared to our existing calculations of ice column densities for various simple species and COMs.

4.3 METHODS

The simulations are carried out with *ATHENA++* for the radiation hydrodynamics (RHD) and *MAGICKAL* for the chemical modeling. The RHD model is run first, with chemical modeling done in post-processing. An overview of the modeling approach is described in Shope et al. (in prep).

Gas-phase column densitites and excitation temperatures are calculated with use of an in-house RHD/chemical model to RADMC-3D pipeline. RADMC-3D is a package that allows users to conduct radiative transfer calculations to generate 2D synthetic images of their data in order to compare to observations. The pipeline streamlines the generation and analysis of synthetic data from our combined hydrodynamical and chemical models. It automates the workflow by: (1) reading the outputs of the dynamico-chemical simulations and formatting them for compatibility with the publicly available radiative transfer code RADMC-3D, (2) retrieving spectroscopic data from SPLATALOG for selected molecules, (3) performing radiative transfer calculations with RADMC-3D, (4) post-processing the resulting 3D datacubes to account for observational effects, such as beam convolution and continuum subtraction, and (5) extracting synthetic spectra at different positions to generate population diagrams, enabling the determination of column densities and excitation temperatures. This treatment is used for the gas-phase column densities reported in this paper. Refer to Bonfand et al. 2025 (in prep) for more details.

All ice column densities are calculated by integrating the abundances over the line of sight, in the same manner as Shope et al. (in prep).

Our models are compared to current gas- and solid-phase column densities of the four CORINOS sources, B335 and IRAS 15398 both have lower luminosities and L483 and Ser-emb 7 have higher luminosities. B335 has been reported to have a solar luminosity of $0.72L_\odot$ by Evans et al. (2015), $1.6L_\odot$ by Okoda et al. (2022), and $1.36L_\odot$ by Evans et al. (2023). In Evans et al. (2023), the mass of the disk is reported as $0.063M_\odot$ and protostellar mass as $0.25M_\odot$. The inclination of B335 is reported to be 87 degrees (Stutz et al., 2008). For L483, literature values are $13L_\odot$ ((Shirley et al., 2000; Jacobsen, Steffen K. et al., 2019)), $4.4M_\odot$ Jørgensen, J. K. (2004) for envelope mass. Radiative transfer calculations from the CORINOS team has the inclination value at 70 degrees. For IRAS 15398, the literature values are $1.8L_\odot$ (Jørgensen et al., 2013) and $1.8L_\odot$ (Okoda et al., 2023) for luminosity and $1.2M_\odot$ for envelope mass (Jørgensen et al., 2013). Concerning the inclination of IRAS 15398, Vazzano et al. (2021) reports a value of 66±14 degrees, but the CORINOS team radiative transfer calculations has it at 69.4 degrees. Lastly, for Ser-emb 7, the luminosity is reported as $7.9L_\odot$ and envelope mass as $4.3M_\odot$ (Enoch et al., 2011). The CORINOS team radiative transfer calculations have the inclination of Ser-emb 7 as 25 degrees.

The pipeline framework has options to select the beam size and inclination for the creation of the synthetic data. In accordance with the beam sizes from literature, I chose an average beam size of 70 AU for B335 in efforts to best match the beam size from Lee et al. (2024), and beam sizes of 62 AU for L483 (Jacobsen, Steffen K. et al., 2019), 49 AU for IRAS 15398 (Okoda et al., 2023), and 242 AU for Ser-emb 7 (Bergner et al., 2019). The inclinations chosen for the pipeline are 87 degrees for B335 (Stutz et al., 2008), 70 for L483 (CORINOS RT), 69 for IRAS 15398 (CORINOS RT), and 25 for Ser-emb 7 (CORINOS RT).

In addition to the beam size and inclination, age of the hot corino sources must be taken into account. In Stage 2 of MAGICKAL, which corresponds to the YSO Classes 0 and I, the chemistry for each tracer particle is calculated throughout the simulation time or until it enters the inner boundary representing the protostar. Careful selection of the tracers is required to ensure good spatial coverage for the chemistry at any particular moment. A total of 12 evenly spaced "snapshot times" are chosen, and tracer particles selected, such that the instantaneous distribution of tracers provides good spatial coverage of the chemical results at those times (Shope et al. (in prep)). Therefore, since these four sources are considered Class 0 sources, we include column density values for all six Class 0 snapshot times along with one more snapshot time at the beginning of Class I.

Concerning other pipeline inputs, I used a velocity window of 20 km/s. The velocity window sets the full extent of the expected broadest emission line (i.e. 2×FWHM). The frequency margin value was set to 34 MHz, which ensured that the synthetic cubes/spectra had enough channels to fit the baseline. The minimum resolution of the output synthetic images was set to 5 pixels/beam. The spectral resolution of the output synthetic spectra was set to 0.5 km/s. The population diagrams were built for the (0.01, 0.0) x-y position. The frequency window was set to 10 MHz. The frequency window is the width of the window defined around a rest frequency of a given transition. The minimum frequency width considered is 1.5 MHz. This parameter excludes transitions that are closer than this value.

4.3.1 Population Diagrams

Part of the process of obtaining a column density from the pipeline entails creating a population diagram. The pipeline is run for seven times starting from $t = 0$ through $t = 120,000$ years with $20,000$ year increments. Each pipeline run outputs a population diagram along with an excitation temperature and column density. Lines for the population diagram are obtained through SPLATALOGUE and lines are included if their emission meets the emission threshold value, which I set to 1×10^{-5} mJy/beam in the input parameters.

Since there are four sources for comparisons and seven snapshot times, the pipeline generates 28 population diagrams, column densities, and excitation temperatures. Figure 4.1 shows four example population diagrams at $t = 100,000$ years, which is the last snapshot time of Class 0 before the transition into Class I. There are 28 population diagrams, but as they are all similar in appearance, only four examples are shown in Figure 4.1.

Part of the pipeline routine is to select the frequency range that SPLATALOGUE will search to obtain lines for the analysis. For this analysis, I chose a generalized frequency range of 340-360 GHz to efforts to include the same lines as in Lee et al. (2024). The list of transitions were pulled from the CDMS database. After analysis of each line, some lines either had transitions too close to one another or did not meet the threshold and did not make their way into the population diagram. There are a total of 26 lines in the analysis, although not all of them make their way into the

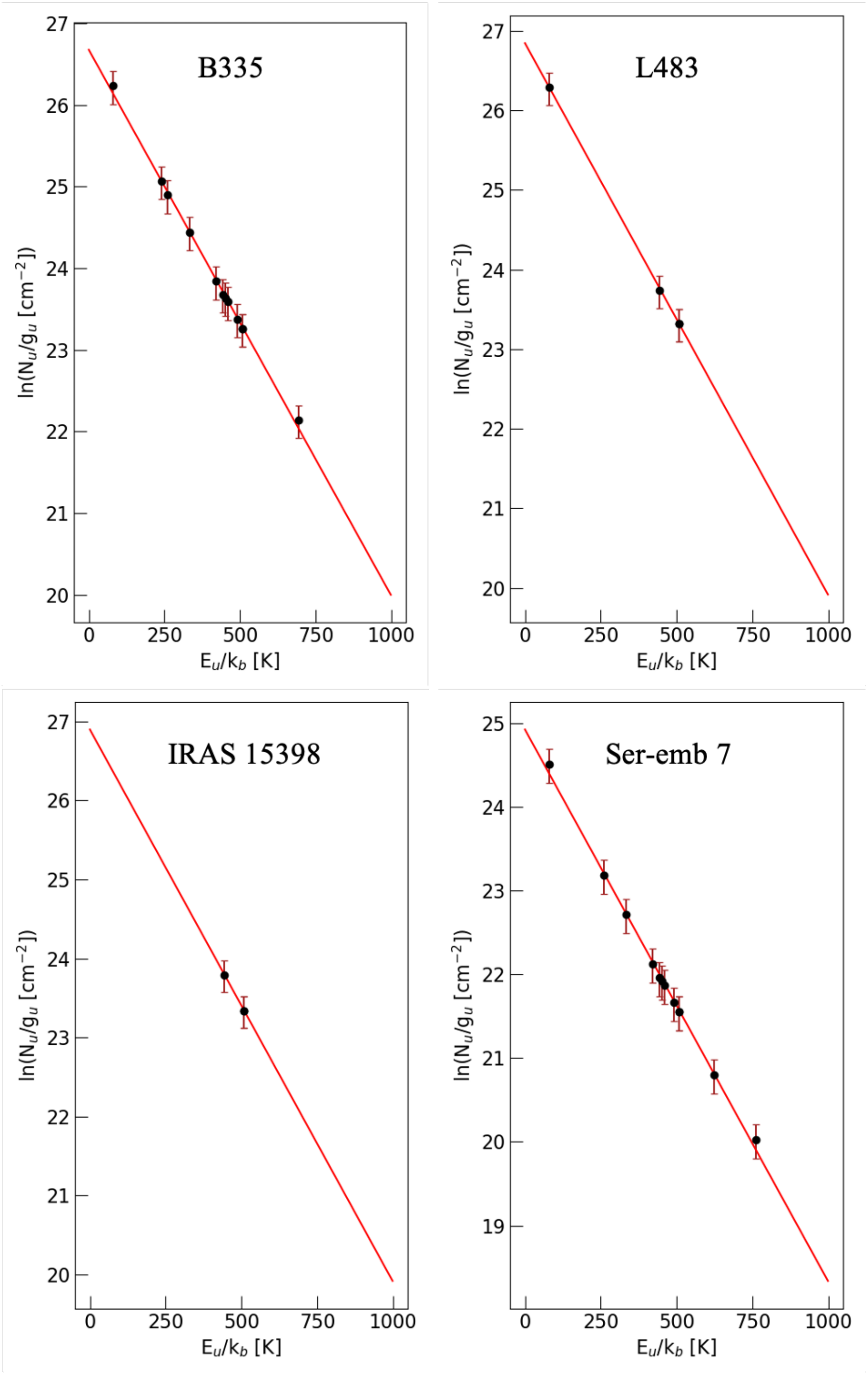

Figure 4.1 Population Diagrams for $t = 100,000$ years, the last snapshot time of Class 0.

population diagram. For each line, there may be one or multiple transitions. For all four synthetic calculations of the four sources, not all synthetic cubes have finished running at this time. Once all synthetic cubes have finished running, the population diagram analysis will be redone for a better constrained column density. Figure 4.1 shows the lines (that met the criteria to be included) that have currently finished for each synthetic calculation of a source.

4.4 Results

4.4.1 Gas-Phase Column Densities

In this paper, I specifically look at modeled gas-phase CH_3OH column densities in comparison to observational gas-phase values. In Table 4.1, I tabulate the column density values obtained from the pipeline for snapshot times $t = 0$ through $t = 120,000$ years in 20,000 year increments. The pipeline as described in Section 4.3, was altered to match observational parameters such as the frequency range, beam size, and viewing angle of the source. Therefore, the labels of "B335", "L483", "IRAS 15398", and "Ser-emb 7" refer to the synthetic column densities as obtained from RHD/chemical model + RADMC-3D pipeline. The pipeline was not able to generate a population diagram for $t = 0$ due to the abundances being below the threshold value. As mentioned in Section 4.3.1, not all synthetic cubes have finished running so in some cases, there are only two lines that were used for the linear fit of the population diagram. Therefore, some column densities do not have any errors associated with their value, since the goodness-of-fit R^2 value was 1. Once all cubes have finished running, these results will be updated.

Figure 4.2 plots the column densities from Table 4.1 in comparison to literature values of B335, L483, and IRAS 15398. There are currently no gas-phase observations

CH$_3$OH Column Density ($\times 10^{15}$ cm^{-2})				
Time (years)	B335	L483	IRAS 15398	Ser-emb 7
$t = 0$	-	-	-	-
$t = 20,000$	27.5±3.87	28.8±2.08	37.7	5.13±0.379
$t = 40,000$	19.3±0.906	21.2±0.0113	21.4±0.115	3.52±0.0903
$t = 60,000$	13.8±0.625	15.8±0.26	15.8±0.0103	2.25±0.168
$t = 80,000$	8.01±0.402	9.13±0.224	10.1±0.197	1.39±0.101
$t = 100,000$	3.74±0.154	4.15±0.0938	4.32	0.663±0.0313
$t = 120,000$	15.7±2.98	39.7±4.33	55.0	1.05±0.179

Table 4.1 Synthetic gas-phase column densities of CH$_3$OH. Column density values are obtained from the RADMC-3D code that reads MAGICKAL outputs and creates synthetic observations to properly account for dust emission and radiative transfer effects, allowing for a better comparison of model data to observations. The RADMC-3D code was altered for each source to match the source inclination and maximum beam size of the observations. For IRAS 15398 modeling, some snapshot times only have two lines, making the linear fit a perfect line with no error bars.

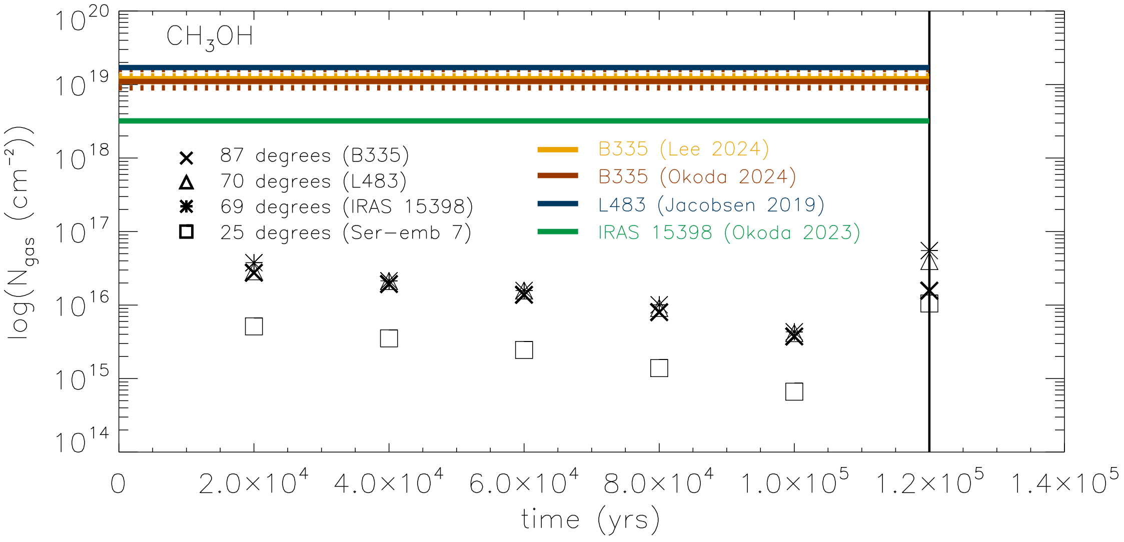

Figure 4.2 Gas-phase column densities of CH$_3$OH obtained from RADMC-3D pipeline compared to observations of CORINOS sources, B335, L483, and IRAS 15398. There are currently no gas-phase observations of methanol for Ser-emb 7. Black symbols correspond to the model results and the colored lines correspond to observations. The vertical black line shows the cutoff from Class 0 to Class I data, at $t = 120,000$ years.

done of Ser-emb 7. In this plot, the solid colorful horizontal lines are the literature values, with their uncertainty (if reported in the literature) as a dashed line in the same coordinating color. The black vertical line shows where the model switches from Class 0 to Class I. The switchover from Class 0 to Class I is where the protostellar mass becomes larger than the envelope mass. The technical switchover value is at $t = 134,610$ yr, which falls after the 7th ($t = 120,000$ yr) snapshot but before the 8th ($t = 140,000$ yr) snapshot time. For simplicity, we define the $t = 120,000$ yr snapshot as the end of the Class 0 stage.

The black symbols correspond to the synthetic column densities obtained from the pipeline. The X symbol corresponds to data for B335 conditions, the triangle for L483, the asterisk for IRAS 15398, and square for Ser-emb 7. These symbols also refer to their inclination values, 87, 70, 69, and 25, respectively. Each black symbol is placed at a snapshot time.

In this plot, the modeled column density values are systematically a few magnitudes below the observational data. The modeled data for the three sources B335, L483, and IRAS 15398, are all at similar values, as seen by their symbol placements that are overlaying on top of one another. However, there is a notable difference for the modeled Ser-emb 7 column densities. The Ser-emb 7 values are about a magnitude below the column densities of the other three sources.

4.4.2 Ice Column Densities

Another goal of this project is to compare modeled ice column densities to column densities obtained from observations of the four CORINOS sources. In Figure 4.3, the modeled column densities are in black, with symbols indictating different inclinations. Here I show inclinations of 90 degrees (edge-on) as an X symbol, 75 degrees as a triangle, 60 degrees as an asterisk, and 0 degrees (face-on) as a square. I selected

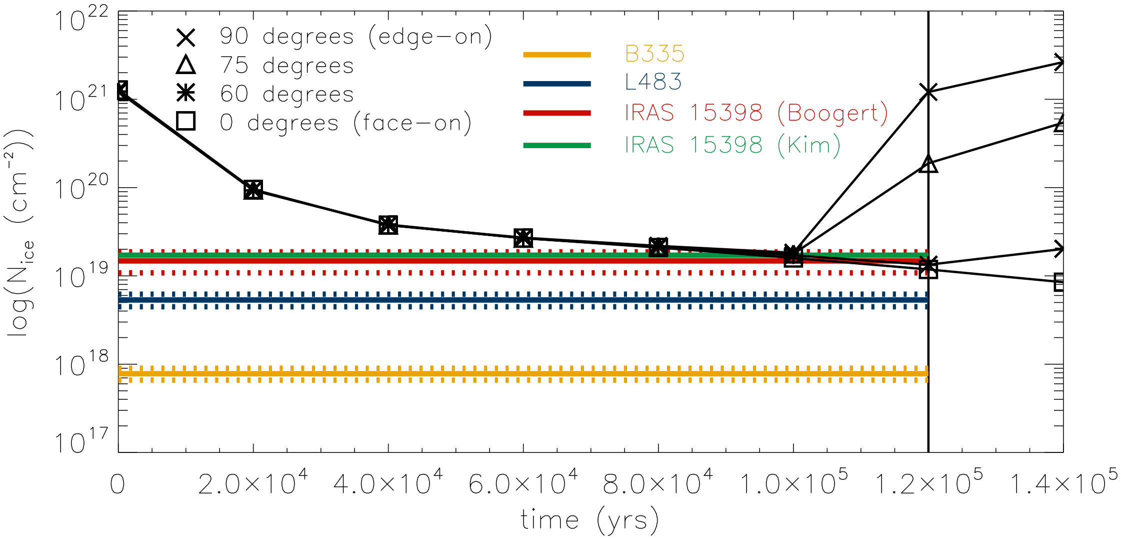

Figure 4.3 Ice column density of water. Modeled column densities are included for inclinations of 90 degrees (edge-on, X symbol), 75 degrees (triangle symbol), 60 degrees (asterisk symbol), and 0 degrees (face-on, square symbol). Observations for B335 and L483 come from Chu et al. (2020), and the two observations for IRAS 15398 come from Boogert et al. (2008) and Kim et al. (in prep). Vertical black line is the beginning of Class I. The solid colored lines are observational values. Dashed lines correspond to their respective reported uncertainties.

to show these inclinations rather than the exact inclinations for the four CORINOS sources, in order to show the full range of inclinations and their effect on the ice column densities.

As concluded in Shope et al. (in prep), inclination angles do not make a difference in the ice column densities until the model reaches Class I. In Figure 4.3, the modeled data matches the IRAS 15398 observational data towards the end of Class 0. As the model goes into Class I and a protostellar disk starts to form, the ice column density shoots up for sources that are edge-on. There is a large deviation in column densities for sources that are between 60-90 degrees. Below 60 degrees is outside of the main density structure of the protostellar disk. The model data only matches IRAS 15398 for inclinations ∼ 60 degrees or lower.

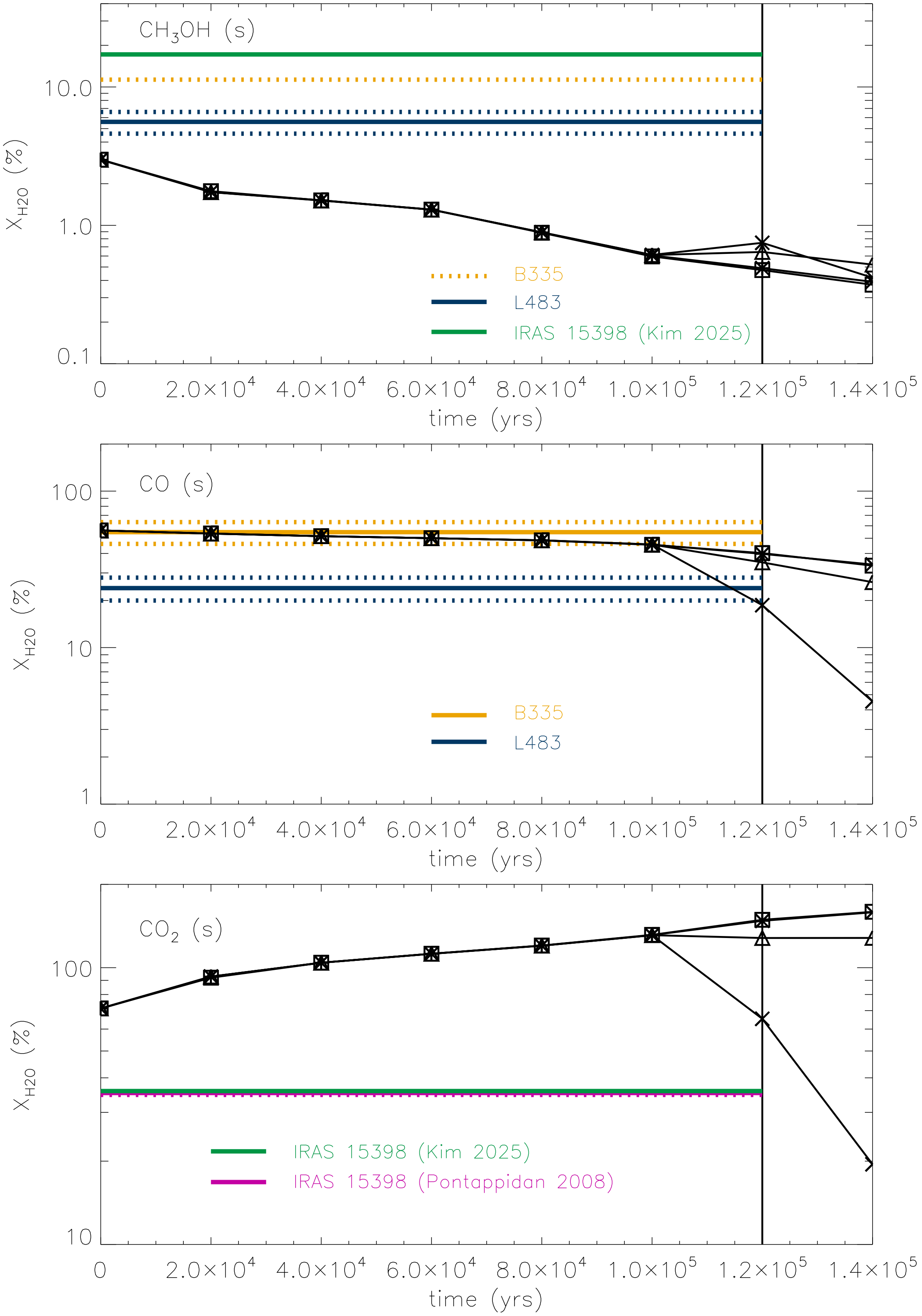

Figure 4.4 Column densities of other species with respect to water.

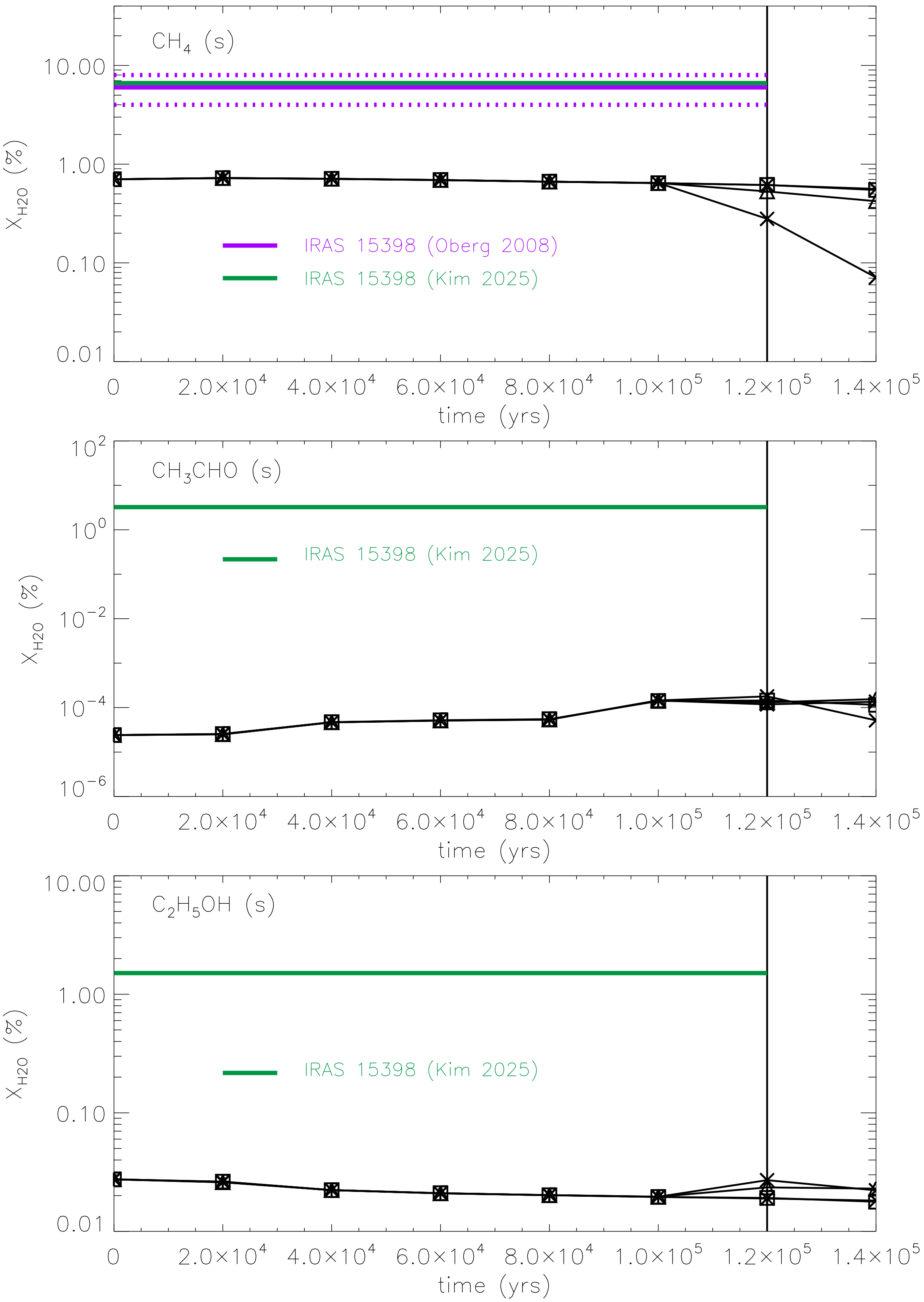

Figure 4.5 Column densities of other species with respect to water.

The remaining figures (Figures 4.4 and 4.5), show comparisons of ice column densities to existing observational column densities. The top plot in Figure 4.4 is of particular interest due to the gas-phase analysis in Section 4.4.1 of CH_3OH. In this plot of modeled CH_3OH ice column density, the modeled results show no effect of inclination on the column density results for Class 0. In this figure, the modeled methanol column density is underproduced.

For the remaining fractional column density plots, CO matches B335 observational data throughout Class 0. It matches L483 column density at the beginning of Class I for an edge-on value. A similar, and expected (see Chapter 3), result is the overproduction of CO_2 in the model when compared to observational column densities. For the remainder of the species, CH_4, CH_3CHO, and C_2H_5OH in Figure 4.5, the modeled column densities are systematically underproduced in comparison to observations.

4.5 Discussion

4.5.1 Benchmarking Current Model

With the launch of JWST, we now can have the sensitivity needed to make observations of COMs in the solid-phase on grains. In the past, the multitude of data coming from gas-phase observations (most notably from ALMA) have assisted in benchmarking chemical models. Now with new data coming in from JWST programs, along with existing Spitzer data, chemical models can now be benchmarked according to ice data as well. In this project, Figures 4.2, 4.4 (except for CO and CO_2, and 4.5, all indicate that the modeled column densities are much lower than observational data.

There could be a number of reasons for a low estimate of the column densities. First, as discussed in Chapter 3, carbon and oxygen are potentially being locked into CO_2, due to a low initial visual extinction and high dust temperatures early on in the model. A higher visual extinction could free up carbon and oxygen and could increase the column densities of COMs.

Second, the elemental budget of carbon could be too low. With too low of an elemental budget of carbon at the beginning of the model would then give too low of abundances for subsequent formation of carbon-bearing species. One way to test this is to run a grid of the RHD/chemical models with various C/O ratios and see the effect on the gas-phase and ice column densities.

Third, the masses and luminosities of the four CORINOS sources may contribute to their observed column densities. For our RHD/chemical model, during stage 2, the total luminosity reaches a maximum value of 25 $L_{\odot}$. The final stellar luminosity is just over 1 $L_{\odot}$, while the final stellar mass is $\sim 0.744 M_{\odot}$ at the end of the model (Shope et al. (in prep)). B335 and IRAS 15398 are both considered to be low-luminosity sources, with solar-type luminosities similar to the model setup. L483 and Ser-emb 7 both have higher luminosities. One way to test the effect of luminosity and mass on column densities is to run the coupled RHD and chemical model with a grid of varying luminosities and masses. Therefore, even though the current model does not line up with observational data, it might be that the difference in luminosities and masses compared to the model setup may contribute to the difference rather than an inaccuracy of the model network.

Fourth, the column densities obtained from the RADMC3D pipeline take dust attenuation into account. Currently, the lines have not been evaluated for optical thickness. A large dust opacity would lower the observed synthetic emission from that line and could ultimately lower the column density obtained from the population diagram. A future implementation of the RADMC-3D pipeline could evaluate the opacity of each emission line and let the user set an opacity threshold, such as a typically threshold of one (where anything above one is considered optically thick), to ensure that the analysis properly calculates the column density. Additionally, to test the effect of dust attenuation completely on the modeled gas-phase column density values, an integration of the gas-phase abundances from outer to inner radius from solely the MAGICKAL results would help give an indication as to the extent the dust opacity affected the pipeline's calculated column densities.

Lastly, this project has assumed that these sources are constrained within the Class 0 times, and it might be that this is too stringent. If these sources are more so in the Class I regime, the formation of a protostellar disk greatly increases both the gas-phase and ice column densities. Therefore, it could be that these sources are more evolved than considered here. In that case, our models might still align well with observations. Additionally, Class 0 sources might in reality have a disk, leading to higher column densities, even though the model presented here does not.

4.5.2 Effect of Viewing Angle

One of the scientific questions of this project is to investigate whether the viewing angle of the source contributes to the observed column densities - gas-phase and ice - of COM-poor and COM-rich sources. In congruence with the conclusions in Shope et al. (in prep), the inclination does not have an effect on the column densities in Class 0 but has a large effect for inclinations between 60-90 degrees in Class I (see Figures 4.3, 4.4, 4.5).

However, there is an evident dependency on inclination in Class 0 in Figure 4.2, where the modeled column densities of Ser-emb 7 is about a magnitude lower than the other sources. Ser-emb 7 is modeled to have an inclination of 25 degrees, whereas the others have inclinations of 87 degrees (B335), 70 degrees (L483), and 69 degrees (IRAS 15398). Ser-emb 7 is identified as a COM-poor source, so the low inclination angle (closer to face-on) may contribute to the low modeled column density. However, based on data from the ALMA survey by Belloche, A. et al. (2020), IRAS 15398 is also identified as a COM-poor source, but its column density is of similar value to the COM-rich sources in Figure 4.2. As mentioned in Section 4.3, inclination angle of IRAS 15398 has also been reported to be 66 ± 14 by Vazzano et al. (2021). According to this reported inclination value range, IRAS 15398 could have an inclination as low as 52 degrees. The ice results have shown that a column density value from 69 degrees to 52 degrees could potentially have a large deviation. A lower modeled inclination of 52 degrees for IRAS 15398 might shed light as to whether the viewing angle of IRAS 15398 and Ser-emb 7 is a cause for lower observed column densities. However, the gas-phase dependence on inclination might be different than ice dependence on inclination.

The fact that there is a difference in column density in Class 0 for Ser-emb 7 compared to the other three sources, and it has a low inclination of 25 degrees might point to the fact that there is indeed a different dependence on inclination for the gas-phase than the ice. It may be that there is some structure in the gas during Class 0 especially if the temperature is low except close to the protostar. The emission region will be wherever the temperature is $>\sim 120$ K, so there may be a substructure within that region that is the beginning of a disk.

Alternatively, Ser-emb 7 also is simulated in the RADMC3D pipeline with a much larger beam size than the other three sources, which could be the cause of variation in the obtained column density values. Ser-emb 7 is simulated with a beam size of 242 AU, and B335, L483, and IRAs 15398 which have beam sizes of 70 AU, 62 AU, and 49 AU, respectively.

4.5.3 Chemical Complexity

If Ser-emb 7 does have a lower column density due to its inclination angle, and possibly IRAS 15398 if its inclination is as low as the range reported by Vazzano et al. (2021), then this result points to a possible gas structure forming before the protostellar disk forms as seen in the density profile in Shope et al. (in prep). Therefore, since the results do not show a difference in ice column density due to inclination in Class 0, but do in the gas-phase, it appears that COM-poor sources might have lower gas-phase column densities due to physical effects such as inefficient desorption off grains, gas-phase destruction (due to physical effects such as high cosmic-ray ionization rate or luminosity outburts), or high dust opacities. Once the pipeline implements removal of lines with high dust opacities and I test the effect of the dust opacities on the column densities by solely integrating the gas-phase abundances without dust attenuation accounted for, I can better conclude the magnitude of dust opacity effects on gas-phase column densities.

4.5.4 Future Considerations

Once all of the synthetic cubes finishing running for CH_3OH, the column densities will be updated in Table 4.1. In addition to column densities for CH_3OH, running the pipeline for other species such as ethanol (C_2H_5OH), acetaldehyde (CH_3CHO), and methyl formate ($HCOOCH_3$) will give a more complete picture and help to narrow the conclusions of this project. Additionally, I am in the process of working with Yao-Lun Yang and Rachel Gross to obtain ice data comparisons for Ser-emb 7.

4.6 CONCLUSIONS

I present here gas-phase column densities of CH_3OH from the coupled radiation hydrodynamical and chemical model along with a RADMC-3D pipeline treatment to properly account for dust attentuation effects. These modeled column densities are compared to existing observations of CH_3OH column densities from the four CORINOS sources, B335, L483, IRAS 15398, and Ser-emb 7, with the first two sources identified as COM-rich sources, and the latter two identified as COM-poor sources. In addition to gas-phase column densities, I specifically compare existing modeled ice column densities (Shope et al. (in prep)) to existing literature values of ice column densities for the four CORINOS sources.

The results lead to the following conclusions:

1. COM-poor sources might have lower gas-phase column densities due to physical effects rather than a chemical cause.
2. The modeled column densities of Ser-emb 7 are about a magnitude lower than the modeled column densities of B335, L483, and IRAS 15398.
3. The lower modeled column density of Ser-emb 7 indicates that its low inclination angle of 25 degrees may be a cause for its identification as a COM-poor source.
4. The larger beam size used in observations and in the RADMC3D pipeline modeling for Ser-emb 7, might also be a cause for the variation in column density.
5. Ice column densities might follow a different dependence on inclination than gas-phase column densities.
6. There might be a gas-phase structure that forms before the protostellar disk forms in Class I.
7. Our current model is systematically underproducing column densities in comparison to observations except for H_2O, CO, and CO_2.

8. In comparison to the modeled column densities, CORINOS sources may be evolved past Class 0.

4.7 Chapter Acknowledgements

I want to thank Mélisse Bonfand for her work on the RADMC-3D pipeline and acknowledge all the time and energy put into creating a pipeline for our group to use together.

CHAPTER 5

CONCLUSIONS

"I think of what the world could be, a vision of the one I see. A million dreams is all it's gonna take."

The Greatest Showman, *A Million Dreams*

5.1 THESIS CONCLUSIONS

In this thesis, I investigate the physical and chemical environments of star-forming regions, both high-mass and low-mass cores. With the most recent version of the fully active three-phase astrochemical model, MAGICKAL (Garrod, 2013; Garrod et al., 2022), which includes the newly implemented non-diffusive mechanisms such as three-body reactions (Jin & Garrod, 2020), I create an expansive grid of models to test the effect of physical conditions on a hot core environment (Chapter 2). Expanding from this 0D chemical model, I present a 2D axisymmetric radiation hydrodynamical model coupled with the chemical model for ~3000 trajectory particles tracing the physical and chemical conditions of a hot corino from the pre-stellar collapse through protostellar disk formation (Chapter 3). Gas-phase and solid-phase results are then compared to four CORINOS (Yang et al., 2022; Salyk et al., 2024; Okoda et al., 2025) sources, B335, L483, IRAS 15398, and Ser-emb 7 to investigate the whether COM complexity is rooted in ice chemistry pathways. Alongside the 2D RHD/chemical model, a radiative transfer pipeline incorporating the RADMC3D software, was streamlined with our model to give proper gas-phase column densities (Chapter 4).

Chapter 2 uses the grid of varied parameter values of visual extinction, hydrogen number density, cosmic-ray ionization rate, and warm-up timescale to investigate the effect on the MF:GA ratio in hot cores. The results indicate that high gas densities and prolonged ice-mantle desorption lead to extreme MF:GA ratios, primarily due to GA destruction on grain surfaces by atomic hydrogen before it can desorb. These results help explain the bimodal MF:GA ratios observed in NGC 6334I and suggest that local physical conditions, such as circumstellar disk chemistry, may play a key role in complex organic molecule distributions.

Chapter 3 presents preliminary results of the coupled RHD/chemical model with a focus on ice chemistry. The models track ice chemistry evolution from pre-stellar collapse through disk formation, mapping the spatial distribution of simple species and COMs. I compare our calculated ice column densities to JWST and Spitzer observations across YSO stages. Results show that the viewing angle significantly affects observed column densities, particularly at edge-on inclinations. The chemical model underproduces carbon-bearing ice species, suggesting a higher abundance of these molecules than currently simulated. Additionally, meridional circulation in the disk influences chemical distributions, with some material exhibiting hot-core-like behavior. I identify pathways for molecular survival through the protostellar phase, where an accreting particle avoids too close of an approach to the hot protostar and in turn is able to retain abundances on the grain as it travels through the disk. This result provides insights into potential cometary composition and the molecular origins of planetary systems.

Chapter 4 implements a RADMC3D pipeline along with the coupled radiation hydrodynamical and chemical model in order to calculate gas-phase column densities that account for dust attenuation. This treatment is then applied to CH_3OH to calculate gas-phase column densities for comparison to observational column densities of the four CORINOS sources, B335, L483, IRAS 15398, and Ser-emb 7. Additionally, pre-existing calculated column densities from Chapter 3 are used to compare to existing observational column densities of various species for the four CORINOS sources. The results show that although the ice column densities show no variation in column densities for various inclinations in Class 0, the modeled gas-phase column density of CH_3OH does show variation with Ser-emb 7, a COM-poor source that has an inclination angle of 25 degrees. This might indicate that there is a gas-phase structure that is dependent on inclination in Class 0 before the protostellar disk starts to form.

Alternatively, the low column density result could be due to a beam size effect, given that Ser-emb 7 has a much higher beam size in observations and subsequently, in our RADMC3D pipeline setup. The gas-phase variability in COM abundances (COM-rich or COM-poor) might be due to physical effects (inefficient desorption, luminosity outbursts, other mechanisms for gas-phase destruction) rather than a chemical effect.

5.2 SCIENTIFIC QUESTIONS

The overarching scientific inquires presented in Section 1.7 are answered as follows:

1. **What hot core physical conditions yield a high MF:GA abundance ratio? And what chemical pathways yield this high ratio?** High gas density and prolonged ice desorption timescales contribute to the high MF:GA ratios observed in NGC 6334I MM2 according to the model. The key chemical mechanism is GA destruction on icy dust grain surfaces, where atomic H reacts with GA before it can desorb. Higher gas densities enhance this destructive process, while extended exposure to temperatures of ∼125–160 K allows GA to linger on grains and be selectively destroyed, unlike MF, which escapes immediately upon water ice desorption.

2. **How does the viewing angle affect the column densities during protostellar disk formation?** In Class 0, the inclination angles do not effect the ice column densities in the models. However, the gas-phase results show that there might be a gas-phase dependency on the inclination in Class 0, as shown in the modeled column density results for the COM-poor Ser-emb 7 source.

   For the class I stage, inclination angles between 60 and 90 degrees (edge-on) have ice column densities that vary over three orders of magnitude. Inclination angles greater than 60 degrees do not have a large variation in column density values as they are outside the main density structure of the disk. This variation leads to an impact on whether a source is COM-rich or COM-poor in the ice.

3. **What implications do the RHD/chemical model results have on the inheritance of COMs throughout the solar-type star formation process?** In general, we find that the COM-rich region of the protostar is within the inner 300 AU of the hot corino. The RHD/chemical model results show an effect of meridonial circulation, where trajectories are circulated out and away from the midplane and are circulated back towards the central protostar before being pushed back out again. This meridonial circulation allows for movement of material, some of which experiences hot-core like behavior due to their close approach to the protostar. Other trajectories, however, escape the meridonial circulation effects and preserve their COM abundances, presenting a possible pathway for COM preservation into future YSO stages or in comets.

APPENDIX A

ADDITIONAL INFORMATION FOR CHAPTER 2

A.1 COMPARISONS WITH IRAS 16293B AND SGR B2(N)

Following G22, we also compare our model results with observations of IRAS 16293B and Sgr B2(N2), using column density data from the PILS (Jørgensen et al., 2016) and EMoCA (Belloche et al., 2016) ALMA line surveys, respectively. The comparison conducted by G22 was based on chemical model results from only three model runs, using different warm-up timescales (*fast*, *medium* and *slow*). All other physical and chemical model parameters were fixed in the G22 model comparison. Abundances in the low-mass star-forming source IRAS 16293B were found to correspond more closely to the *fast* warm-up model, while abundances toward the high-mass source Sgr B2(N2) matched more closely with the *slow* model. With the larger model grid explored here, we seek to determine whether the warm-up trend holds, and what degree of degeneracy may apply when other parameters are considered.

A.1.1 Matching Parameter

When considering the column densities observed in the PILS and EMoCA surveys, the match parameter includes a selection of observed molecules, thus Eq. (2.1) includes multiple terms. For each term, given by Eq. (2.2), $R_{\mathrm{mod,i}}$ represents the ratio of the peak fractional abundance of molecule i versus that of methanol, while $R_{\mathrm{obs,i}}$ represents the observed column density ratio of the same two molecules.

The observed ratios are the same as those used by G22, which were provided in the review of Jørgensen et al. (2020); for IRAS 16293B, this included a total of 24 molecular column densities from the PILS survey, while for Sgr B2(N2) 19 values were available from the EMoCA survey. G22 compared their model values against the observational data for all of these species, although they did not calculate a matching parameter and instead judged the best-match model (out of three warm-up timescales) based on a qualitative judgement.

Here, in order to determine the best match model based on the matching parameter, we further exclude some species from the analysis for which the G22 chemical network is uncertain or likely incomplete, namely: acetone, $(CH_3)_2CO$; propanal, C_2H_5CHO; methyl isocyanate, CH_3NCO; methyl isocyanide, CH_3NC; acetamide, $CH_3C(O)NH_2$; and methyl mercaptan, CH_3SH (see G22 for a brief discussion of this issue). We also exclude cyanoacetylene, HC_3N, due to the fact that its abundance is not exclusively associated with the hot-core chemistry, meaning that a good match is more closely related to having a model with an accurate physical/spatial structure. Therefore, there are a total of 17 molecular column densities considered in the match parameter for the PILS survey (IRAS 19293B) and a total of 13 molecules column densities considered for the EMoCA survey (Sgr B2(N2)).

A.1.2 Results

The model that has the lowest m-value is deemed the best-match model over all of the parameter space, indicating which physical conditions may be most representative of these particular sources (in the context of using a single-point model to represent the entirety of each source). However, as there can be some flexibility in the conditions that still yield low match parameters, we present the top four best-match models for the PILS and EMoCA results, listed in Table A.1 along with each match parameter. Additionally the model that is the worst match to the data (has the highest match parameter value) is included in Table A.1 along with its match parameter for reference. Note that the match parameter for IRAS 16293B is naturally larger than that of Sgr B2(N2), due to the larger number of molecules in the matching procedure (17 versus 13).

For both sources, the best match models have CRIR values around the canonical value, with the best matches for EMoCA trending slightly lower. High CRIR values appear to provide a poor match. The gas densities of the best-match models are a little higher for the EMoCA matches. For both sources the worst-match model has the highest gas density value used in the model grid. Longest warm-up timescale (2×10^6 yr) is favored in all the best matches for the EMoCA data, while for PILS the warm-up timescale is somewhat lower (around 10^5 yr). This broadly agrees with the trend noted by G22 in their limited parameter space. All the best matches for each source have initial visual extinction of 3.

The individual m-values for each molecule in the best-match model for either source are plotted as bars in Fig. A.1. The red and blue bars are molecules considered in the match, while black bars are not considered, due to the difficulty involved in reproducing these species with the current chemical network, using a single-point

Table A.1 Four best match models for IRAS 16293B (PILS) and Sgr B2(N2) (EMoCA). Best models determined by lowest overall match parameters. Match parameter considers the selection of molecules listed in Figure A.1. Model that is the worst match to the data is also included along with its respective match parameter value for reference.

	m-value	$A_{\mathrm{v,init}}$ (mag)	n_{H} (cm^{-1})	ζ (s^{-1})	t_{wu} (yr)
PILS					
#1	1.33	3	2.00×10^{7}	4.11×10^{-17}	2.00×10^{5}
#2	1.40	3	2.00×10^{6}	4.11×10^{-17}	2.00×10^{5}
#3	1.44	3	6.32×10^{7}	1.30×10^{-16}	6.32×10^{4}
#4	1.47	3	2.00×10^{7}	4.11×10^{-17}	1.12×10^{5}
#756	10.92	2	2.00×10^{10}	4.11×10^{-16}	2.00×10^{6}
EMoCA					
#1	1.95	3	2.00×10^{8}	1.30×10^{-17}	2.00×10^{6}
#2	1.97	3	2.00×10^{9}	4.11×10^{-18}	2.00×10^{6}
#3	1.98	3	6.32×10^{7}	1.30×10^{-17}	2.00×10^{6}
#4	1.99	3	2.00×10^{8}	4.11×10^{-18}	2.00×10^{6}
#756	7.84	2	2.00×10^{10}	4.11×10^{-16}	2.00×10^{6}

model. Blue bars in the plot for Sgr B2(N2) represent upper limits for those molecules; bars falling below the zero-line therefore count as an exact match. The top four best match models show very similar peak abundance behavior, so only the best-match model data are shown here.

In both panels, modeled values for all of the molecules included in the matching procedure come within one order of magnitude (or better) of the observed values. In the IRAS 16293B comparison, the black-bar molecules CH_3NCO, HC_3N, and $CH_3C(O)NH_2$ deviate at least two orders of magnitude from the observations. For Sgr B2(N2), methyl isocyanate (CH_3NCO), methyl isocyanide (CH_3NC) and acetamide ($CH_3C(O)NH_2$) provide a particularly poor match. However, since these species were not included in the matching procedure, it is not a surprise that they are not well represented in the data shown here.

For the PILS data (IRAS 16293B), the top five molecules that match observations very well are formic acid (HCOOH), dimethyl ether (CH_3OCH_3), methyl formate ($HCOOCH_3$), acetic acid (CH_3COOH), and ethyl cyanide (C_2H_5CN). For the EMoCA data (Sgr B2(N2)), the five molecules that match the observations most accurately

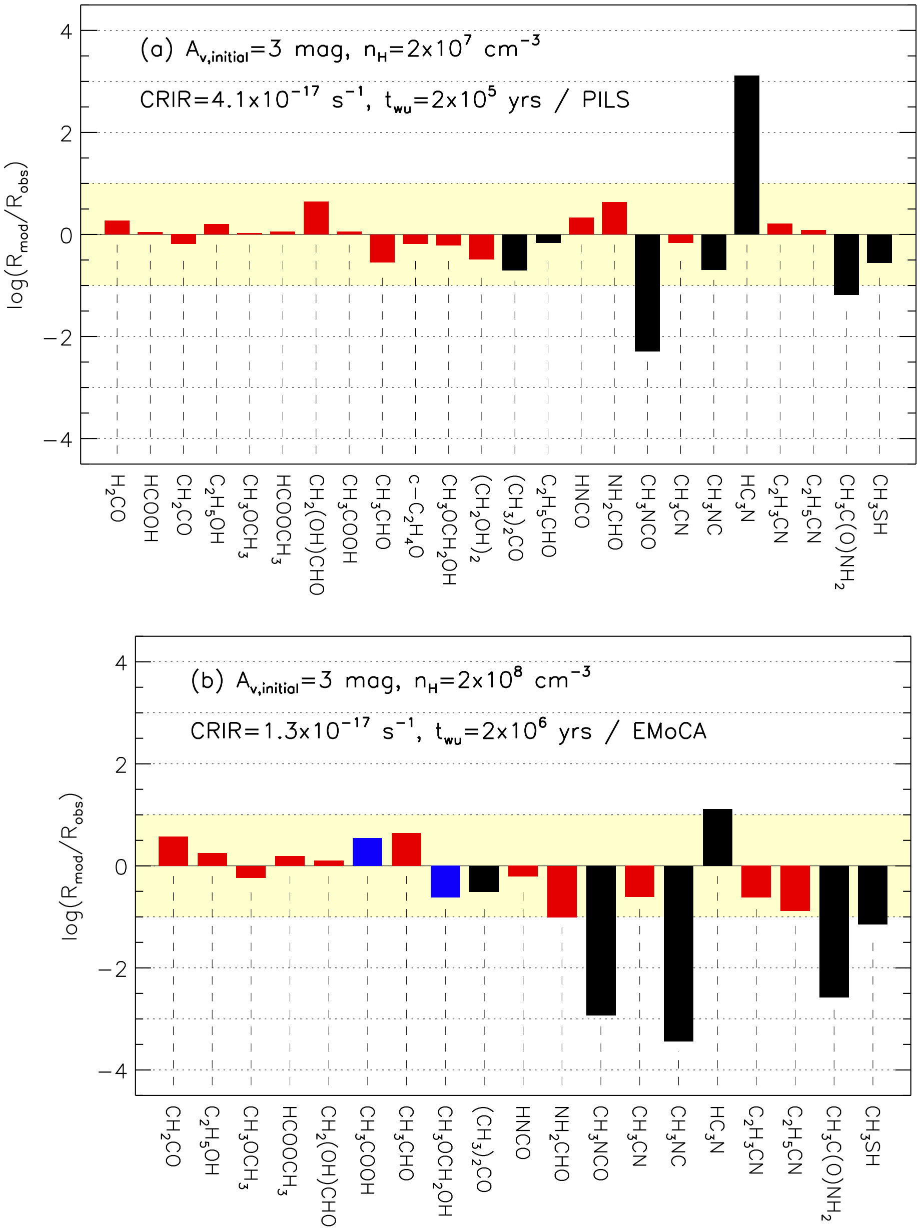

Figure A.1 Comparison between the peak gas-phase molecular abundances achieved in the best-match models (normalized to the models' peak methanol abundances), R_{mod}, and observational values of the same quantities (based on column densities), R_{obs}. Panel (a) corresponds to chemical species observed in the PILS survey of IRAS 16293B (Jørgensen et al., 2016); panel (b) corresponds to species observed in the EMoCA survey of Sgr B2(N2) (Belloche et al., 2016). Bars indicate the logarithm of $R_{\mathrm{mod}}/R_{\mathrm{obs}}$. Blue bars are based on observational upper limits; bars below the zero-line thus represent an exact match. Black bars are not included in the matching procedure, but are included for completeness. The shaded area represents values where the models and observations vary by 1 order of magnitude or less.

are ethanol (C_2H_5OH), dimethyl ether (CH_3OCH_3), methyl formate ($HCOOCH_3$), glycolaldehyde ($CH_2(OH)CHO$), and isocyanic acid (HNCO).

A.1.3 Discussion and Conclusions

In G22, out of the three models considered, the fast (5×10^4 yr) warm-up model agreed best with the IRAS 16293B data and the slow (1×10^6 yr) model agreed best with Sgr B2(N2). In the present results (Table A.1), we find that an intermediate warm-up timescale model (2.00×10^5) agrees best for IRAS 16293 and that a slow model (2.00×10^6) still agrees best for Sgr B2(N2). When comparing the results of Fig. A.1 with the equivalent bar plots of the "fast" model for PILS and the "slow" model for EMoCA considered in G22, we see that there are not extreme differences concerning the chemical species predictions. The three models considered in G22 all had initial visual extinctions of 3 mag, final hydrogen number densities of 2.00×10^8 cm^{-1}, and cosmic-ray ionization rates of 1.30×10^{-17} s^{-1}, while our own best-match models were not very far from these same values.

From Table A.1, it appears that Sgr B2(N2) has higher density matches than IRAS 16293B data, which is compatible with the fact that IRAS 16293B is a low-mass source and Sgr B2(N2) is a high-mass source. However, it is notable that neither source has an extreme MF:GA ratio, and also that the best-matching density values are generally on the lower end of the modeled range. If an extreme gas density were associated with a circumstellar disk, this might indicate that COM emission in both of these sources is not strongly associated with high-density regions of a disk structure.

The similarity of the top four model results in their predictions of chemical species abundances indicates that there are different setups that can produce acceptable results, even with the larger range of molecules included in the analysis. However, the best matching models for Sgr B2(N2) all have the longest warm-up timescale available in the grid, and the best-matching timescales for IRAS 16293 are all fairly close together. The ζ-values selected for each source are also quite strongly clustered, with the IRAS 16293 best-match model showing a marginally higher value than Sgr B2(N2) (4.11×10^{-17} versus 1.30×10^{-17} s^{-1}, respectively).

With this larger selection of molecules in the comparison, all of the physical parameters in the grid appear to be consistently constrained. The overall match parameter for IRAS 16293 is actually based on a larger number of molecules, so the smaller m-value that is actually achieved for its best-match model indicates a significantly better match than is achieved for Sgr B2(N2). The better quality of match may be seen by inspection of Fig. A.1. We note again that the black bars are not included in the matching procedure because they are not expected to be well reproduced by the present models (see G22 for discussion of this point). Acetone ($(CH_3)_2CO$) and propanal (C_2H_5CHO) are nevertheless quite well reproduced in the present results. We note also that the blue bars, which correspond only to an observational upper limit, are deemed to be a perfect match to observations if the bar falls below the zero-line; methoxymethanol (CH_3OCH_2OH) therefore seems to be well matched in the models, which was also found by G22.

In summary, we used the large parameter space to re-evaluate the comparison between the previous smaller collection of MAGICKAL models presented in G22 to observational data taken by the PILS (Jørgensen et al., 2016) and EMoCA (Belloche et al., 2016) surveys of IRAS 16293B and Sgr B2 (N2), respectively. For the EMoCA data of Sgr B2(N2), the best match models have higher densities as expected, standard or lower cosmic-ray ionization rates, and uniformly long timescales. For the PILS data of IRAS 16293B, the best match models have lower densities, standard to slightly higher cosmic-ray ionization rates, and medium timescales. Neither set of models falls into the most extreme values of any physical parameter in the grid.

REFERENCES

Adams, F. C., Lada, C. J., & Shu, F. H. 1987, The Astrophysical Journal, 312, 788

Agúndez, M., Marcelino, N., Cernicharo, J., Roueff, E., & Tafalla, M. 2019, A&A, 625, A147

Aikawa, Y., Wakelam, V., Garrod, R. T., & Herbst, E. 2008, The Astrophysical Journal, 674, 984

Aikawa, Y., Wakelam, V., Hersant, F., Garrod, R. T., & Herbst, E. 2012, The Astrophysical Journal, 760, 40

Bacmann, A., Taquet, V., Faure, A., Kahane, C., & Ceccarelli, C. 2012, A&A, 541, doi:10.1051/0004-6361/201219207

Barger, C. J., & Garrod, R. T. 2020, The Astrophysical Journal, 888, 38

Barger, C. J., Lam, K. H., Li, Z. Y., et al. 2021, Astronomy and Astrophysics, 651, A43

Belloche, A., Garrod, R. T., Müller, H. S. P., et al. 2019, Astronomy and Astrophysics, 628, A10

Belloche, A., Garrod, R. T., Zingsheim, O., Müller, H. S. P., & Menten, K. M. 2022, A&A, 662, A110

Belloche, A., Müller, H. S. P., Garrod, R. T., & Menten, K. M. 2016, A&A, 587, A91

Belloche, A., Maury, A. J., Maret, S., et al. 2020, A&A, 635, A198

Benner, S. A., Kim, H. J., & Biondi, E. 2019, Life, 9, 84

Bergin, E. A., & Tafalla, M. 2007, Annual Review of Astronomy and Astrophysics, 45, 339

Bergner, J. B., Martín-Doménech, R., Öberg, K. I., et al. 2019, ACS Earth and Space Chemistry, 3, 1564

Bhandare, Asmita, Commerçon, Benoît, Laibe, Guillaume, et al. 2024, A&A, 687, A158

Bisschop, S. E., Jørgensen, J. K., van Dishoeck, E. F., & de Wachter, E. B. M. 2007, A&A, 465, 913

Bohlin, R. C., Savage, B. D., & Drake, J. F. 1978, The Astrophysical Journal, 224, 132

Boogert, A. A., Gerakines, P. A., & Whittet, D. C. 2015, Annual Review of Astronomy and Astrophysics, 53, 541–581

Boogert, A. C. A., Pontoppidan, K. M., Knez, C., et al. 2008, The Astrophysical Journal, 678, 985

Brinch, C., Jørgensen, J. K., & Hogerheijde, M. R. 2009, A&A, 502, 199

Brogan, C. L., Hunter, T. R., Cyganowski, C. J., et al. 2018, ApJ, 866, 15

Brown, R. D., Crofts, J. G., Gardner, F. F., et al. 1975, The Astrophysical Journal Letters, 197, L29

Burke, D. J., Puletti, F., Brown, W. A., et al. 2015, Monthly Notices of the Royal Astronomical Society, 447, 1444

Cabedo, V., Maury, A., Girart, J. M., et al. 2023, Astronomy and Astrophysics, 669, A90

Caselli, P., Walmsley, C. M., Terzieva, R., & Herbst, E. 1998, The Astrophysical Journal, 499, 234

Cazaux, S., Tielens, A. G. G. M., Ceccarelli, C., et al. 2003, The Astrophysical Journal, 593, L51

Choudhury, Schilke, Stéphan, et al. 2015, A&A, 575, A68

Chu, L. E. U., Hodapp, K., & Boogert, A. 2020, The Astrophysical Journal, 904, 86

Chuang, K.-J., Fedoseev, G., Ioppolo, S., van Dishoeck, E., & Linnartz, H. 2015, Monthly Notices of the Royal Astronomical Society, 455, 1702

Commerçon, B., Launhardt, R., Dullemond, C., & Henning, Th. 2012, A&A, 545, A98

Coutens, A., Commerçon, B., & Wakelam, V. 2020, A&A, 643, A108

Drozdovskaya, M. N., van Dishoeck, E. F., Rubin, M., Jørgensen, J. K., & Altwegg, K. 2019, Monthly Notices of the Royal Astronomical Society, 490, 50

Dullemond, C. P., Juhasz, A., Pohl, A., et al. 2012, RADMC-3D: A multi-purpose radiative transfer tool, Astrophysics Source Code Library, record ascl:1202.015, ,

Dupuy, J. L., Lewis, S. P., & Stancil, P. C. 2016, The Astrophysical Journal, 831, 54

El-Abd, S. J., Brogan, C. L., Hunter, T. R., et al. 2019, The Astrophysical Journal, 883, 129

Emerson, J. P., Harris, S., Jennings, R. E., et al. 1984, The Astrophysical Journal Letters, 278, L49

Enoch, M. L., Corder, S., Duchêne, G., et al. 2011, The Astrophysical Journal Supplement Series, 195, 21

Evans, N. J., Francesco, J. D., Lee, J.-E., et al. 2015, The Astrophysical Journal, 814, 22

Evans, N. J., Yang, Y.-L., Green, J. D., et al. 2023, The Astrophysical Journal, 943, 90

Favre, C., Ceccarelli, C., López-Sepulcre, A., et al. 2018, The Astrophysical Journal, 859, 136

Fedoseev, G., Chuang, K.-J., Ioppolo, S., et al. 2017, The Astrophysical Journal, 842, 52

Fedoseev, G., Cuppen, H. M., Ioppolo, S., Lamberts, T., & Linnartz, H. 2015, Monthly Notices of the Royal Astronomical Society, 448, 1288

Fitz Axen, M., Offner, S. S. S., Gaches, B. A. L., et al. 2021, The Astrophysical Journal, 915, 43

Furuya, K., Aikawa, Y., Tomida, K., et al. 2012, The Astrophysical Journal, 758, 86

Gaches, B. A. L., & Offner, S. S. R. 2018, The Astrophysical Journal, 861, 87

Garrod, R. T. 2013, The Astrophysical Journal, 765, 60

—. 2019, The Astrophysical Journal, 884, 69

Garrod, R. T., & Herbst, E. 2006, A&A, 457, 927

—. 2023, Faraday Discussions, 245, 541

Garrod, R. T., Jin, M., Matis, K. A., et al. 2022, The Astrophysical Journal Supplement Series, 259, 1

Garrod, R. T., & Pauly, T. 2011, The Astrophysical Journal, 735, 15

Garrod, R. T., Wakelam, V., & Herbst, E. 2007, A&A, 467, 1103

Garrod, R. T., Weaver, S. L. W., & Herbst, E. 2008, The Astrophysical Journal, 682, 283

Geppert, W. D., Hamberg, M., Thomas, R. D., et al. 2006, Faraday Discuss., 133, 177

Good, D. A., & Francisco, L. J. S. 2002, J. Phys. Chem. A., 106, 1733

Halfen, D. T., Apponi, A. J., Woolf, N., Polt, R., & Ziurys, L. M. 2006, The Astrophysical Journal, 639, 237

He, J., Acharyya, K., & Vidali, G. 2016, The Astrophysical Journal, 823, 56

Henderson, B. L., & Gudipati, M. S. 2015, The Astrophysical Journal, 800, 66

Herbst, E., & van Dishoeck, E. F. 2009, Annual Review of Astronomy and Astrophysics, 47, 427

Hincelin, U., Commerçon, B., Wakelam, V., et al. 2016, The Astrophysical Journal, 822, 12

Hirota, T., Wolak, P., Hunter, T. R., et al. 2022, Publications of the Astronomical Society of Japan, 74, 1234

Hocuk, S., Szűcs, L., Caselli, P., et al. 2017, Astronomy and Astrophysics, 604, A58

Hollis, J. M., Lovas, F. J., & Jewell, P. R. 2000, The Astrophysical Journal, 540, L107

Hollis, J. M., Vogel, S. N., Snyder, L. E., Jewell, P. R., & Lovas, F. J. 2001, The Astrophysical Journal Letters, 554, L81

Hosokawa, T., & Omukai, K. 2009, The Astrophysical Journal, 691, 823

Hunter, T. R., Brogan, C. L., MacLeod, G., et al. 2017, ApJ, 837, L29

Hunter, T. R., Brogan, C. L., MacLeod, G., et al. 2017, The Astrophysical Journal Letters, 837, L29

Hunter, T. R., Brogan, C. L., De Buizer, J. M., et al. 2021, The Astrophysical Journal Letters, 912, L17

Imai, M., Oya, Y., Sakai, N., et al. 2019, The Astrophysical Journal Letters, 873, L21

Imai, M., Sakai, N., Oya, Y., et al. 2016, The Astrophysical Journal Letters, 830, L37

Ioppolo, S., Fedoseev, G., Chuang, K.-J., et al. 2020, Nature Astronomy, 5, 197

Ioppolo, S., Fedoseev, G., Chuang, K. J., et al. 2021, Nature Astronomy, 5, 197

Jacobsen, Steffen K., Jørgensen, Jes K., Di Francesco, James, et al. 2019, A&A, 629, A29

Jensen, S. S., Jørgensen, J. K., Furuya, K., Haugbølle, T., & Aikawa, Y. 2021, A&A, 649, A66

Jiménez-Serra, I., Vasyunin, A. I., Caselli, P., et al. 2016, The Astrophysical Journal Letters, 830, L6

Jiménez-Serra, I., Rodríguez-Almeida, Lucas F., Martín-Pintado, Jesús, et al. 2022, A&A, 663, A181

Jin, M., & Garrod, R. T. 2020, The Astrophysical Journal Supplement Series, 249, 26

Jin, M., Lam, K. H., McClure, M. K., et al. 2022, The Astrophysical Journal, 935, 133

Jørgensen, J. K., Belloche, A., & Garrod, R. T. 2020, Annual Review of Astronomy and Astrophysics, 58, 727

Jørgensen, J. K., Favre, C., Bisschop, S. E., et al. 2012, The Astrophysical Journal, 757, L4

Jørgensen, J. K., Visser, R., Sakai, N., et al. 2013, The Astrophysical Journal Letters, 779, L22

Jørgensen, J. K., van der Wiel, M. H. D., Coutens, A., et al. 2016, A&A, 595, A117

Jørgensen, J. K., Bourke, T. L., Myers, P. C., et al. 2005, The Astrophysical Journal, 632, 973

Jørgensen, J. K. 2004, A&A, 424, 589

Lam, K. H. 2022, PhD Dissertation, University of Virginia, doi:https://doi.org/10.18130/x2qv-6j63

Lee, J.-E., Evans, N. J., Baek, G., et al. 2024, The Astrophysical Journal Letters, 978, L3

Marcelino, N., Cernicharo, J., Agúndez, M., et al. 2007, The Astrophysical Journal, 665, L127

Masunaga, H., & Inutsuka, S.-i. 2000, The Astrophysical Journal, 531, 350

Masunaga, H., Miyama, S. M., & ichiro Inutsuka, S. 1998, The Astrophysical Journal, 495, 346

McClure, M. K., Rocha, W. R. M., Pontoppidan, K. M., et al. 2023, Nature Astronomy, 7, 431–443

McGuire, B. A., Shingledecker, C. N., Willis, E. R., et al. 2017, ApJL, 851, L46

Megías, A., Jiménez-Serra, I., Martín-Pintado, J., et al. 2022, Monthly Notices of the Royal Astronomical Society, 519, 1601

Mehringer, D. M., Snyder, L. E., Miao, Y., & Lovas, F. J. 1997, The Astrophysical Journal, 480, L71

Meyer, D. M. A., Vorobyov, E. I., Elbakyan, V. G., et al. 2021, Monthly Notices of the Royal Astronomical Society, 500, 4448

Nazari, P., Tabone, B., Rosotti, G. P., et al. 2022, A&A, 663, A58

Öberg, K. I., Garrod, R. T., van Dishoeck, E. F., & Linnartz, H. 2009, A&A, 504, 891

Occhiogrosso, A., Viti, S., Modica, P., & Palumbo, M. E. 2011, MNRAS, 418, 1923

Okoda, Y., Oya, Y., Imai, M., et al. 2022, The Astrophysical Journal, 935, 136

Okoda, Y., Oya, Y., Sakai, N., et al. 2024, The Astrophysical Journal, 970, 28

Okoda, Y., Oya, Y., Francis, L., et al. 2023, The Astrophysical Journal, 948, 127

Okoda, Y., Yang, Y.-L., II, N. J. E., et al. 2025, CORINOS. III. Outflow Shocked Regions of the Low-mass Protostellar Source IRAS 15398-3359 with JWST and ALMA, , , arXiv:2503.03050

Oya, Y., Sakai, N., Watanabe, Y., et al. 2017, The Astrophysical Journal, 837, 174

Padovani, M., Galli, D., & Glassgold, A. E. 2009, Astronomy and Astrophysics, 501, 619

Padovani, M., Ivlev, A. V., Galli, D., & Caselli, P. 2018, Astronomy and Astrophysics, 614, A111

Padovani, Marco, Marcowith, Alexandre, Galli, Daniele, Hunt, Leslie K., & Fontani, Francesco. 2021, A&A, 649, A149

Persi, P., Marenzi, A. R., Gómez, M., & Olofsson, G. 2001, A&A, 376, 907

Pontoppidan, K. M., Boogert, A. C. A., Fraser, H. J., et al. 2008, The Astrophysical Journal, 678, 1005

Rimmer, P. B., Herbst, E., Morata, O., & Roueff, E. 2012, Astronomy and Astrophysics, 537, A7

Rivilla, V. M., Colzi, L., Jiménez-Serra, I., et al. 2022, The Astrophysical Journal Letters, 929, L11

Rocha, W. R. M., & Pilling, S. 2020, The Astrophysical Journal, 896, 27

Rocha, W. R. M., van Dishoeck, E. F., Ressler, M. E., et al. 2024, A&A, 683, A124

Rocha, W. R. M., McClure, M. K., Sturm, J. A., et al. 2025, A&A, 693, A288

Sabatini, G., Bovino, S., & Redaelli, E. 2023, arXiv e-prints, arXiv:2304.00329

Salyk, C., Yang, Y.-L., Pontoppidan, K. M., et al. 2024, The Astrophysical Journal, 974, 97

Senevirathne, B., Andersson, S., Dulieu, F., & Nyman, G. 2017, Molecular Astrophysics, 6, 59

Shirley, Y. L., Evans, II, N. J., Rawlings, J. M. C., & Gregersen, E. M. 2000, The Astrophysical Journal Supplement Series, 131, 249

Shope, B. M., El-Abd, S. J., Brogan, C. L., et al. 2024, The Astrophysical Journal, 972, 146

Simons, M. A. J., Lamberts, T., & Cuppen, H. M. 2020, Astronomy and Astrophysics, 634, A52

Snow, T. P., & McCall, B. J. 2006, Annual Review of Astronomy and Astrophysics, 44, 367

Stone, J. M., Gardiner, T. A., Teuben, P., Hawley, J. F., & Simon, J. B. 2008, The Astrophysical Journal Supplement Series, 178, 137

Stone, J. M., Tomida, K., White, C. J., & Felker, K. G. 2020, The Astrophysical Journal Supplement Series, 249, 4

Stutz, A. M., Rubin, M., Werner, M. W., et al. 2008, The Astrophysical Journal, 687, 389

Tu, Y., Li, Z.-Y., & Lam, K. H. 2022, Monthly Notices of the Royal Astronomical Society, 515, 4780 van der Tak, F. F. S., Belloche, A., Schilke, P., et al. 2006, Astronomy and Astrophysics, 454, L99

Vazzano, M. M., Fernández-López, M., Plunkett, A., et al. 2021, Astronomy and Astrophysics, 648, A41

Visser, R., Bergin, Edwin A., & Jørgensen, Jes K. 2015, A&A, 577, A102

Visser, R., Doty, S. D., & van Dishoeck, E. F. 2011, A&A, 534, A132

Visser, R., van Dishoeck, E. F., Doty, S. D., & Dullemond, C. P. 2009, A&A, 495, 881

Williams, G. M., Cyganowski, C. J., Brogan, C. L., et al. 2023, Monthly Notices of the Royal Astronomical Society, 525, 6146

Yang, Y.-L., Sakai, N., Zhang, Y., et al. 2021, The Astrophysical Journal, 910, 20

Yang, Y.-L., Green, J. D., Pontoppidan, K. M., et al. 2022, The Astrophysical Journal Letters, 941, L13

Zeng, S., Jiménez-Serra, I., Rivilla, V. M., et al. 2018, Monthly Notices of the Royal Astronomical Society, 478, 2962

Zeng, S., Zhang, Q., Jiménez-Serra, I., et al. 2020, Monthly Notices of the Royal Astronomical Society, 497, 4896

Álvarez Barcia, S., Russ, P., Kästner, J., & Lamberts, T. 2018, Monthly Notices of the Royal Astronomical Society, 479, doi:10.1093/mnras/sty1478

Öberg, K. I., Boogert, A. C. A., Pontoppidan, K. M., et al. 2008, The Astrophysical Journal, 678, 1032

Öberg, K. I., Bottinelli, S., Jørgensen, J. K., & van Dishoeck, E. F. 2010, The Astrophysical Journal, 716, 825